

# **3D NLTE RADIATIVE TRANSFER MODELLING OF M-DWARF ATMOSPHERES**

Dissertation zur Erlangung des Doktorgrades  
an der Fakultät für Mathematik, Informatik und Naturwissenschaften  
Fachbereich Physik  
der Universität Hamburg

vorgelegt von

**Ivan De Gennaro Aquino**

aus Vico Equense, Italien

Hamburg, 2016



Gutachter der Dissertation: Prof. Dr. Peter H. Hauschildt  
Dr. Sven Wedemeyer

Vorsitzender der Prüfungskommission: Prof. Dr. Jochen Liske

Mitglieder der Prüfungskommission: Prof. Dr. Robi Banerjee  
Prof. Dr. Marcus Brüggem  
Prof. Dr. Peter H. Hauschildt  
Prof. Dr. Jochen Liske  
Dr. Sven Wedemeyer

Datum der Disputation: 27.01.2017



# Abstract

The chromosphere is a region in the atmosphere of (cool) stars, working as interface between the optically thick photosphere and the optically thin corona. It is a highly dynamic environment, shaped by shocks and magnetic fields, with cold and hot gas co-existing at similar heights. While directly imaged on the Sun, the chromosphere of other stars can only be detected spectroscopically, using several emission lines, e.g. the Ca II H&K doublet or H $\alpha$ , well studied and calibrated chromospheric diagnostics.

M-dwarfs are the most common stars in the Milky Way. They are characterised by low effective temperatures, with the optical and infrared spectrum being dominated by molecular absorption bands. Due to convective overshooting and acoustic waves penetrating deep into the atmosphere, and magnetic heating processes, their chromospheric activity is generally very intense. Accurate estimate of the stellar parameters is, therefore, only possible with models that consider the large range of phenomena and complexity of M-dwarf atmospheres.

One-dimensional models, although successful in reproducing observations, rely on restrictive physical assumptions. Three-dimensional simulations have been conducted to study the convective motions in M-dwarf atmospheres. Radiative-magneto-hydrodynamic simulations (R-MHD) with the CO<sup>5</sup>BOLD code showed that M-dwarf chromospheres feature complex dynamics qualitatively similar to what is known for the solar chromosphere. However, because of high computational costs, 3D MHD frameworks are currently unable to compute lines and continua opacities with a detailed treatment of the atomic level populations, focusing on estimating the radiative transfer energy correctly with simplified methods. Moreover, departures from local thermodynamic equilibrium (LTE) conditions must be taken into account due to the very low densities in the chromosphere. An additional step is required to calculate these properties. The non-LTE (NLTE) radiative transfer code PHOENIX/3D provides a general, massively parallelised, numerical framework. It allows to compute the radiative properties of 3D model atmospheres and to produce synthetic observables, e.g. spectrum and synthetic images, to compare with observations.

For this thesis, a snapshot from CO<sup>5</sup>BOLD M-dwarf models was used as input to PHOENIX/3D simulations, including multi-level NLTE opacity for the most abundant atomic species, as well as LTE background opacities. The models show the importance to treat the radiative transfer in the chromosphere allowing for departures from LTE. Spectrum and chemical concentrations are both strongly affected by the NLTE treatment. The 3D geometry has great influence on the radiative properties of the atmosphere. Synthetic images are used to investigate the depth of formation of spectral lines and continua. Technical issues concerning aliasing artefacts are also discussed.

This work shows that 3D multi-level NLTE modelling of M-dwarf atmospheres is currently possible, provided using large super-computing facilities. With further optimisation of the PHOENIX/3D code, and increased computational capabilities in the future, we will model stellar chromospheres with higher spatial and wavelength resolution.



# Zusammenfassung

Die Chromosphäre ist ein Bereich in den Atmosphären von (kühlen) Sternen, welche die optisch dicke Photosphäre mit der optisch dünnen Korona verbindet. Sie ist eine besonders dynamische Umgebung, geformt durch Schocks und Magnetfelder, in der kühles Gas mit warmen Gas in gleichen Höhen nebeneinander besteht. Obwohl sie an der solaren Oberfläche direkt beobachtet werden kann, erkennen wir die Chromosphäre anderer Sterne nur mit Hilfe gut erforschter und kalibrierter spektroskopischer Methoden, wie z. B. basierend auf die Emissionslinien Ca II H&K und H $\alpha$ .

M-Zwerg sind die häufigsten Sterne der Milchstraße. Charakterisiert sind sie durch niedrige effektive Temperaturen. Ihre optischen und infraroten Spektren werden von molekularen Absorptionsbanden dominiert. Konvektive Strömungen, akustische Wellen, welche tief in die Atmosphäre eindringen, und magnetische Erwärmungsprozesse erzeugen ihre starke chromosphärische Aktivität. Eine genaue Abschätzung der Sternparameter ist daher nur mit Modellen möglich, die die große Phänomenologie und Komplexität der Atmosphären von M-Zwergen mit einbeziehen.

Eindimensionale Modelle sind zwar erfolgreich bei der Wiedergabe von Beobachtungen, allerdings basieren sie auf restriktive physikalischen Annahmen. Daher wurden dreidimensionale Simulationen durchgeführt, um die konvektiven Bewegungen in den Atmosphären von M-Zwergen zu untersuchen. Strahlungs-Magneto-Hydrodynamik-Simulationen (R-MHD) mit dem CO<sup>5</sup>BOLD Code zeigten, dass die Chromosphären von M-Zwergen qualitativ die gleiche komplexe Dynamik wie die Sonnenchromosphäre besitzen. Aufgrund des hohen Rechenaufwands ist es den 3D MHD Codes derzeit nicht möglich, die Opazitäten von Linien und Kontinua durch eine detaillierte Berücksichtigung der Besetzungszahlen der Atomniveaus zu berechnen. Der Fokus liegt dabei auf die richtige Abschätzung der Strahlungsenergie mit vereinfachten Methoden. Desweiteren müssen Abweichungen vom lokalen thermodynamischen Gleichgewicht (LTE) betrachtet werden, welche aufgrund der sehr geringen Gasdichten in der Chromosphäre auftreten. Um dies alles berechnen zu können, ist ein weiterer Schritt erforderlich. Der nicht-LTE (NLTE) Strahlungstransport-Code PHOENIX/3D bietet einen allgemeinen, massiv parallelisierten, numerischen Rahmen. Mit ihm ist es möglich, die Strahlungseigenschaften von 3D-Modellatmosphären zu berechnen und synthetische Spektren und Bilder mit Beobachtungen zu vergleichen.

Für diese Dissertation wurde ein Schnappschuss von CO<sup>5</sup>BOLD M-Zwerg-Modellen als Startwerte für PHOENIX/3D verwendet. Multi-Level-NLTE Opazitäten der häufigsten Atomarten und LTE Hintergrund-Opazitäten wurden mit einbezogen. Die Simulationen zeigen die Bedeutung der Abweichungen vom LTE für den Strahlungstransport in der Chromosphäre. Spektrum und chemische Konzentrationen werden stark von der Behandlung des NLTEs beeinflusst. Die 3D-Geometrie hat einen großen Effekt auf die Strahlungseigenschaften der Atmosphäre. Synthetische Bilder der Modelle werden verwendet, um die Tiefe der Bildung von Spektrallinien und Kontinua zu untersuchen. Zusätzlich werden technische Probleme durch Aliasing Artefakte diskutiert.

Diese Arbeit zeigt, dass, sofern große Super-Computing-Einrichtungen zur Verfügung stehen, eine 3D-Multi-Level-NLTE Modellierung der Atmosphären von M-Zwergen gegenwärtig bereits möglich ist. Mit der weiteren Optimierung des PHOENIX/3D Codes und durch erhöhte rechnerische Möglichkeiten in der Zukunft werden wir stellare Chromosphären mit einer höheren räumlichen und Wellenlängen-Auflösung modellieren.



# Contents

<b>1</b>	<b>Introduction</b>	<b>1</b>
<b>2</b>	<b>The chromosphere</b>	<b>3</b>
2.1	Phenomenology . . . . .	3
2.2	Simulations . . . . .	7
2.3	Do we really need 3D NLTE models? . . . . .	10
<b>3</b>	<b>Radiative transfer concepts</b>	<b>13</b>
3.1	The radiative transfer equation . . . . .	13
3.2	Photons and particles . . . . .	14
3.3	Kinetic equilibrium . . . . .	19
3.4	Iterative solutions . . . . .	20
<b>4</b>	<b>Computational framework</b>	<b>23</b>
4.1	PHOENIX . . . . .	23
4.2	CO <sup>5</sup> BOLD . . . . .	25
4.3	Setup for this project . . . . .	29
<b>5</b>	<b>Results</b>	<b>35</b>
5.1	NLTE only opacities (NN model) . . . . .	35
5.2	NLTE and LTE opacities (NL model) . . . . .	35
5.3	Small model atoms (NS model) . . . . .	41
5.4	Aliasing artefacts . . . . .	45
<b>6</b>	<b>Discussion</b>	<b>51</b>
6.1	Flux spectrum . . . . .	51
6.2	Synthetic images . . . . .	53
6.3	Mean vs. median 1D profiles . . . . .	59
6.4	NLTE effects . . . . .	60
6.5	Species concentrations . . . . .	64
6.6	Binned vs. non-binned model . . . . .	68
6.7	Aliasing artefacts . . . . .	70
<b>7</b>	<b>Conclusions and outlook</b>	<b>73</b>
	<b>Bibliography</b>	<b>77</b>



# Chapter 1

## Introduction

The solar atmosphere is a dynamic environment, changing on large and small spatial and temporal scales. That the solar “surface”, roughly corresponding to the *photosphere*, is not a perfect sphere is known since the discovery of the sunspots centuries ago. During a total solar eclipse in 1868, Sir Norman Lockyer observed a thin layer extending above the solar disk. He called it the *chromosphere*

*“...in order to distinguish it from the cool absorbing atmosphere on the one hand, and from the white light-giving photosphere on the other”*  
(Lockyer, 1868).

This bright, red coloured layer is located at the base of a much more extended region of the solar atmosphere, the *corona*, which bright prominences and features are easily observable during a total eclipse.

At the same time as Lockyer, Jansen observed Balmer emission lines while obtaining spectra of prominences during a total eclipse (see Heinzel et al., 2007, for a review on the history of solar chromosphere observations). When observed off-limb, the spectrum of the upper solar atmosphere is characterised by emission lines, unlike the absorption-dominated photospheric spectrum. The strength and shape of several emission lines are used to measure the *chromospheric activity*. In the last decades, solar research achieved great accuracy with ground observatories, such as the Swedish Solar Telescope (Scharmer et al., 2003), the Dutch Open Telescope (Rutten et al., 2004a), the GREGOR telescope (Schmidt et al., 2012), ALMA (Wedemeyer et al., 2016), etc., and space telescopes, like SOHO (Domingo et al., 1995), HINODE (Tsuneta et al., 2008), STEREO (Driesman et al., 2008), SDO (Pesnell et al., 2012), IRIS (De Pontieu et al., 2014), and others. We can now resolve phenomena on the solar surface with very high angular and temporal resolution at many different wavelengths (e.g. the Sun observed in the core of the Ca II 8542 Å line with the Swedish Solar Telescope, Fig. 1.1).

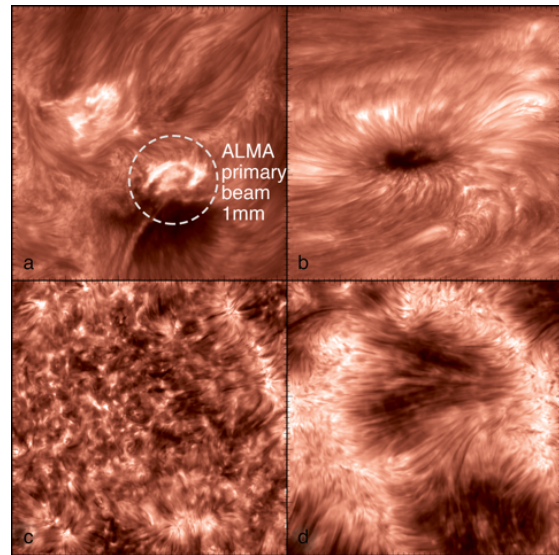


Figure 1.1: Solar chromosphere observed at Ca II 8542 Å with the Swedish Solar Telescope (from Wedemeyer, 2016). The four panels’ field of view is  $1 \times 1$  arc-minute, to compare with the ALMA 1 mm in the white circle. Respectively, the panels show (a) an active region with an ongoing flare, (b) a sunspot, (c) a quiet region inside a coronal hole, (d) a decaying active regions.

Stellar chromospheres were detected for the first time by Eberhard and Schwarzschild (1913), who, inspired by solar observations, observed a sharp reversal in the Ca II K line core for Arcturus. Chromospheres have been observed on cool dwarfs and giants, from late A to M-type.

The study of the chromosphere of very cool stars, like M-dwarfs, covers several interesting topics: evolutionary models, stellar magnetic fields, convection, flares, and many more. Recently, the hunt for exo-planets has become a major driver: planets orbiting closely around a host star induce a gravitational feedback on the stellar motion (Alonso-Floriano et al., 2015). The spectroscopic signatures of chromospheric activity carry invaluable information about the physical processes in stellar atmospheres, and correctly modelling the chromosphere is a crucial task to accurately determine the stellar properties and to corroborate and improve the theory.

Theoretical models to predict and simulate the solar and stellar atmosphere have been built since the 1960s, primarily due to the great advancements in computational techniques and infrastructure. The complexity of these models has increased steadily, thanks to many different contributions: multi-wavelength observations, better micro-physics, faster computers with larger memories, etc. While the first models assumed one-dimensional atmospheres, whether spherical or plane-parallel, during the last three decades multi-dimensional codes have become progressively more popular for many simulation models. M-dwarf atmospheres represent challenging environments to model: they feature activity, sometimes also major flares; strong convective flows extend to the photosphere; atomic and molecular opacities all play important roles; departures from the ideal *local thermodynamic equilibrium* (LTE) conditions are typical in the chromosphere.

3D radiative-magneto-hydrodynamic codes, e.g. CO<sup>5</sup>BOLD (Freytag et al., 2012), have been developed to simulate stellar atmospheres to investigate fundamental processes such as convection, waves propagation, reconnection, non-radiative heating, etc. Nowadays 3D MHD codes' radiative transfer treatment focuses mainly on properly estimating the radiative energy in order to compute, with sufficient accuracy, the energy budget of the atmosphere. Therefore, they cannot calculate the detailed radiative properties of the model, such as atomic and molecular line opacities, or departures from LTE, due to very high computational costs. 3D radiative transfer codes have to be used to compute the spectral properties of MHD models *a posteriori* and to produce synthetic observables.

The non-LTE (NLTE) radiative transfer code PHOENIX/3D provides an excellent framework to investigate the radiative properties of M-dwarf atmospheres. The purpose of my work was to analyse the outcome of M-dwarfs PHOENIX/3D NLTE simulations, using photosphere-chromosphere input models computed with the radiation-magneto-hydrodynamics code CO<sup>5</sup>BOLD.

I here outline the structure of this thesis. Chapter 2 covers the phenomenology and simulations of the chromosphere. Some of the terms used in this chapter are covered in more detail in Chapter 3, where I briefly introduce the most important aspects of radiative transfer. In Chapter 4, I describe the computational framework used for my simulations, namely the PHOENIX/3D and the CO<sup>5</sup>BOLD codes. Results from the models are presented in Chapter 5, and analysed and discussed in Chapter 6. Chapter 7 is dedicated to conclusions and future prospects.

## Chapter 2

# The chromosphere

During the last decades, the understanding of the chromosphere went hand-in-hand with the advancement in observational techniques and theoretical models.

Many of the processes occurring on the Sun, which we can directly observe and image, are indirectly observed on other stars. This solar-stellar connection is naturally bi-directional: we can improve our understanding of the solar atmosphere by investigating these phenomena for stars with different effective temperatures, radii, rotational periods, or various other stellar parameters.

Several reviews were helpful for writing this chapter: Heinzel et al. (2007) covers many observational and theoretical aspects; Hall (2008) reviews stellar chromospheric activity, focusing mainly on the observational aspects; recent findings and simulations about the quiet Sun are reviewed in Wedemeyer-Böhm et al. (2009); low mass stars are reviewed in Reid and Hawley (2005).

### 2.1 Phenomenology

#### The Sun

In visible light, the solar disk appears at first glance as a quite uniform surface, if not for the dark *sunspots*, localised region with strong magnetic field and temperatures significantly lower than the average temperature. During a total solar eclipse, it is also possible to observe gas filaments at the solar limb, the *prominences*. These features are bright when observed at the limb, but dark when observed in front of the disk (and in that case they are simply called *filaments*). Outside of sunspots associations, *granules* cover the whole surface: these cells are the top of convective flows, and have extensions on the order of  $10^3$  km. Large scale, deeper convective cells are responsible for the *super-granulation*, features with diameters on the order of  $10^4 - 4 \times 10^4$  km.

A total solar eclipse also reveals the *corona*, the outermost part of the solar atmosphere: it features streams and loops of gas changing and evolving on short time scales (hours, up to days), shaped by the magnetic fields (see Fig. 2.1). The bulk of the emission is in X-ray, hinting at very high plasma temperatures, up to million kelvins. Areas characterised by enhanced coronal emission and strong magnetic fields are called *active regions*. The transition between chromosphere and corona is abrupt, with the temperature increasing by almost two orders of magnitude in less than one pressure scale height. This temperature step is called *transition region*.

The chromosphere appears to be very narrow, on average approximately 2000 km, and it represents the interface between the photosphere and the corona. Small bright patches on the solar disk called *plage* can be observed around sunspots: they are associated with magnetic field concentrations and chromospheric emission. The latter comes in the form of emission lines, which represent the signature of excess radiative losses compared to radiative equilibrium conditions. A multitude of species are observed: in the optical, lines from Ca II (the H&K doublet) and H I are the strongest features; in the UV, Lyman- $\alpha$  and Mg II (the h&k doublet), along with many other weaker lines

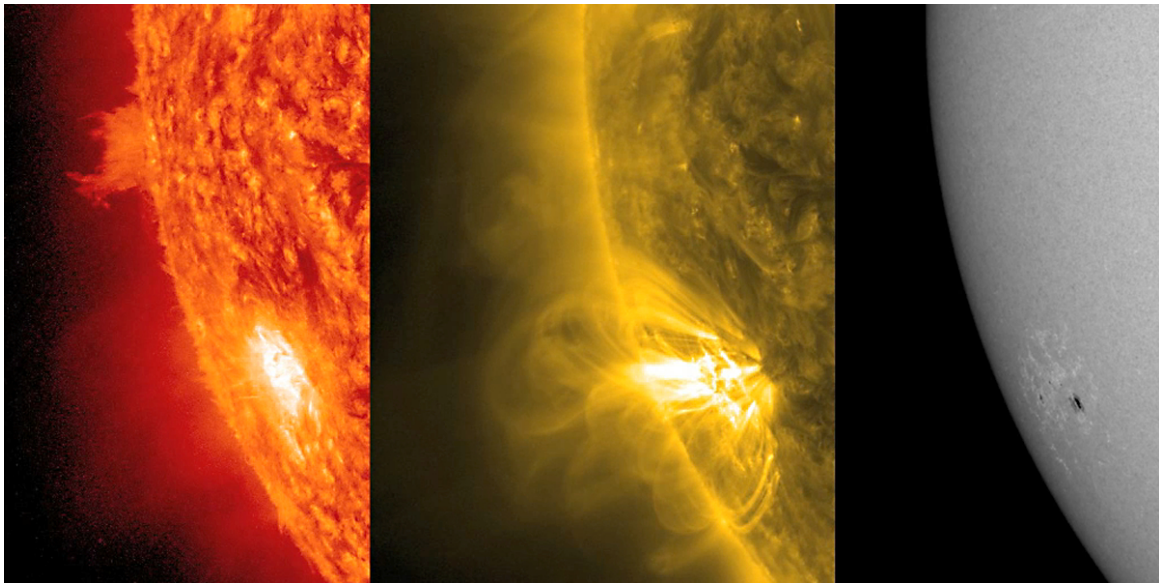


Figure 2.1: Three images from the SDO telescope of an active region on the Sun. Left panel: 304 Å band, showing the hot chromosphere; diffuse gas is suspended above the active region, and a bright prominence is visible at the limb. Middle panel: 171 Å band, displaying the corona; loops are visible arising above the active region. Right panel: 6173 Å band, showing the photosphere; the sunspot is dark, with bright plages surrounding it. From the SDO picture gallery <http://sdo.gsfc.nasa.gov/gallery/>.

(Linsky, 1980). The Ca II H&K lines are physically and historically important for determining the plasma conditions in the chromosphere, given their sensitivity to the electron density and temperature.

Narrow passbands observations display the solar disk at different wavelengths. In H $\alpha$ , we can observe spicular shaped structures, few thousands kilometres long, covering almost uniformly the solar surface. They are called *mottles*, *spiculae*, or *fibrils* when observed in correspondence with quiet regions, plage, or active regions, respectively. They are also associated with chromospheric emission: Rutten (2007) suggests that the chromosphere should be defined as the total mass of fibrils observed in H $\alpha$  emission.

Cooling in the chromosphere (which accounts for less than 0.01% of the total radiative flux emitted from the Sun) occurs mainly in strong resonance lines and the H $^-$  continuum, in contrast to the photosphere where the continuum plays the biggest role, in the optical and infrared. In the corona, the bulk of the emission is in X-rays, hinting at very high plasma temperatures, up to a few million kelvins. Consequently, the chromosphere needs a separate approach when investigating the ongoing radiative processes.

Already Leighton (1959) mentioned that non-radiative processes, of mechanical or magnetic origin, are playing an important role in the energy budget of the outer solar atmosphere. The presence of a temperature minimum, where the bottom of the chromosphere is located, is a clear evidence for effective non-radiative heating mechanisms active in the upper atmosphere. In truth, hot and cold gas co-exist at chromospheric heights, as clearly suggested by the observation of CO lines at the solar limb (Ayres and Testerman, 1981; Solanki et al., 1994). Due to its role as interface, some of the processes ongoing in the chromosphere are necessarily responsible for the coronal heating. What heats the coronal plasma up to millions of degrees? The details of this are still largely debated (Klimchuk, 2015).

Pioneering solar observations by Leighton (1959) revealed that Ca II emission is spatially correlated with magnetic field concentrations. In the Sun, magnetic fields are continuously generated by the  $\alpha\Omega$ -dynamo (see Charbonneau, 2014, for a recent review). Electric currents due to ionised gas within the Sun produce magnetic fields. Differential rotation winds up the magnetic fields lines,

generating a toroidal field (the  $\Omega$ -effect), while the solar rotation itself, through the Coriolis force, twists the magnetic field tubes, inducing a poloidal field (the  $\alpha$ -effect). Thanks to convection, the magnetic field tubes are advected from the interior through the surface into the atmosphere, where they form the sunspots groups. The  $\alpha\Omega$ -dynamo also predicts that shorter rotation periods produce stronger magnetic fields.

In the chromosphere, the spicular features mentioned above spatially correspond to the *magnetic network*. The foot-points of the magnetic network are characterised by vertical field lines that mostly form loops and connect to the opposite polarity magnetic field on the other sides of the cell. This extended magnetic sheet that overlays inter-network regions is called *canopy*.

Convective flows and turbulence are responsible for the granulation pattern observable in the photosphere, as well as for the generation of oscillation modes, like the acoustic  $p$ -modes in the photosphere, which cause the 3 minute (peak frequency) oscillations in the inter-network chromosphere. These oscillations are measurable as Doppler shift of spectral lines. De Pontieu et al. (2003) confirmed that coronal oscillations are correlated to photospheric  $p$ -modes, which again highlights the active role of the chromosphere considering the energy and mass exchanges between photosphere and corona. Waves generated by these oscillations are responsible for acoustic heating in the chromosphere (see Section 2.2).

More recently, thanks to high angular and temporal resolution measurements, Wedemeyer-Böhm and Rouppe van der Voort (2009b) observed *chromospheric swirls*, tornado-like features with diameters on the order of  $10^3$  km, covering almost ubiquitously the solar surface. These vortices feature up-flows of gas from the photosphere, through the chromosphere, into the corona. Multi-wavelength observations are described in Wedemeyer-Böhm et al. (2012), who finally confirmed the magnetic nature of these phenomena and their role in channelling energy from the convective zone into the upper layers of the solar atmosphere.

## Stars

Unlike the Sun, we cannot yet directly image chromospheric features on other stars. For now, we have to rely on photometry and spectroscopy, possibly conducted in multiple wavelength ranges, to study stellar chromospheric activity. However, this may change in the near future thanks to observational facilities like ALMA, which angular resolution is planned to be sufficient to resolve the stellar disk of nearby giants. For instance, Wong et al. (2016) discuss inner wind high resolution images of Mira.

Chromospheric activity can be observed for stars throughout the whole Hertzsprung–Russell-diagram, from late A to M-dwarfs on the main sequence, as well as in certain giants. Correspondingly, chromospheric activity appears for main sequence stars “crossing” the transition from radiative to convective envelope (Simon and Landsman, 1991). Stars earlier than type A cannot rely on neutral hydrogen as cooling agent because it is mostly ionised and they do not have a chromosphere, nor a corona.

Ca II H&K emission has been studied intensively throughout the last century and is still a primary chromospheric activity indicator. It was actually easier to observe in the past thanks to the high sensitivity of the emulsion plates in the near UV (modern CCDs are typically more sensitive in the red). Long-term studies are important to investigate periodicities in the chromospheric activity. One of the main observational campaigns was the “HK project”, run at the Mount Wilson Observatory (Wilson, 1978): they measured Ca II H&K emission (quantified with the *S-index*) for approximately 2200 stars from 1966 to 2003 (Baliunas et al., 1998).

Long before the Mount Wilson survey, Wilson and Vainu Bappu (1957) discovered the *Wilson-Bappu effect*: absolute magnitude and logarithm of the Ca II K line emission widths, for G and cooler stars, for dwarfs and giants, are linearly correlated over 5 orders of magnitude in luminosity. Reimers (1973) empirically demonstrated that this effect originates from a relation between the surface gravity, effective temperature and the Ca II K emission width  $W_0 \sim g^{-0.25} T_{\text{eff}}^{1.2}$ . A similar correlation is

observed for Mg II k and, although weaker, for H $\alpha$ . A theoretical derivation of this effect, using scaling laws and assuming a hydrostatic atmosphere and a non-specified source of non-radiative heating, is explained by Ayres et al. (1975) and Ayres (1979). They suggested mechanical processes, i.e. waves energy dissipation, and/or magnetic processes, i.e. currents and small-scale reconnection, as possible sources of non-radiative heating (more details in Section 2.2).

Like the Sun, magnetic field generation for cool dwarfs is due to the  $\alpha\Omega$ -dynamo, which in turn is due to differential rotation within the stellar structure. Thanks to Mount Wilson data, Noyes et al. (1984) were able to correlate the rotational period of several late-type dwarfs with their mean activity level: the faster the rotation, the higher the activity. This correlation is a perfect example of solar-stellar connection: since chromospheric emission and magnetic fields are well correlated on the solar surface, and the  $\alpha\Omega$ -dynamo theory predicts stronger magnetic field amplification with faster rotation, we can assume that magnetic heating is an important source of non-radiative heating regardless of the spectral type. Moreover, chromospheric diagnostics can be used to investigate stellar ages: low mass dwarfs spend a long time on the main sequence, and they lose angular momentum and spin-down due to magnetic braking (Schatzman, 1962), therefore slowly becoming less active.

The magnetic structures of cool stars has been intensively investigated since the publication of the Mount Wilson studies and the UV space telescopes, like the IUE (Kondo et al., 2013). Using multi-wavelength data, the magnetic properties of cool star atmospheres were extensively investigated in a long series of papers, starting with Middelkoop and Zwaan (1981). Schrijver (1987) found tight power-laws for chromospheric and coronal indicators (Ca II H&K, Mg II h&k, C II-IV, Si II), provided that a lower-limit, *basal flux*, is subtracted from the measured flux densities. He suggests that the basal flux represents the minimum level of activity for the chromosphere, due to acoustic heating, while the excess flux originates from magnetic activity.

## M-dwarfs

Low mass stars of less than  $0.8 M_{\odot}$  are the most abundant stellar objects in the Milky Way, counting up to 70% of all the stars, and roughly 40% of the total mass of the galaxy (Bochanski et al., 2010). M-dwarfs masses range from approximately  $0.08$  to  $0.6 M_{\odot}$  and the effective temperatures go from 2300 to 3900 K. The luminosity is intrinsically very low, with  $L_{\text{bol}}/L_{\odot} \approx 0.02\% - 7\%$ , making them generally challenging observational targets.

Due to the low effective temperature, most of the energy is radiated in the near infrared, between 1 and 3  $\mu\text{m}$ . The (photospheric) spectrum is characterised by strong molecular bands, with the main molecular species being TiO, VO and several hydrides like CaH, MgH, FeH etc. Infrared spectroscopy shows also CO and water bands. Amongst the atomic species, the most notable are Ca I and II, Na I and K I. The Ca II H&K lines may show absorption with an emission core, which originates in the chromosphere. The Balmer lines' presence and shape depend on the level of activity: if the level is low, they are not observable; with increasing activity, an absorption profile appears; the depth of the line increases and then decreases with higher activity, eventually being replaced by an emission profile for very high activity (Cram and Giampapa, 1987). UV and X-ray spectral features are tracing gas from higher regions in the atmosphere, namely transition region and corona.

Compared to earlier type stars, measuring chromospheric activity in M-dwarfs is more challenging: being much brighter in the infrared than in the blue, it is harder to measure Ca II H&K lines fluxes. To overcome this problem, H $\alpha$  has been extensively used as activity indicator (Giampapa and Liebert, 1986), and other lines, e.g. the Ca II infrared triplet, represent possible chromospheric diagnostics suitable for long wavelength instruments.

Balmer lines' emission has been observed for a large fraction of M-dwarfs, labelled *dMe* stars. The ratio between H $\alpha$  luminosity and the bolometric luminosity is, basically, constant for values of  $M_{\text{bol}}$  up to 12 and then decreases for later types. Joy and Abt (1974) showed that dM and dMe stars do not differ statistically in absolute magnitude, which suggests that the photospheric properties of

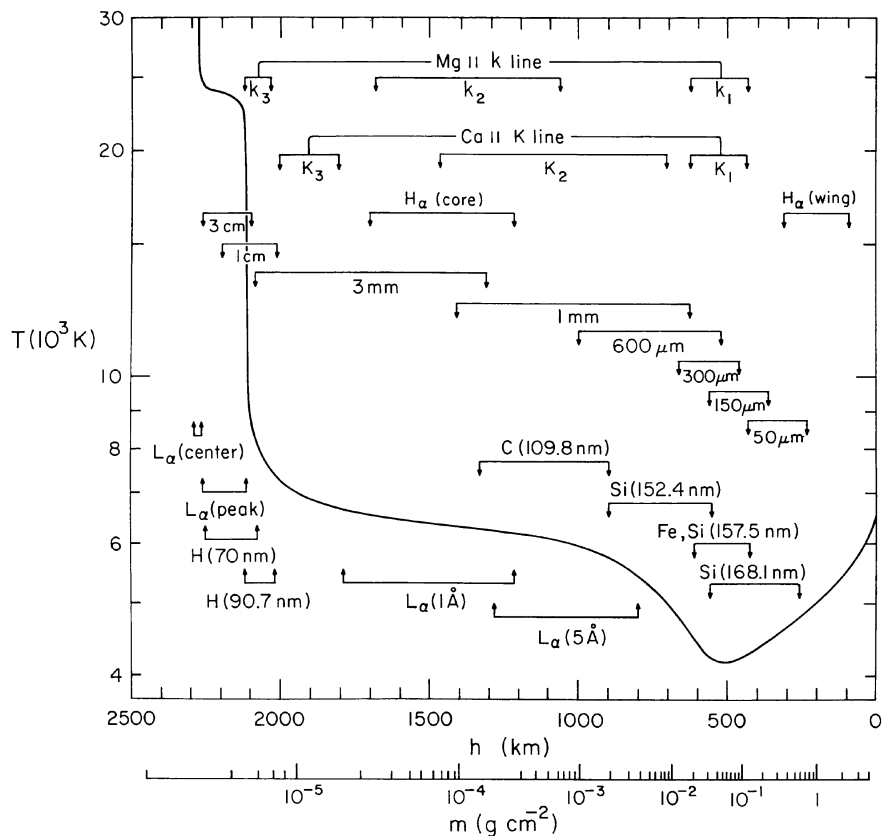


Figure 2.2: Average quiet Sun model from Vernazza et al. (1981). The photosphere is on the right side of the plot (lower height), with the chromosphere extending up to the transition region (the discontinuity at  $h \sim 2100$  km). The formation heights of several lines and continua are also marked.

dM and dMe are substantially identical.

With high-cadence observations, it is common to observe  $H\alpha$  and Ca II H&K line fluxes varying by factors of 2 or more in a few hours, due to small-scale flares. However, many M-dwarfs exhibit major flares: the UV and blue fluxes can increase by 2 orders of magnitude in a few minutes and emission lines from a large ensemble of species appear; the light-curve and spectrum go back to quiescence within 10 - 20 minutes. Stellar flares, like solar flares, can be extremely useful to investigate the properties of the flaring object and the heating mechanism in the upper atmosphere.

## 2.2 Simulations

### The Sun

The first solar atmosphere models used pioneering analytic theoretical models, such as the Schuster-Schwarzschild or the Milne-Eddington model, and curve-of-growth abundance measurements to estimate the main opacity sources and the thermal structure of the outer layers of the Sun (Unsöld, 1938). More complex simulations that included detailed micro-physics became possible with the foundation of the first high performance computational facilities. In the 1960s, panchromatic observations of the solar atmosphere became possible thanks to balloons and the first space missions. This allowed to constrain models by this broader wavelength interval.

*Semi-empirical models* are constructed using depth-dependent observations, like centre-to-limb continua variations and line profiles from many different species, to infer the temperature-pressure

stratification.

The first successful semi-empirical solar photosphere model was developed by Holweger and collaborators in the 1960s (Holweger, 1967; Holweger and Mueller, 1974). The HOLMUL atmosphere is a LTE model that has set the standard for years concerning abundance calculations (especially thanks to the fit to the Fe optical lines).

One of the first successful model that included the photosphere and the low chromosphere was the *Utrecht Reference Model* (Heintze et al., 1964). This model relied only on continuum observations, and presented the temperature minimum that is still a feature for 1D chromospheric models. The Utrecht model was subsequently improved (wider optical depth scale) with the *Bilderberg Continuum Atmosphere* (Gingerich and de Jager, 1968). Departures from LTE for hydrogen and calcium were taken into account for an improved model, the *Harvard-Smithsonian Reference Atmosphere* (Gingerich et al., 1971).

Following a similar approach to Holweger and Mueller (1974), and including the data from the Skylab space observatory and a large number of spectral lines, Vernazza et al. (1973, 1976, 1981) developed a semi-empirical model of the solar atmosphere that includes the chromosphere. The Vernazza et al. (1981) models are usually called *VAL*. The resulting temperature vs. height profile is displayed in Fig. 2.2. The graph also shows the formation height of several important lines, e.g. Lyman- $\alpha$  and H $\alpha$ , Mg II and Ca II doublets, and the continuum, from radio to far-UV. The model assumed a plane-parallel, time-independent, homogeneous atmosphere and included NLTE treatment for a large number of species (with only a small number of levels per species). Although it relied on very strong simplifying assumptions, the VAL atmosphere represented a reference for 1D chromospheric models for more than two decades and it has been progressively developed and refined, e.g. the *FAL* models by Fontenla et al. (1990, 1991, 1993).

Anderson and Athay (1989) expanded the levels and lines list used in the VAL model to include millions of spectral lines. They concluded that the bulk of the radiative losses originates from Fe II, with Ca II, Mg II, and H I playing an important but minor role.

Semi-empirical models have been very successful in reproducing observations, but they unfortunately cannot test the basic physics hidden behind the many free parameters that are usually required.

Static 1D models do not take into account the highly dynamical state of the upper atmosphere and cannot simulate the inhomogeneities and structures. Carlsson and Stein (1992, 1995) investigated the effect of acoustic waves in a 1D plane-parallel atmosphere using for their time rather detailed NLTE treatment for H, He and Ca. Acoustic waves propagate through the photosphere to the chromosphere and corona and deposit non-radiative energy. The wave's amplitude steepens while propagating upwards, and due to the lower density in the chromosphere, the velocity amplitude increases to conserve the wave energy flux. Eventually, shocks are formed and heat the gas. Their work confirmed the necessity of using NLTE radiative transfer and demonstrated that the "classical" transition region above the chromospheric temperature minimum is just a result of time-averaged models. They succeeded in modelling Ca II line profiles time-evolution but failed for other spectroscopic diagnostics, the reason likely being the lack of magnetic fields treatment, for which a 1D geometry is not suitable.

The treatment of small and large scales motions in 1D simulations relies often on strong simplifications and approximations. One example is the mixing-length theory (Böhm-Vitense, 1958): it treats turbulent eddies as isotropic and parametrizes the mixing length with a constant that is calibrated against solar observations. A proper 3D treatment that includes the upper region of the convective zone and the atmosphere, eliminates the free parameters, but it is still affected by many *a priori* assumptions (see Chapter 4).

Pioneering time-dependent, multi-dimensional hydrodynamic simulations of the solar photosphere were conducted by Nordlund (1982). Granulation and photospheric oscillations have been accurately simulated by Stein and Nordlund (1998). The radiative transfer for these simulations was treated

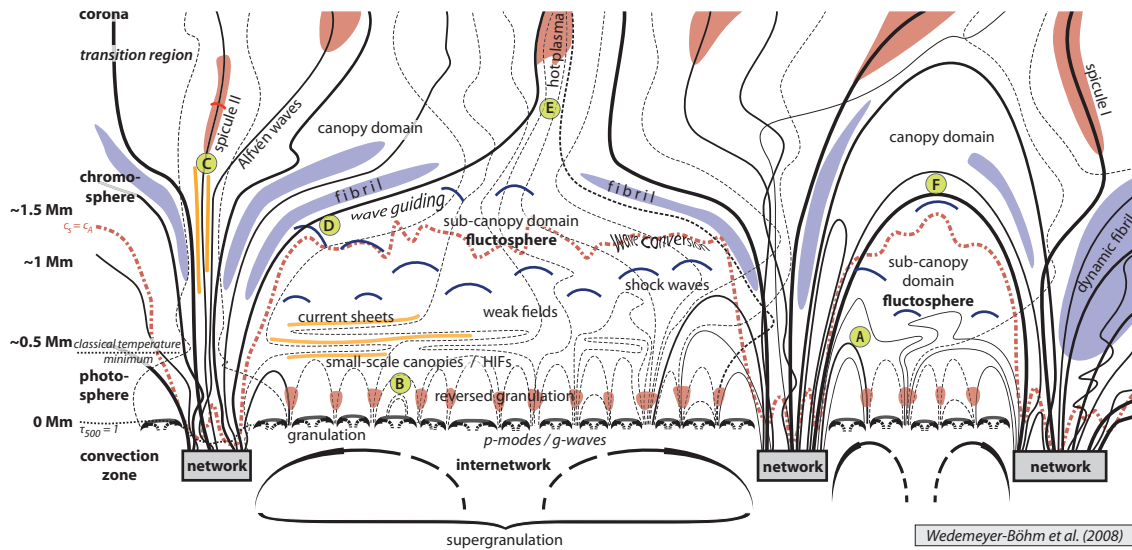


Figure 2.3: From Wedemeyer-Böhm et al. (2009): a schematic illustration of the structure and processes present in the quiet Sun outer layers.

using the *Opacity Binning method* (Nordlund, 1982) (see Chapter 4). The works mentioned above did not include scattering. This problem was addressed by Skartlien et al. (2000), who performed the first 3D hydrodynamic simulations extending from the convective zone to the low chromosphere.

High spatial and temporal resolution simulations were conducted by Wedemeyer et al. (2004) using the CO<sup>5</sup>BOLD code (Freytag et al., 2012). Their work, although preliminary for the modelling of the chromosphere due to several simplifying assumptions, revealed the importance of using high resolution spatial grids to properly model the small-scale structures of the chromosphere. In agreement with the results from Carlsson and Stein (1995), they suggest that the 1D temperature minimum can be explained as the outcome of spatial and temporal average. CO is formed in the lower chromosphere but does not play an important role for the thermal budget of the upper atmosphere (Wedemeyer-Böhm and Steffen, 2007).

Simulating 3D magneto-hydrodynamic (MHD) flows is a numerically demanding task, which can be tackled nowadays with the current computational facilities. Using the MURaM code, Vögler et al. (2005) performed high spatial and time resolution models of the upper convective zone and photosphere of the Sun. The simulation develops a magnetic structure similar to the one described in the previous section, with a magnetic network characterised by vertical field lines in correspondence with convective down-flows. Wedemeyer-Böhm et al. (2012) used the MHD version of CO<sup>5</sup>BOLD to simulate the solar chromosphere. They investigate the formation of chromospheric swirls and compare their simulations to multi-wavelength, high resolution observations. At the vertices of the intergranular lanes network, where gas flows downwards, vortex flows can be generated. At the same time, the magnetic field lines are arranged mostly vertically in the photospheric magnetic foot-points. There, the thermal gas pressure dominates over the magnetic pressure, and the plasma is essentially “frozen in”: the magnetic field lines are twisted, because they are forced to follow the rotation induced by the vortex flows. In the upper layers, where magnetic pressure dominates against gas pressure, the plasma follows the magnetic field and is lifted upwards. Finally, these *magnetic tornadoes* are likely responsible for a possibly significant but still not properly determined fraction of the heating of the transition region (see Fig. 2.3 for an illustration of the magnetic field structure in the solar atmosphere).

## M-dwarfs

Pioneering cool dwarf chromospheric models were produced by Kandel (1967), who concluded that a self-consistent, multi-level NLTE treatment for H and Ca I-II is necessary to properly predict the line profiles. Giampapa et al. (1982) constructed semi-empirical models, similar to the VAL atmosphere. They found out that a single component, homogeneous model fails to reproduce Ca II K and Mg II k lines, suggesting that the assumption of lateral homogeneity is unrealistic, and that a reasonable model would be a blend of active and quiet regions.

Using the Pandora code (an extended version of the code used in Vernazza et al., 1981), Mauas and Falchi (1994) computed semi-empirical models of the quiescent state of AD Leo (a nearby dMe, spectral type M3.5V; one of the most extensively observed flare stars); similarly, in Mauas and Falchi (1996), they modelled the flaring state of AD Leo. They estimate the flare's filling factor, the ratio between the flaring and quiet area on the stellar disk, to be approximately 1% (during major flares on the Sun, the H $\alpha$  flare area is approximately 0.01% of the solar disk).

With the same modelling framework, Falchi and Mauas (1998) performed a detailed review of some common assumptions in M-dwarfs chromosphere modelling. First, they underline the importance of including also minor species in NLTE treatment, especially to properly characterise the UV continuum. Second, they highlight the effects of including complete or partial frequency redistribution (CRD or PRD) treatment for Lyman- $\alpha$ : electron density in CRD is under-estimated, strongly affecting the line profile for H I transitions and other lines formed in the chromosphere, like the Ca II H&K doublet. To date, a consistent, multi-level treatment of PRD is still computationally very expensive.

Fuhrmeister et al. (2005, 2006) computed PHOENIX/1D models of mid- to late M-dwarfs. These models are constructed starting from an underlying photosphere and adding an artificial first shallow temperature rise for the chromosphere, and a steep rise for the transition region, to resemble the VAL chromosphere. They highlight the strong dependence of the chromospheric structure on the stellar parameters  $T_{\text{eff}}$  and  $\log g$ . They also review the inclusion of LTE background lines, i.e. species which opacities are computed assuming LTE population densities: they concluded that these species emission strengths are over-predicted in PHOENIX/1D models, consequently heavily influencing the ionisation balance for the NLTE species. Models of the spectra observed during a CN Leo (spectral type M5.5V) giant flare are discussed in Fuhrmeister et al. (2010). The simulations suggest that the filling factor during the impulsive phase is approximately 0.3%, and goes up to 2-3% at flare peak.

1D semi-empirical models for cool dwarfs are still developed nowadays, to improve the micro-physics and extend the computational domain to include also the transition region and the corona (Fontenla et al., 2016). However, only with 3D models we can consistently treat the radiative, hydrodynamic, and magnetic processes that are evidently present in the chromosphere.

The first 3D simulations of M-dwarf atmospheres focused on the convective envelope and the photosphere. Radiation-hydrodynamics simulations carried out by Ludwig et al. (2002) investigated the granulation and photospheric flows in late M-dwarfs (for which convective flows penetrate far into the atmosphere). They found out that the granulation pattern in their models did not qualitatively differ from the solar case, despite the large differences in stellar parameters. The horizontal scale for M-dwarf granulation is approximately one order of magnitude smaller than the solar case, in agreement with the difference in pressure scale heights. With a similar framework, Ludwig et al. (2006) investigated the efficiency of convective energy transport and compared it with the classical mixing-length theory. They conclude that synthetic models using the mixing-length parameter may overestimate the effective temperature (order of 200 K for M-dwarfs) when compared to RHD models. Freytag et al. (2010) further investigated convection and dust formation in M-dwarf and brown dwarf atmospheres with 2D CO<sup>5</sup>BOLD simulations: they suggest that gravity waves, and not over-shooting, are playing a major role in the mixing of the outer layers. Wende et al. (2009) computed a grid of CO<sup>5</sup>BOLD models to investigate the relation between velocity fields and FeH line shapes in M-dwarf

photospheres. Their study reveals a strong dependence of the velocity fields on  $\log g$  and  $T_{\text{eff}}$ : the velocity dispersion becomes larger for decreasing surface gravity and increasing effective temperature. Moreover, 1D spectral synthesis methods, including micro- and macro-turbulence, well reproduce the 3D line profiles. Beeck et al. (2013) investigated the connection between convective flows, granulation and line profiles in MHD simulations of cool dwarfs, including M-dwarfs: they suggest that the observed, disk-integrated line profiles carry the signature of the complex 3D structure, while line-asymmetries are mainly modulated by stellar (differential) rotation.

The simulations discussed above included only the photosphere. Wedemeyer et al. (2013) extended the model grid from Ludwig et al. (2006) including also the chromosphere. I discuss these models in greater detail in Chapter 4.

### 2.3 Do we really need 3D NLTE models?

As mentioned above, 1D models are still largely used to compare and calibrate observations, with good, if not excellent, results, depending on the problem we address. However, 1D NLTE calculations, performed with a large number of NLTE atomic species, LTE background opacities, a detailed equations of state solver, and high wavelength resolution, are still computationally non-trivial. A practical example: PHOENIX/1D NLTE models require several hundred hours of CPU time to converge, which means that, nowadays, we still cannot compute PHOENIX/1D spectra “on-the-fly” on typical office computers. This is tremendously complicated when we add two more dimensions, with computational times going up to millions and more CPU hours.

Although the high technical costs of these simulations, the answer to the headline question is *yes*. Stellar atmospheres naturally feature NLTE conditions, with LTE being only valid in very specific cases. Even the photosphere of the Sun, a relatively quiet G2-dwarf, needs NLTE treatment in order to properly estimate the metallicity. In fact, 3D simulations give different results than 1D models. For instance, the solar metallicity would be sub-solar if we would use the 1D calculations as reference (Asplund, 2005). On the same topic, Pereira et al. (2013) compared different 1D and 3D models with observational diagnostics for the Sun: they concluded that the 3D models reproduce the observables much better than the 1D counterpart. Finally, for realistic simulations of the chromosphere, NLTE multi-level treatment is basically mandatory, and the inhomogeneities and dynamical processes discussed above require a 3D, time-dependent approach.



## Chapter 3

# Radiative transfer concepts

This chapter is a brief introduction to radiative transfer theory. I refer mostly to classical reviews and texts about the topic, Rutten (2003) and Hubeny and Mihalas (2015), from which the mathematical notation was based on, PhD theses from the Hamburger Sternwarte, mainly van Rossum (2009) and Berkner (2015), and the PHOENIX/3D paper series (Hauschildt and Baron, 2014, and previous).

### 3.1 The radiative transfer equation

The amount of energy  $dE_\lambda$  transported by radiation through a surface  $dA$ , in a wavelength range from  $\lambda$  to  $\lambda + d\lambda$ , between time  $t$  and  $t + dt$ , is defined as

$$dE_\lambda = I_\lambda(\vec{r}, \vec{n}, t) \cos \theta dA dt d\Omega d\lambda, \quad (3.1)$$

with  $I_\lambda(\vec{r}, \vec{n}, t)$  being the specific intensity of the radiation field at time  $t$  and position  $\vec{r} = \vec{r}(x, y, z)$ , in the direction  $\vec{n} = \vec{n}(\theta, \phi)$ ,  $\theta$  the polar angle, measured from the surface normal to the direction  $\vec{n}$ ,  $\phi$  the azimuthal angle, and  $d\Omega$  the solid angle with coordinates  $\theta$  and  $\phi$  (see Fig. 3.1). Along the beam, matter may emit and scatter photons into the light beam, or absorb and scatter them away. For the first case, we define the *emissivity*  $\eta_\lambda(\vec{r}, \vec{n}, t)$  so that the energy added to the radiative beam is

$$dE_\lambda^{\text{add}} = \eta_\lambda(\vec{r}, \vec{n}, t) ds dA dt d\Omega d\lambda, \quad (3.2)$$

where  $ds$  is the thickness of the irradiated slab. For the second case, we define the *extinction* (or *opacity*)  $\chi_\lambda(\vec{r}, \vec{n}, t)$  so that the energy removed from the beam is

$$dE_\lambda^{\text{rem}} = \chi_\lambda(\vec{r}, \vec{n}, t) I_\lambda(\vec{r}, \vec{n}, t) ds dA dt d\Omega d\lambda, \quad (3.3)$$

The energy sinks and sources sum up linearly, therefore  $dE_\lambda = dE_\lambda^{\text{add}} + dE_\lambda^{\text{rem}}$ . More details concerning the physical processes hidden inside  $\eta_\lambda$  and  $\chi_\lambda$  are explained in Section 3.2.

If we consider a beam of radiation with specific intensity  $I_\lambda(\vec{r}, \vec{n}, t)$  entering a slab of material with cross section  $dA$  and length  $ds$ , at time  $t + dt$  the intensity has changed by an amount equal to the energy introduced into the beam by in-scattering and emission minus the energy scattered-out or absorbed. Therefore,

$$[I_\lambda(\vec{r} + \Delta\vec{r}, \vec{n}, t + dt) - I_\lambda(\vec{r}, \vec{n}, t)] dA d\Omega d\lambda dt = [\eta_\lambda(\vec{r}, \vec{n}, t) - \chi_\lambda(\vec{r}, \vec{n}, t) I_\lambda(\vec{r}, \vec{n}, t)] dA ds d\Omega d\lambda dt, \quad (3.4)$$

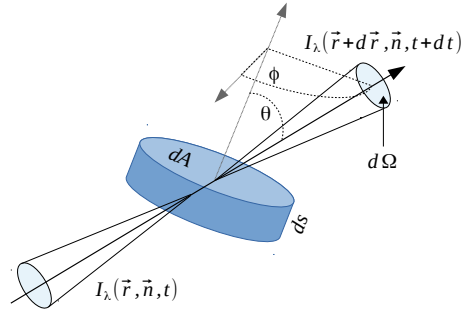


Figure 3.1: Scheme of the radiation transfer.

which we can rewrite as

$$\frac{dI_\lambda(\vec{r}, \vec{n}, t)}{ds} = \eta_\lambda(\vec{r}, \vec{n}, t) - \chi_\lambda(\vec{r}, \vec{n}, t)I_\lambda(\vec{r}, \vec{n}, t). \quad (3.5)$$

Eq. 3.5 is the *radiative transfer equation* in a general form.

Several useful quantities can be calculated from the specific intensity. The average of  $I_\lambda$  over all solid angles is called *mean intensity*

$$J_\lambda(\vec{r}, t) = \frac{1}{4\pi} \int I_\lambda d\Omega = \frac{1}{4\pi} \int_0^{2\pi} \int_0^\pi I_\lambda \sin \theta d\theta d\phi. \quad (3.6)$$

This quantity is useful when evaluating the amount of radiative energy in a specific location, regardless of its origin. To quantify the rate of radiative energy flowing through a surface per wavelength unit, we define the (*monochromatic*) *radiative flux*  $\vec{F}_\lambda$  as the vector

$$\vec{F}_\lambda(\vec{r}, t) = \int I_\lambda \vec{n} d\Omega. \quad (3.7)$$

In order to provide a general and comparable description of the radiative transfer problem, it is helpful to work with numerical scales that carry the physical information without depending on the metric distances considered. The *source function* is defined as the ratio between total emissivity and total opacity

$$S_\lambda = \frac{\eta_\lambda}{\chi_\lambda}. \quad (3.8)$$

The *optical depth* is defined as

$$d\tau_\lambda = -\chi_\lambda ds. \quad (3.9)$$

Thanks to the source function and optical depth definitions, we can now simplify Eq. 3.5 into

$$\frac{dI_\lambda}{d\tau_\lambda} = I_\lambda - S_\lambda. \quad (3.10)$$

This compact version of the radiative transfer equation along a path (also called *characteristic*) is extremely useful to further develop the theory, and its derivation and building blocks can be generalised to more cases.

Eq. 3.10 can be directly solved if  $\eta_\lambda$  and  $\chi_\lambda$ , which in general depend on the radiation field, are given (a so called *formal solution*). This equation is a first-order linear differential equation, which solution is

$$I_\lambda(\tau_\lambda) = I_\lambda(0)e^{-\tau_\lambda} + \int_0^{\tau_\lambda} S_\lambda(t)e^{t-\tau_\lambda} dt. \quad (3.11)$$

## 3.2 Photons and particles

With Eqs. 3.2 and 3.3, I introduced the emissivity and extinction, two intensive properties tightly connected to the physico-chemical conditions of the gas *and* the radiation flowing through it. In this section, I briefly describe some of the many physical processes hidden behind  $\eta_\lambda$  and  $\chi_\lambda$ .

Stellar atmospheres are predominately gaseous. A gas (more correctly, a *gas mixture*) may contain free electrons, neutral and ionised atoms, neutral and ionised molecules, and condensates. We can describe the conditions of the gas following a statistical approach. For each species in our mixture, the number density of particles  $N$  for that species is determined by  $N = \sum_{i,s} n_{i,s}$ , where  $n_{i,s}$  is the concentration of particles in the excitation level  $i$  and ionisation stage  $s$ , also called *population density*. The kinetics are fundamental to the thermodynamic properties of the gas and they are often treated in a semi-classical way, i.e. particles' positions and velocities are not quantised, while the electromagnetic micro-physical states are described by quantum mechanics. The  $n_{i,s}$  are set by several physical processes that we can generally divide in two classes: particle-photon and particle-particle interactions. Theoretically, higher orders can be included, like three body collisions, etc.

### Photon-scattering

Photon-scattering is an interaction between photons and particles. Within the non-relativistic energy range concerning stellar atmospheres, photon-scattering leaves the scattering centre (free or bound electron) substantially unaltered while the photon may change direction and/or frequency.

Photon-scattering on free electrons is called *Thomson scattering*. Its non-relativistic cross section is

$$\sigma_T = \frac{8\pi e^4}{3m_e^2 c^4} = 6.65 \times 10^{-25} \text{ cm}^2, \quad (3.12)$$

where  $e$  is the electron charge,  $m_e$  the electron mass, and  $c$  the speed of light. Thomson scattering is coherent, i.e. the frequency is unaltered, and anisotropic: the intensity of the scattered radiation has an angular dependence, that is not all outgoing directions have the same probability. However, Thomson scattering is normally treated as isotropic, an approximation that does not critically influence the calculations, especially when compared with other important sources of uncertainty (see Hubeny and Mihalas, 2015, Chapter 12, for more details). It is the main source of continuum opacity for stellar atmospheres with a large pool of free electrons, i.e. high degree of ionisation. For late-type stars, later than G, the ionisation level for hydrogen and metals is, on average, low, and Thomson scattering is important only in the deeper layers of the atmosphere, or in localised regions with ionised gas, like chromospheric shock fronts.

Photons may scatter with bound electrons in atoms and molecules, a process called *Rayleigh scattering*. A photon can excite a bound electron to a virtual state, which creates a photon with identical energy once it decays. Like Thomson scattering, Rayleigh scattering is coherent and anisotropic (but often approximated as isotropic), and the cross section is typically described by

$$\sigma_{R,\lambda} \propto f_{ij} \sigma_T \left( \frac{\lambda_{ij}}{\lambda} \right)^4, \quad (3.13)$$

where  $f_{ij}$  and  $\lambda_{ij}$  represent the oscillator strength and the wavelength, respectively, of the strongest resonance transition for the bound electron, e.g. Lyman- $\alpha$  for neutral hydrogen. Rayleigh scattering by neutral H and He is important for stars from late B-type to late G-type, while Rayleigh scattering on  $\text{H}^-$  and  $\text{H}_2$  are important sources for cool stars, from spectral types late F to M.

### Bound-bound transitions

With *radiative bound-bound transitions* we refer to interactions between bound electrons and photons that lead to a change in the quantum properties of the electron, but without altering the ionisation stage of the atom. The transition happens between two states  $i$  and  $j$  ( $i < j$ ), with an energy difference  $\Delta E = E_j - E_i = hc/\lambda_{ij}$ , where  $h$  is the Planck constant and  $\lambda_{ij}$  is the transition wavelength. The possible transitions are

- *radiative excitation / absorption*: a photon gets destroyed and an electron switches from the state  $i$  to the state  $j$ , to account for energy and quantum numbers differences;
- *radiative de-excitation / spontaneous emission*: decay of an excited state  $j$  to a lower state  $i$ , creating a photon;
- *induced radiative de-excitation / induced emission*: a photon induces a de-excitation, creating a second photon in coherence with the first one.

For these processes, the transition rates are expressed by the Einstein coefficients:  $B_{ij}$  for absorption,  $A_{ji}$  for spontaneous emission, and  $B_{ji}$  for induced emission. These coefficients are defined by

$$A_{ji} = \frac{2hc}{\lambda_{ij}^3} B_{ji} \quad \text{and} \quad g_i B_{ij} = g_j B_{ji},$$

where  $g_i$  ( $g_j$ ) is the degeneracy of the state  $i$  ( $j$ ).  $A_{ji}$  has the units of a frequency, and  $A_{ji}^{-1}$  is usually called the *life-time* of the transition.

The cross section for absorption is

$$\alpha_{ij,\lambda} = \frac{h\lambda}{4\pi c} B_{ij} \Phi_{ij,\lambda}(\vec{n}), \quad (3.14)$$

while for spontaneous emission we have

$$\alpha_{ji,\lambda} = \frac{h\lambda}{4\pi c} B_{ji} \Psi_{ji,\lambda}(\vec{n}), \quad (3.15)$$

with  $\Phi_{ij,\lambda}$  and  $\Psi_{ji,\lambda}$  the absorption and emission line profile, respectively.

Treating together absorption and induced emission, being both dependent on the intensity, the absorption coefficient is

$$\kappa_{ij,\lambda}(\vec{n}) = \alpha_{ij,\lambda} n_i \left( 1 - \frac{\alpha_{ji,\lambda} g_i n_j}{\alpha_{ij,\lambda} g_j n_i} \right), \quad (3.16)$$

while the emission coefficient is

$$\eta_{ji,\lambda}(\vec{n}) = \frac{2hc^2}{\lambda^5} \frac{g_i}{g_j} \alpha_{ji,\lambda} n_j. \quad (3.17)$$

Eq. 3.14 includes the absorption line profile, which represents the probability distribution function of absorbing a photon at a specific wavelength for a bound-bound transition (similar description for the emission line profile in Eq. 3.15). Several micro- and macroscopic processes, usually called *line broadening* mechanisms, contribute to the shape of the line: the uncertainty principle, collisions with other particles, turbulence, convective flows, stellar rotation, electric or magnetic fields, and many other (see Rutten, 2003, and Hubeny and Mihalas, 2015, for in-depth discussion).

In Eqs. 3.16 and 3.17, we can drop the dependency on  $\vec{n}$ , i.e. the emission and absorption profiles may be angle-averaged, if the gas particles are isotropically distributed. If the atoms experience frequent collisions with other particles, the excited states are constantly perturbed, and absorbed and emitted photons are substantially uncorrelated (the excited states do not have “memory”). We can, therefore, assume that  $\Phi_{ij,\lambda} = \Psi_{ji,\lambda}$ , i.e. the absorption and emission profiles for a specific transition are identical. Consequently,  $\alpha_{ij,\lambda} = \alpha_{ji,\lambda}$ . This approximation is called *complete frequency redistribution* (CRD): photons are redistributed throughout the full line profile. CRD is a helpful approximation because it allows us to treat upwards and downwards transitions alike, for example in Eqs. 3.16 and 3.17, greatly decreasing the computational effort concerning line radiative transfer.

However, *partial frequency redistribution* (PRD) effects gain significance in low density media and for strong or resonance lines, like Lyman- $\alpha$ . In the latter case, the Lorentzian contribution to the line profile is strong and heavily influences the line wings. Consequently, radiative damping is more effective than collisional damping and, in the wings, the photons are more likely trapped, rather than being redistributed towards the line core: as a result, wings’ photons behave diffusively, influencing the line source function on spatial scales much larger than the photon mean free path (see Hubeny and Mihalas, 2015, Chapter 15, for in-depth treatment of the PRD). From here on, I only consider the CRD scenario.

### Bound-free and free-free transitions

Radiative interactions can change the ionisation stage of atoms and molecules. *Photo-ionisation* involves the destruction of a photon to release a bound electron. Free electrons can take any value of energy, the so called *continuum* (if the gas is not degenerate). The inverse process is *recombination*. These transitions are called *bound-free*, and represent an important source of opacity for wavelengths close to the ionisation threshold.

*Free-free* transitions occur between unbound states and, therefore, do not influence the populations and the statistical equilibrium. *Bremsstrahlung* (“braking radiation”) is the outcome of interactions between charged particles: electrons “feel” the electric field of ions and get decelerated, emitting photons. Thanks to time-invariance, the inverse process is also possible: we have, therefore, free-free emission and absorption.

Depending on the wavelength, bound-free and free-free opacities are strongly related to the gas temperature and, therefore, to the influence of the most abundant nuclei.

### Collisions

In any gas, particles collide with each other all the time. Collisions may be frequent or rare in comparison to radiative transitions: in the first case, statistical mechanics provides simple relations between the states and the thermodynamic properties of the gas (mainly temperature and density); in the second case, the treatment gets complicated and analytical approaches are limited to few simple cases, with numerical solutions being the most suitable approach.

*Collisional excitation* or *de-excitation* of bound electrons may happen through collisions with other particles. For stellar atmospheres, collisions with free electrons is generally the most important collisional process. Electrons are very light compared to any other species, resulting in high relative velocities and, consequently, higher collisional rates. Moreover, the high degree of ionisation of hydrogen provides a large pool of free electrons. For cool stars, hydrogen ionisation in the atmosphere decreases but free electrons are still provided by lowly ionised abundant metals; however, in this case, collisions between neutral species must also be taken into account.

Collisions may also alter the ionisation stage:

- *spontaneous recombination*: an ionised atom captures a free electron; a photon is created;
- *collisional ionisation*: a bound electron is “kicked out” by the collision, ionising the host species;
- *induced recombination*: a recombination catalysed by a photon, thus depending on the radiation field; it is a high order interaction, therefore, less probable.

### Thermodynamic equilibrium

*Thermodynamic equilibrium* (TE) represents the ideal case in which all the gas constituents, particles and photons, are in their most probable macro-state due to random, uncorrelated collisions. In TE, the gas is a closed system, and all properties can be described by one single macroscopic parameter, the temperature  $T$ .

In TE, the energy distribution of the photons is described by the *Planck* formula

$$B_{\lambda}(T) = \frac{2hc^2}{\lambda^5} \left( \exp \left[ -\frac{hc/\lambda}{kT} \right] - 1 \right)^{-1}, \quad (3.18)$$

where  $k$  is the Boltzmann constant.

TE is a good approximation for stellar interiors (not stellar cores, where energy is actively generated), because particle-particle and photon-particle interactions are extremely frequent and photons are effectively trapped. An important property of TE is *detailed balance*: each process is equilibrated by its reverse.

In the outer layers of a star, e.g. the stellar atmosphere, particles may still be thermalised while photons will not be perfectly thermalised because they are more likely to meet the boundary and leave the star. Therefore, the radiation field may be different from the Planckian one (Eq. 3.18), but the collisional processes still dominate over the radiative ones. This case is called *local thermodynamic equilibrium* (LTE).

In LTE, detailed balance still holds for the gas particles, as long as the *radiative imbalance* does not influence the Saha-Boltzmann equilibrium or the thermalisation proceeds too slowly. Moreover, while the photons distribution function is not strictly dependent uniquely on the local temperature, the material particles distribution function still is. Particles velocities are set by the Maxwell velocity distribution. The LTE population densities  $n_{i,s}^*$  for the level  $i$ , in the ionisation stage  $s$ , are defined by the Boltzmann equation

$$\frac{n_{i,s}^*}{n_{j,s}^*} = \frac{g_{i,s}}{g_{j,s}} \exp\left[-\frac{hc/\lambda_{ij}}{kT}\right]; \quad (3.19)$$

the ionisation ratios are set by the Saha equation

$$\frac{N_{s+1}^*}{N_s^*} = \frac{2}{n_e} \frac{Q_{s+1}}{Q_s} \left(\frac{2\pi m_e kT}{h^2}\right)^{3/2} \exp\left[-\frac{\xi_s - \xi_{s+1}}{kT}\right], \quad (3.20)$$

where  $\xi_s$  is the ionisation potential, and  $Q_s$  the partition function

$$Q_s = \sum_i g_{i,s} \exp[-E_{i,s}/kT], \quad (3.21)$$

with  $E_{i,s}$  being the excitation potential. Combining Eqs. 3.18 and 3.19 we obtain the Saha-Boltzmann equation for the population densities

$$n_i^* = 2n_\kappa n_e \frac{g_i}{g_\kappa} \left(\frac{h^2}{2\pi m_e kT}\right)^{3/2} \exp\left[-\frac{E_i - E_\kappa}{kT}\right], \quad (3.22)$$

where  $\kappa$  is the ground state of the next ionisation stage.

If the LTE assumptions fail, the gas is in *non-LTE* (NLTE) conditions. For stellar atmospheres, NLTE conditions allow for the population densities to differ from the Saha-Boltzmann values, while a single Maxwell velocity distribution for the gas is still a good approximation (see Hubeny and Mihalas, 2015, p. 112).

It is standard practice to compare the actual conditions of the gas to those of the ideal LTE case. For quantitative reasoning, we can define, for each level  $i$  in the ionisation stage  $s$ , the *departure coefficient*  $b_{i,s}$  (following the definition from Mihalas, 1978):

$$b_{i,s} = \frac{n_{i,s}}{n_{i,s}^*}, \quad (3.23)$$

with  $n_{i,s}$  being the actual population density and  $n_{i,s}^*$  the LTE value given by Eq. 3.22.

### Collisional rates

The *collisional excitation* rate, taking into account only collisions with free electrons, can be described as

$$C_{ij} = n_e \int_{v_{th}}^{\infty} \alpha_{e,ij}(v) v f(v) dv = n_e q_{ij}(T), \quad (3.24)$$

where  $n_e$  is the electron density,  $\alpha_{e,ij}$  the cross section,  $f(v)$  the velocity distribution of the particles,  $v_{th}$  the threshold velocity for the process, and  $q$  the rate coefficient.

A very general treatment of Eq. 3.24 is complicated. Equilibrium assumptions are helpful for collisionally-dominated processes (LTE-rates). First, by assuming detailed balance and Maxwellian velocity distribution for the particles, the collisional excitation and de-excitation rates are straightforwardly

$$n_i^* C_{ij} = n_j^* C_{ji}, \quad (3.25)$$

from which we get

$$n_j C_{ji} = n_j \frac{n_i^*}{n_j^*} C_{ij}. \quad (3.26)$$

This “constrains” the problem to measure or theoretically compute the rate coefficient  $q_{ij}(T)$  (Itikawa, 2003).

### Opacity and emissivity

We can combine all the processes responsible for removing photons from the beam into the total extinction  $\chi_\lambda$ . Assuming isotropy for each extinction and emission process, we get

$$\chi_\lambda = \sum_{i \neq j} \kappa_{ij,\lambda} + \kappa_{bf,\lambda} + \kappa_{ff,\lambda} + \sigma_\lambda, \quad (3.27)$$

where  $\kappa_{bf,\lambda}$ ,  $\kappa_{ff,\lambda}$ , and  $\sigma_\lambda$  describe the background bound-free, free-free, and scattering contribution, respectively. Likewise, for the processes contributing to the total emissivity  $\eta_\lambda$ , we have

$$\eta_\lambda = \sum_{i \neq j} \eta_{ij,\lambda} + \eta_{bf,\lambda} + \eta_{ff,\lambda} + \sigma_\lambda J_\lambda. \quad (3.28)$$

In the idealised LTE case, emissivity and absorptivity are balanced. Including scattering, we obtain

$$\eta_\lambda = \kappa_\lambda B_\lambda + \sigma_\lambda J_\lambda. \quad (3.29)$$

In this case, we can re-write the source function (Eq. 3.8) as

$$S_\lambda = \frac{\kappa_\lambda B_\lambda + \sigma_\lambda J_\lambda}{\kappa_\lambda + \sigma_\lambda}. \quad (3.30)$$

From Eq. 3.27, we can define the *thermal coupling parameter*  $\epsilon_\lambda$  as

$$\epsilon_\lambda = \kappa_\lambda / \chi_\lambda. \quad (3.31)$$

$\epsilon_\lambda$  can be interpreted as a probability: with  $\epsilon_\lambda \sim 1$ , a photon experiences no scattering, and therefore it is created and destroyed locally, its energy returned to the thermal pool (almost) instantaneously; with  $\epsilon_\lambda \ll 1$ , or  $(1 - \epsilon_\lambda) \sim 1$ , a photon experiences multiple scattering events before escaping or being absorbed, and can transport information about its creation place over large distances across the atmosphere. In the first case, for very optically thick gas, Eq. 3.30 becomes  $S_\lambda \approx B_\lambda$ . In the second case, the gas-radiation equilibrium will be de-localised, and the particles will “feel” a radiation field that differs strongly from the local  $B_\lambda$ .

## 3.3 Kinetic equilibrium

To solve the radiative transfer equation we must calculate the opacity and for that we have to calculate the atomic level populations for each species considered. In atmosphere models, *kinetic equilibrium* is a common assumption: all the populating and de-populating processes, for excitation and ionisation states, are balanced, i.e. all the processes are time-independent. Therefore, for a certain ionisation stage, for a level  $i$ , we have

$$n_i \sum_{j \neq i} (R_{ij} + C_{ij}) = \sum_{j \neq i} n_j (R_{ji} + C_{ji}), \quad (3.32)$$

where the left (right) side of the equation gives the number of transitions in (out) of the level  $i$ , and  $R_{ij}$  and  $C_{ij}$  represent respectively radiative and collisional rates in the transition. Using Eq. 3.24, we

can re-write Eq. 3.32 in a slightly different way that highlights the dependency from the population densities of any state  $j$  for a specific state  $i$

$$n_i \left( \sum_{j>i} (R_{ij} + C_{ij}) + \sum_{j<i} \left( \frac{n_j}{n_i} \right)^* (R_{ij} + C_{ji}) \right) = \sum_{j<i} n_j (R_{ji} + C_{ji}) + \sum_{j>i} n_j \left( \frac{n_i}{n_j} \right)^* (R_{ji} + C_{ij}), \quad (3.33)$$

with  $(n_i/n_j)^*$  being the LTE population densities ratios.

### Radiative rates

The radiative rates are divided into absorption and emission rates for each transition.

For bound-bound-upwards transitions, the radiative rates depend on the absorption coefficient, the line profile (assuming CRD, absorption and emission profiles are identical) and the mean intensity

$$R_{ij} = B_{ij} \int \Phi_{ij,\lambda} J_\lambda \lambda d\lambda. \quad (3.34)$$

For bound-bound-downwards transitions, we have to include spontaneous emission and induced emission

$$R_{ji} = A_{ji} + B_{ji} \int \Phi_{ij,\lambda} J_\lambda \lambda d\lambda. \quad (3.35)$$

It is advantageous to combine bound-bound and bound-free processes in one single notation and to use the definitions of absorption and emission cross sections defined above (Eqs. 3.14 and 3.15). For upwards transitions, where  $j$  refers to a bound or a free state, we get

$$R_{ij} = \frac{4\pi}{hc} \int \alpha_{ij,\lambda} J_\lambda \lambda d\lambda, \quad (3.36)$$

while for downwards transitions, we obtain

$$R_{ji} = \frac{4\pi}{hc} \int \alpha_{ji,\lambda} \left( \frac{2hc^2}{\lambda^5} + J_\lambda \right) \exp\left(-\frac{hc/\lambda}{kT}\right) \lambda d\lambda. \quad (3.37)$$

To finalise Eq. 3.33, we use the collisional rates from Eq. 3.26. The system of equations is then closed by particle and charge conservation. Equation 3.33 is evidently non-linear, with the radiative rates depending on the populations densities that we actually want to find, and depending on the electron number density through the collisional rates.

## 3.4 Iterative solutions

As already mentioned, the NLTE radiative transfer problem is non-linear. Direct and indirect approaches are both necessary to address the problem. Iterative schemes are general and computationally efficient indirect methods providing accurate solutions.

The formal solution in Eq. 3.11 can be rewritten into operator form, called  $\Lambda$ -operator, that acts on the source function

$$I_\lambda(\mu) = \Lambda(\mu) [S_\lambda]. \quad (3.38)$$

Consequently, by averaging over the angles, we calculate the mean intensity as

$$J_\lambda = \Lambda [S_\lambda], \quad (3.39)$$

which we can solve with any method imaginable, once we express the “building blocks” of the source function.

If we assume LTE conditions, and isotropic and coherent scattering, combining Eqs. 3.30 and 3.31, we obtain

$$S_\lambda = (1 - \epsilon_\lambda)J_\lambda + \epsilon_\lambda B_\lambda. \quad (3.40)$$

We can now re-write the mean intensity in terms of the  $\Lambda$ -operator and the just defined source function as

$$J_\lambda = \Lambda [S_\lambda] = \Lambda [(1 - \epsilon_\lambda)J_\lambda] + \Lambda [\epsilon_\lambda B_\lambda], \quad (3.41)$$

which we could solve directly. Unfortunately this is computationally prohibitively demanding, especially in multi-dimensional problems, because we would have to invert the (rather large) matrix of the  $\Lambda$ -operator.

An iterative scheme, the so-called  $\Lambda$ -iteration scheme, was proposed to overcome this difficulty. We make up an initial estimate for  $J_\lambda = J_\lambda^{(0)}$  (a typical choice is  $J_\lambda^{(0)} = B_\lambda$ , a first guess that is definitely reasonable for stellar atmospheres). We then compute a new  $J_\lambda^{(1)}$  using Eq. 3.41, obtaining

$$J_\lambda^{(1)} = \Lambda [(1 - \epsilon_\lambda)J_\lambda^{(0)}] + \Lambda [\epsilon_\lambda B_\lambda]. \quad (3.42)$$

$\Lambda$  is now “operating” on known integrands and we can integrate to obtain  $J_\lambda^{(1)}$ . We can repeat this  $n$  times to get

$$J_\lambda^{(n+1)} = \Lambda [(1 - \epsilon_\lambda)J_\lambda^{(n)}] + \Lambda [\epsilon_\lambda B_\lambda]. \quad (3.43)$$

We could write the previous equation in terms of the source function

$$S_\lambda^{(n+1)} = (1 - \epsilon_\lambda)\Lambda [S_\lambda^{(n)}] + \epsilon_\lambda B_\lambda. \quad (3.44)$$

This seems promising at first glance, but unfortunately math strikes back. From Eq. 3.44, we can see that successive corrections of  $S_\lambda$ , i.e.  $S_\lambda^{(n+1)} - S_\lambda^{(n)}$ , are of the order  $(1 - \epsilon_\lambda)^n$  relative to  $B_\lambda$ . This iterative scheme may work reasonably well for atmospheres where scattering is weak, i.e.  $\epsilon \approx 1$ , but it is slow, or will completely fail, if the atmosphere is *scattering-dominated*, i.e.  $(1 - \epsilon) \approx 1$ .

To overcome this problem, Cannon (1973) proposed a new iterative scheme using an *approximate*  $\Lambda$ -operator and the *operator splitting* method: we can iteratively solve a linear system  $Ax = b$  by splitting  $A$  into two operators,  $A = M - N$ , and derive the iterative form  $Mx^{n+1} = Nx^n + b$  (similarly to the classical Jacobi or Gauss-Seidel iterative schemes). As already stated, the linear system  $Ax = b$  could also be solved directly, but the inversion of the matrix  $A$  is generally computationally costly, especially for multi-dimensional problems.

We split  $\Lambda$  in two parts

$$\Lambda = (\Lambda - \Lambda^*) + \Lambda^*, \quad (3.45)$$

with  $\Lambda^*$  being an operator that *approximates*  $\Lambda$  in the most convenient way with respect to the overall computational time. We can rewrite Eq. 3.44 and apply the iterative scheme

$$S_\lambda^{(n+1)} = (1 - \epsilon_\lambda)(\Lambda - \Lambda^*) [S_\lambda^{(n)}] + (1 - \epsilon_\lambda)\Lambda^* [S_\lambda^{(n+1)}] + \epsilon_\lambda B_\lambda, \quad (3.46)$$

where now  $(\Lambda - \Lambda^*)$  is operating on the previous state of the source function, while  $\Lambda^*$  operates on the new source function. For each iterative step, this solution is evidently approximate, but it is exact in the convergence limit, i.e.  $S_\lambda^{(n+1)} = S_\lambda^{(n)}$ , as long as convergence is achieved. We can rewrite Eq. 3.46 using an intermediate value of the source function calculated through a formal solution of the  $n$ -th iteration of  $S_\lambda$ ,

$$S_\lambda^{\text{FS}} = (1 - \epsilon_\lambda)\Lambda [S_\lambda^{(n)}] + \epsilon_\lambda B_\lambda, \quad (3.47)$$

obtaining

$$(1 - (1 - \epsilon_\lambda)\Lambda^*) [S_\lambda^{(n+1)}] = S_\lambda^{\text{FS}} - (1 - \epsilon_\lambda)\Lambda^* [S_\lambda^{(n)}]. \quad (3.48)$$

From here, it is straightforward to derive that the successive corrections of the source functions are

$$S_\lambda^{(n+1)} - S_\lambda^{(n)} = (1 - (1 - \epsilon_\lambda)\Lambda^*)^{-1} [S_\lambda^{\text{FS}} - S_\lambda^{(n)}], \quad (3.49)$$

where we see that convergence is actually *accelerated* for values of  $(1 - \epsilon) \approx 1$ , but at this point the employed definition of  $\Lambda^*$  is still unaccounted for. Without going into a thorough discussion here, we only mention the seminal work from Olson et al. (1986) who suggests that a good choice for  $\Lambda^*$  is simply the diagonal part of the exact  $\Lambda$ , because of the simple matrix inversion, but this may lead to slow convergence.

The operator splitting method is also used to solve the radiative rates equation (Eq. 3.33). We define the *rate-operator* for upwards transitions  $[R_{ij}]$ , and the *population density operator*  $[n]$ , so that the rate  $R_{ij}$  is

$$R_{ij} = [R_{ij}][n]. \quad (3.50)$$

We can then use an approach similar to the  $\Lambda$ -operator scheme to solve iteratively the radiative rates equation (Eq. 3.33). The method described here was suggested by Rybicki and Hummer (1991) and explained, e.g., in Hauschildt and Baron (2014).

We can finally outline our strategy to iteratively solve the multi-level NLTE problem: guess initial values for the population and electron densities; solve the radiative transfer equation and update the radiative rates with  $\Lambda$  and  $\Lambda^*$ ; solve the rate equations to obtain the new populations densities; calculate the new population and electron densities; iterate until convergence.

## Chapter 4

# Computational framework

As mentioned in the Introduction, the goal of this work was to compute the radiative properties of M-dwarfs chromospheres with a 3D NLTE framework. For this purpose, I used the PHOENIX/3D code and pre-computed atmospheric models. Through a collaboration with Sven Wedemeyer (University of Oslo), we obtained high resolution M-dwarf MHD models, calculated with CO<sup>5</sup>BOLD.

In this chapter, I present the technical features of the PHOENIX/3D code, briefly introduce the MHD code CO<sup>5</sup>BOLD, and then describe the M-dwarf models used for the simulations discussed in the next chapters.

### 4.1 PHOENIX

PHOENIX is a general purpose model atmosphere code. It can simulate stellar atmospheres and compute the emergent spectra for a wide range of astrophysical objects, e.g. planets, dwarfs and giant stars (also with winds and irradiation), novae and supernovae, AGNs and disks. Other important applications are the computation of opacity tables and limb-darkening coefficients.

The code provides two different modes: PHOENIX/1D and PHOENIX/3D. The two modes share the same micro-physics treatment, i.e. equations of state, LTE opacity, multi-level NLTE treatment for ions and molecules. The geometry differs between the two modes: with PHOENIX/1D we can solve the time-dependent, special relativistic, radiative transfer problem for a spherically symmetric or plane-parallel atmosphere; with PHOENIX/3D we can model 3D atmospheres in Cartesian, cylindrical and spherical coordinate systems, using pre-computed input atmospheres. For both modes, the formal solution of the radiative transfer equation is performed along characteristics.

The core features of PHOENIX/1D are extensively described in Hauschildt (1992, 1993). The high degree of parallelisation in PHOENIX/1D allows us to treat simultaneously a large number of LTE and NLTE transitions with high wavelength resolution (Hauschildt et al., 1997). The code uses the MPI and OpenMP APIs to distribute the work to multiple CPU cores and threads.

An important feature of PHOENIX/1D, currently absent in PHOENIX/3D, is the temperature correction procedure, which ensures iteratively the conservation of the total energy. The temperature correction procedure provides an effective indicator of convergence, associated with the energy and thermal structure of the atmosphere. The convergence rates of electron density, departure coefficients, and the population densities provide additional convergence criteria, in this case related to the NLTE conditions. For PHOENIX/3D models, we only need to rely on the latter quantities to establish the convergence rate.

To compute the Saha-Boltzmann populations for the LTE species, the current version of the code uses the ACES-EOS (Astrophysical Chemical Equilibrium Solver-Equations of State). ACES is based on the VCS method (Villars-Cruise-Smith, Smith and Missen, 1982) to calculate an ideal gas stoichiometric equilibrium, i.e. the calculation of the relative quantities between reactants and

products in a steady state. It takes as input the element abundances, temperature, pressure, and the desired species for which to calculate the concentrations (neutrals, ions, molecules, condensates).

The calculation of opacity and emissivity relies on atomic and molecular spectroscopic databases to read the transitions' quantum mechanical properties. The NLTE atomic lines list is based on the Kurucz<sup>1</sup> database, with the possibility of using the CHIANTI<sup>2</sup> and APED<sup>3</sup> databases as well. The LTE atomic lines list is also based on the Kurucz database, while molecular lines list is based on many different sources, e.g. CO data from Goorvitch (1994), the Kurucz and HITRAN<sup>4</sup> databases etc.

LTE atomic and molecular opacities are computed with a *direct opacity sampling* method: at each iteration, the strongest lines are selected from the line lists and, within a wavelength window, their contributions summed up. This approach allows detailed, depth-dependent line opacity and profile treatment, and it is computationally very efficient thanks to parallelisation.

### 4.1.1 PHOENIX/3D

The three-dimensional mode is a huge advancement for PHOENIX, with an ongoing series of papers dedicated to describe the development progress of the code, with the latest issue being Hauschildt and Baron (2014).

The current version of PHOENIX/3D takes as input pre-computed atmospheres in Cartesian, cylindrical and spherical coordinates. The required data include gas temperature, pressure, and density. These values remain unaltered throughout the simulation.

The iteration scheme in PHOENIX/3D is the following:

- the input atmosphere is given to the code;
- the equations of state are solved for LTE and NLTE species, providing the population densities;
- opacity and emissivity are calculated and the radiative transfer equation is solved for all wavelengths in a prescribed grid;
- the rate equations are solved to get the population densities;
- iterate until old and new population densities converge;
- compute flux spectrum.

The operator splitting scheme (Section 3.4) is used to solve the radiative transfer problem and the multi-level rate equations.

The formal solution of the radiative transfer equation (Eq. 3.11 or 3.47) is performed along characteristics. The *full* characteristics method is currently available. The characteristics, defined by the solid angle  $(\theta, \phi)$ , are tracked continuously through the grid. For each solid angle, each voxel must be hit by, at least, one characteristic. For Cartesian boxes, we can apply periodic boundary conditions on the lateral faces (Hauschildt and Baron, 2008). At the *xy*-boundaries the characteristics are wrapped-around, i.e. they continue on the opposite side of the box, following the periodic boundary conditions. Characteristics with low inclinations would be wrapped-around too many times before reaching the top of the box: therefore, we use a limiting parameter to constrain how many times, per voxel, can a characteristic be wrapped-around. This value is usually set to 16, with lower values poorly resolving the structure, and higher values not improving significantly the results (Seelmann, 2011).

<sup>1</sup><http://kurucz.harvard.edu/>

<sup>2</sup><http://www.chiantidatabase.org/>

<sup>3</sup><http://cxc.harvard.edu/ciao/dictionary/aped.html/>

<sup>4</sup><http://www.cfa.harvard.edu/hitran/>

To calculate the mean intensity or the monochromatic flux, we have to perform an integration of the specific intensity over all solid angles. The integration follows a *pseudo* Monte Carlo procedure (Hauschildt and Baron, 2006). For the mean intensity, we have

$$J_\lambda(\vec{r}, t) = \frac{1}{4\pi} \int_0^{2\pi} \int_0^\pi I_\lambda \sin \theta d\theta d\phi \approx \frac{1}{2\pi^2} \sum_{\theta, \phi} I_\lambda \sin \theta, \quad (4.1)$$

where the sum goes over *pseudo*-randomly selected and equally weighted pairs  $(\theta, \phi)$ . This integration scheme differs insignificantly from a typical quadrature integrative method. The accuracy relies on the angular resolution, i.e. how many different values for the two angles  $\theta$  and  $\phi$ . Usually,  $(n_\theta \times n_\phi) = 48^2$  or  $64^2$  solid angles are sufficient enough to provide accurate solutions (Hauschildt and Baron, 2006).

The parallelisation in PHOENIX/3D is described in Hauschildt and Baron (2010). The domain decomposition distributes the tasks to sets of processes, each with its private memory. The work-load is parallelised over wavelength points and solid angles, given that each formal solution (performed for every wavelength point, for every solid angle) is independent from each other in the rest frame. We define the cluster's size  $s_{cl}$  as the number of processes, collectively working on a single wavelength, each assigned to a different group of solid angles (spatial domain decomposition). We then define the number of clusters  $N_{cl}$ , each assigned to a different set of wavelength points (energy domain decomposition). The hierarchical scheme is based on the MPI framework, which is applicable on practically any machine.

### PHOENIX/3D output

In the current version, the atmosphere data file contains the following data arrays: the input atmosphere thermodynamical quantities  $(T, P, \rho)$ , NLTE levels data  $(n_i, n_i^*, b_i)$ , and species concentrations.

For a spectrum output, which takes the atmosphere data as input and returns the angular averaged radiative field quantities,  $B_\lambda$ ,  $\vec{F}_\lambda$ ,  $J_\lambda$ , and  $S_\lambda$  are stored in a single file per wavelength point.

The specific intensity field can be re-computed using the output spectrum files as input for the imager (introduced in Hauschildt and Baron, 2008). This program generates intensity images of the model for specified solid angles  $(\theta, \phi)$ , using the pre-computed source function to perform a formal solution. I updated the program to deal with the non-regularly spaced vertical axis of the CO<sup>5</sup>BOLD input atmosphere.

## 4.2 CO<sup>5</sup>BOLD

CO<sup>5</sup>BOLD is the abbreviation for ‘‘CONservative COde for the COmputation of COmpressible COnvection in a BOX of L Dimensions with L = 2, 3’’. In-depth description of the code is provided in Freytag et al. (2012), which is the main reference for this section.

CO<sup>5</sup>BOLD solves numerically the time-dependent MHD equations, coupled with radiation transport, on a Cartesian grid. It can be used for two different modelling scenarios: box-in-a-star, and star-in-a-box. The first simulates a small region of a star, using a Cartesian grid, in 2 or 3 dimensions, with equidistant or non-equidistant grid spacing. The star-in-a-box (or global) model also uses a Cartesian grid, with a radial gravitational potential and open boundaries.

The 3D box-in-a-star model used in this work features a non-equidistant grid on the z-axis and equidistant grid on the x- and y-axes. The side-boundaries are treated as periodic. The bottom boundary, located in the convective zone, allows for in- and out-flow of gas. The top boundary is ‘‘transmitting’’, allowing for shocks to leave the box or for gas to flow back in. The gravitational field is vertical and constant. The CO<sup>5</sup>BOLD code also allows for different settings of the boundary conditions.

The code features two different hydrodynamics solvers: a radiation-hydrodynamics mode and a radiation-magneto-hydrodynamics mode. It includes an equation of state to account for the ionisation equilibrium of H, He, H<sub>2</sub> and one representative metal.

Radiative energy gains and losses may constitute an important part in the energy budget of the model. In the deeper layers, where convective motions are strong, the energy is mainly mechanical, and the radiative energy exchanges from cell to cell are local due to the high optical depth. In the outer layers, mechanical and radiative energy exchanges are of similar magnitude, with the latter being non-local due to the lower opacity. Moreover, local variations caused by shocks or waves may produce large fluctuations on the energy source within few cells. Due to the current technological limitations, it is impossible to have a detailed opacity treatment for an already very complex MHD code. CO<sup>5</sup>BOLD relies on the *Opacity Binning method* (Nordlund, 1982). This technique combines continua and lines into several spectral bins, typically from 4 to 12. Only lines and continua that reach optical depth unity within a certain depth range are considered. A further refinement is achieved by splitting the spectral bins into frequency sub-groups, to differentiate between frequency points that preferentially heat or cool the atmospheric layers. The opacity data is usually obtained from tables, like the PHOENIX NextGen opacity tables (Hauschildt et al., 1999). The radiative transfer equation is then solved using short or long characteristics.

### 4.2.1 Simulating MHD flows

Following Freytag et al. (2012), I briefly describe the hydrodynamics problem in absence and presence of magnetic fields, and the difficulties of modelling a stellar atmosphere.

#### Hydrodynamics

The hydrodynamics equations are expressed in terms of the gas density  $\rho$ , the fluid velocity  $\vec{u}$ , the pressure  $P$ , and the total energy density  $\varepsilon$  :

- the *continuity equation*, for the conservation of mass

$$\partial_t \rho + \nabla \cdot (\rho \vec{u}) = 0; \quad (4.2)$$

- the *momentum equation*, for the conservation of momentum, with the additional term due to the (external) gravitational potential  $\Phi$

$$\partial_t (\rho \vec{u}) + \nabla \cdot (\rho \vec{u} \vec{u} + P \mathbf{I}) = -\rho \nabla \Phi, \quad (4.3)$$

where  $\mathbf{I}$  is the identity matrix;

- the energy equation

$$\partial_t (\rho \varepsilon) + \nabla \cdot [(\rho \varepsilon + P) \vec{u}] = -\nabla \cdot \vec{F}, \quad (4.4)$$

where  $\vec{F}$  is the frequency integrated radiative flux;

- the total energy is given by

$$\varepsilon = \varepsilon_{\text{int}} + \frac{u^2}{2} + \Phi, \quad (4.5)$$

where  $\varepsilon_{\text{int}}$  is the internal energy density, calculated with the equation of state;  $\varepsilon_{\text{int}}$  is also used to derive the pressure.

To take *viscosity* into account, a viscous stress tensor must be added in the momentum equation.

The spatial and temporal scales of 3D models are dictated by the physical properties of the atmosphere of interest.

For the Sun (and similarly for M-dwarfs), the model box horizontal size has to be large enough, i.e.  $\sim 10^4$  km, to contain several convective cells to reasonably apply periodic boundary conditions.

The spatial resolution depends on more detailed macroscopic, like the typical sonic velocities, and microscopic properties. The Reynolds number is very helpful in this case. It is defined by  $Re = u_c H_p / \nu$ , where  $u_c$  is the typical velocity of the fluid,  $H_p$  the pressure scale height, and  $\nu$  the microscopic velocity, which takes both atomic and radiative viscosity into account. For the solar atmosphere,  $Re$  reaches large values, around  $10^9 \dots 11$ , therefore the fluid is inviscid and turbulent at very small scales. From simple dimensional arguments, if  $L$  is the size of the convection scale and  $\zeta$  is the size of the smallest turbulent eddy, we obtain that  $Re \sim (L/\zeta)^{4/3}$ : when taking  $L = 10^3$  km, i.e. the typical size of a granule, this translates into turbulence eddy sizes in the order of few centimetres or smaller. It is clearly impossible with the current computing technologies to properly resolve over 10 orders of magnitude in spatial extension. To overcome this inconvenience, an artificial numerical viscosity is introduced which is very large compared to the physical viscosity.

The duration of the simulation should be long enough to make sure that the model has reached a thermally relaxed state. When radiative processes dissipate the thermal energy, the order of magnitude for the thermal relaxation time is given by the Kelvin-Helmholtz time scale  $t_{KH}$ . For the solar surface,  $t_{KH}$  is approximately 300 hours (Freytag et al., 2012), which is very large when compared to the observed typical lifetimes of granules, i.e. few hours. Fortunately, convection carries most of the energy flux. Therefore, a simulation time of few convective turnover times  $t_{turnover} \sim H_p / u_c$ , i.e. few hours, is enough to provide a relaxed state.

The temporal resolution, i.e. the time-step  $\Delta t$ , has to fulfil several criteria. First,  $\Delta t$  has to be shorter than the travel time of the fastest wave possible within a grid cell (*Courant condition*). Second, the time-step should be smaller than the shortest thermal relaxation time possible. From typical solar surface values, it results into  $\Delta t \lesssim 0.1$  s.

### Magneto-hydrodynamics

With few modifications, the magnetic field  $\vec{B}$  can be included in the hydrodynamics equations to derive the *ideal* magnetohydrodynamics equations.

- the *continuity equation* is unaltered;
- the *momentum equation*

$$\partial_t (\rho \vec{u}) + \nabla \cdot \left( \rho \vec{u} \vec{u} + \left( P + \frac{\vec{B} \cdot \vec{B}}{2\mu_0} \right) \mathbf{I} - \vec{B} \vec{B} \right) = -\rho \nabla \Phi, \quad (4.6)$$

with  $\mu_0$  being the magnetic permeability of the vacuum;

- the *energy equation*

$$\partial_t (\rho \varepsilon) + \nabla \cdot \left[ \left( \rho \varepsilon + P + \frac{\vec{B} \cdot \vec{B}}{2\mu_0} \right) \vec{u} + \vec{B} (\vec{u} \cdot \vec{B}) \right] = -\nabla \cdot \vec{F}; \quad (4.7)$$

- *Faraday's law*

$$\partial_t \vec{B} + \nabla \cdot (\vec{u} \vec{B} - \vec{B} \vec{u}) = 0; \quad (4.8)$$

- the total energy density becomes

$$\varepsilon = \varepsilon_{\text{int}} + \frac{u^2}{2} + \frac{B^2}{2} + \Phi; \quad (4.9)$$

- the magnetic field is constrained by  $\nabla \cdot \vec{B} = 0$ .

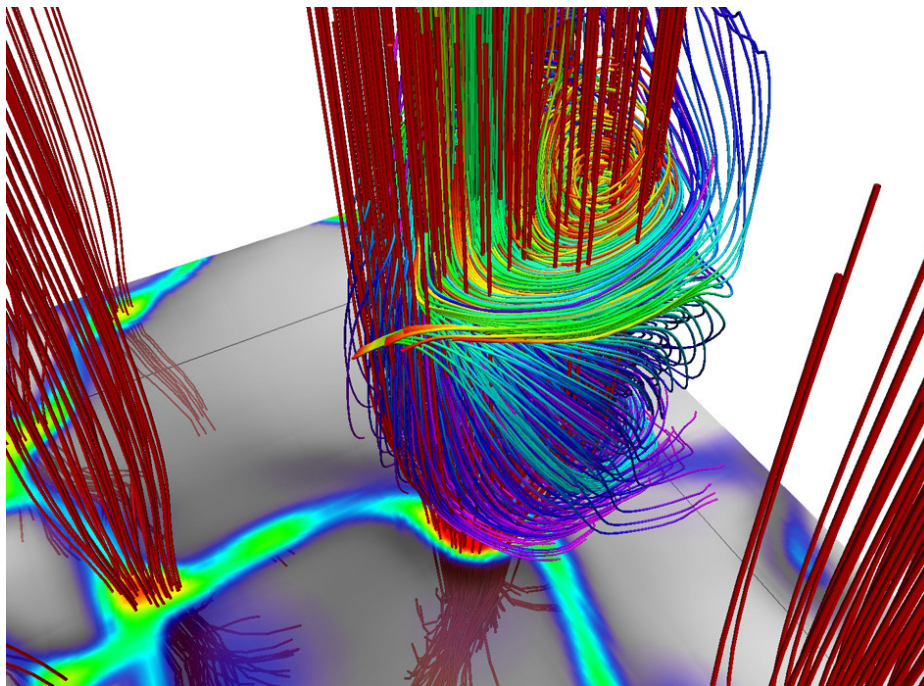


Figure 4.1: From Wedemeyer et al. (2013). A “magnetic tornado” in one of the models from the M-dwarf models CO<sup>5</sup>BOLD grid. The coloured surface represents the strength of the magnetic field at the bottom of the photosphere. The magnetic field (red lines) is concentrated in the intergranular lanes and funnels out into the chromosphere. The gas (green-blue lines) is frozen on the magnetic field lines and, therefore, moves following spiral trajectories.

Although this step is formally simple, the numerical implementation is not straightforward. Especially the magnetic field divergence-free constrain throughout the box requires special attention. Another problem is related to the positivity of the gas pressure, a quantity derived from the total energy equation. If the magnetic and kinetic energy terms are much larger than the pressure term, small discretisation errors may produce a negative value of the pressure. This problem is only marginal in the photosphere, where the plasma- $\beta$ , i.e. the ratio of thermal over magnetic pressure, is very high, but becomes relevant in the chromosphere, which is the region where the plasma- $\beta$  goes below 1.

The spatial and temporal resolutions have to be increased when including magnetic fields, necessary when simulating the chromosphere. The magnetic field usually forms very localised magnetic flux regions, requiring, therefore, higher spatial accuracy. Moreover, low density and strong magnetic field environments, i.e. low plasma- $\beta$ , feature typical Alfvén velocities,  $u_A \sim \sqrt{B^2/\rho}$ , larger than the speed of sound,  $u_s \sim \sqrt{P/\rho}$ . With a magnetic field strength of the order 1 kG, typical for sunspots, and temperature minimum gas pressure of the order 100 dyne cm<sup>-2</sup>, the ratio between hydrodynamic and magneto-hydrodynamic time-steps is of the order 100, i.e. few milliseconds. Comparing this time-step with the above mentioned relaxation time for a convective solar model, i.e. hours, clearly shows the computational time cost of these simulations.

#### 4.2.2 M-dwarf models grid

Wende et al. (2009) used CO<sup>5</sup>BOLD for modelling M-dwarfs atmospheres. They computed hydrodynamic photospheric models (no magnetic fields or chromosphere included) to investigate the effective temperature and surface gravity dependence of the velocity fields. Wedemeyer et al. (2013) expanded the same working set-up by extending the model in depth and height to include the chromosphere, increasing the spatial resolution, and adding magnetic fields.

The M-dwarf chromosphere models grid, described in Wedemeyer et al. (2013), was built adopting as initial model a snapshot from a photosphere calculation with  $T_{\text{eff}} = 3330$  K and  $\log g = 4.5$ , similar to the models discussed in Wende et al. (2009). These stellar parameters are analogous to AD Leo. The box final extension is  $1950 \times 1950 \times 1692$  km with  $120 \times 120 \times 261$  cells. The z-axis ranges from -713 to 979 km, with  $z = 0$  km defined as the surface with average Rosseland mean opacity (the average opacity weighted over the derivative of the Planck curve) equal to 1, corresponding to the bottom of the photosphere. This model, so far purely hydrodynamic, was then used as input for the MHD runs. The initial magnetic field was added following two different configurations: a uniform vertical field and a  $2 \times 2$  checker-board vertical field with mixed polarities. For both initial magnetic field configurations, five different values were chosen for the magnetic field strength at the beginning of the simulation:  $|B_z|_0 = 10$  G, 50 G, 100 G, 200 G, and 500 G. In addition, a purely hydrodynamic model was also computed. In total, 11 atmospheres were computed, for 1800 s (physical time) to guarantee the relaxation of the models.

The atmosphere in these simulations present a high level of variability, concerning the structure of the magnetic field lines and the evolution of the shock fronts, which heat up the gas locally while the post-shocked gas cools to low temperature. Magnetic tornadoes, similar to those on the Sun, also develop in these simulations, suggesting that they may play an important role for the heating of the outer atmosphere also in late-type dwarfs (Fig. 4.1).

For each of the models in the grid, Sven Wedemeyer kindly provided us six snapshots at different time-steps.

## 4.3 Setup for this project

### 4.3.1 CO<sup>5</sup>BOLD input model

At the time of writing, PHOENIX/3D models using only one of the provided snapshots were finalised, characterised by initial uniform magnetic field and  $|B_z|_0 = 10$  G, i.e. a low activity model. This snapshot has been extensively used to test the code and also to finally produce a physically meaningful atmosphere. My analysis of these calculations constitutes the main part of my project.

Several physical quantities are saved into a CO<sup>5</sup>BOLD time-step file: physical extension, gas temperature and density, velocity and magnetic field components. The other physical quantities, such as optical depth, entropy, etc., can be re-computed *a posteriori* from the model snapshot. For PHOENIX/3D simulations, we consider only temperature, pressure and density.

Vertical profiles of these variables are displayed in Figs. 4.2. The information is extracted column by column (each column with a different colour), with black lines representing the average per vertical layer. The temperature profile shows a steep decline from the deepest layers up to  $z \sim 200$  km, with small variations column by column. For layers above  $z \sim 200$  km, the temperature may strongly vary from cell to cell, where shock fronts are present. Pressure and density show a similar structure, with both quantities varying over 2-3 orders of magnitude in the chromospheric layers.

Colour maps of the temperature are displayed in Fig. 4.3. A vertical slice through the box (Fig. 4.3a) reveals how the temperature decreases, on average, from the photosphere up to the chromosphere. Hot gas regions, corresponding to shocks and filaments, are visible in the upper layers, with peak temperatures up to  $\approx 6000$  K. The horizontal map at  $z = 0$  km (Fig. 4.3b) shows the photospheric granulation pattern. Going upwards (Fig. 4.3c), the gas is cool,  $T \approx 2000$  K, but very hot patches are present. At the outermost layers (Fig. 4.3d), the cool and hot gas occupy similarly large volumes. However, for the whole chromosphere, cool gas takes the largest fraction of the volume. We can verify this by displaying a histogram of the temperature for layers above  $z = 0$  km (Fig. 4.4, gray histogram). Most of the cells are characterised by a temperature between 2000 and 3000 K, with the histogram extending up to 6000 K but with very few cells featuring such high temperatures. The red, green, and blue histograms in Fig. 4.4 show the temperature distribution for

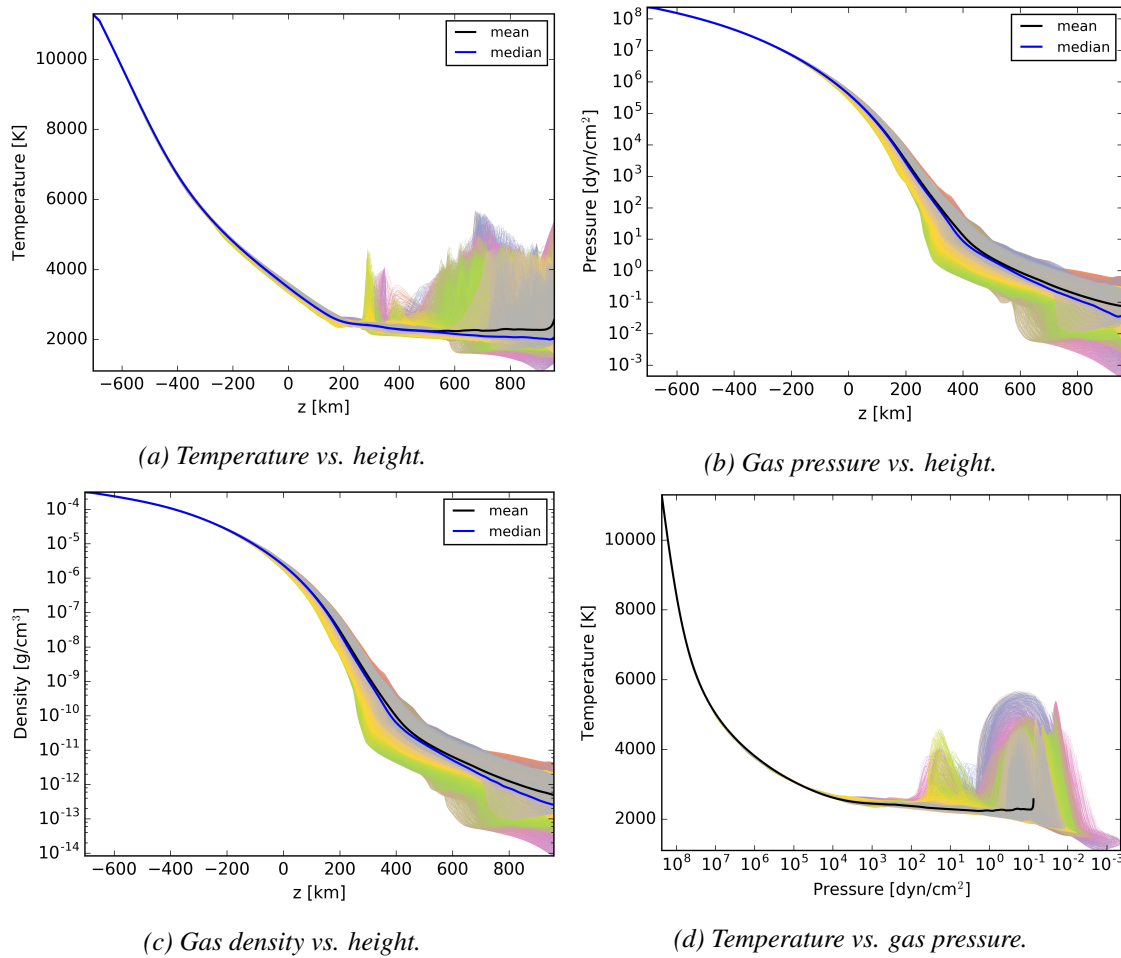


Figure 4.2: Thermodynamic quantities from the original CO<sup>5</sup>BOLD model, extracted column by column, each column with a different colour. The black and blue lines in each plot represent the horizontal average and median for the corresponding quantity.

different height ranges: with increasing altitude, the “warmer” bins become relatively more populated, but most of the cells are characterised by progressively lower temperature. The histogram also reveals the absence of a temperature bifurcation, which is an observed feature in the solar CO<sup>5</sup>BOLD models (Wedemeyer et al., 2004).

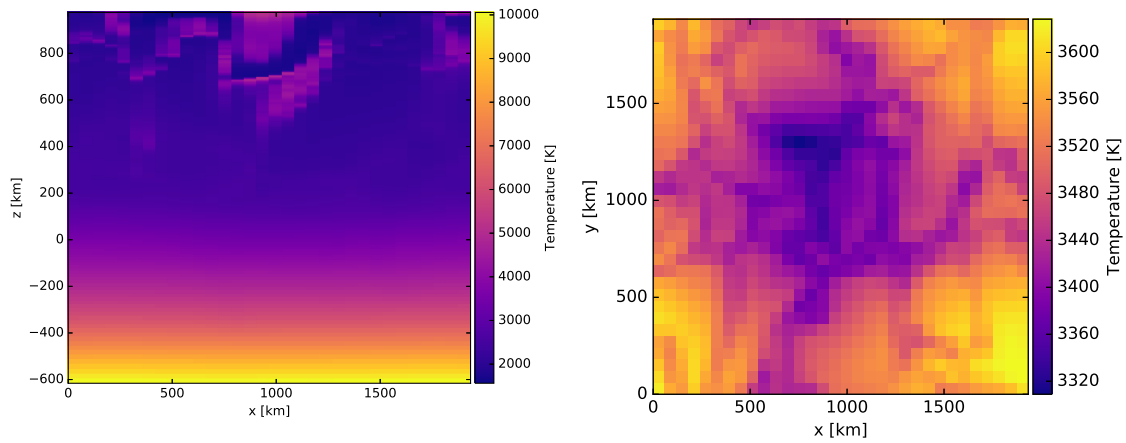
The temperature structure of the adopted CO<sup>5</sup>BOLD snapshot shows the signature of the slow, large scale oscillations in the MHD model. The temperature map for the height  $z = 0$  km, corresponding to the surface with the average Rosseland mean opacity  $\tau_R$  equal to 1, is displayed in Fig. 4.5a. Slow modes, due to the oscillations triggered by convection, make the model “breathe”: temperature, pressure, etc., vary in response to these oscillations, and the deeper layers expand and contract on long time scales (this effect is stronger at the bottom of the model where the density is higher). As a result, at a specific time-step, the optically depth unity surface is deformed, like a membrane. At the height with *average* Rosseland mean opacity equal to 1, the temperature map may show very high contrast between the centre of the models and the boundaries. From the original CO<sup>5</sup>BOLD data, we can interpolate the temperature data with the optical depth scale to obtain the surface with  $\tau_R$  equal to 1 (Fig. 4.5b), for which the contrast is decreased. Global oscillations are well reproduced in solar simulations (Wedemeyer et al., 2004) and under investigation for the M-dwarf models (Wedemeyer, private communication). For the purpose of the PHOENIX/3D simulations presented in this work, these temperature oscillations do not critically affect the calculations: the opacity is calculated self-consistently, and the 3D treatment takes care of computing the radiative field throughout the structure, weighting the contribution from all solid angles. Moreover, the oscillations influence mostly the photospheric layers.

### 4.3.2 PHOENIX/3D runs

Three PHOENIX/3D runs with the same input model and different settings were computed.

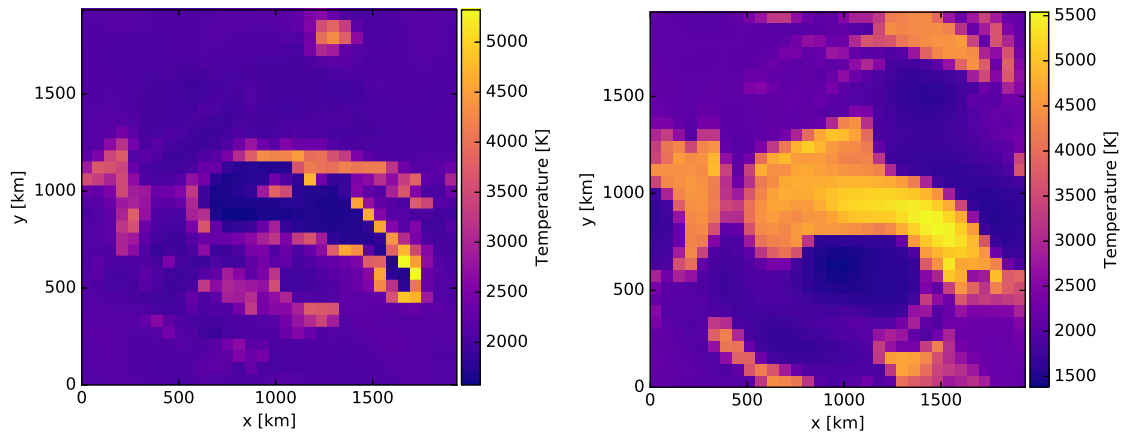
- NN - a spatially binned model,  $33 \times 33 \times 257$ , with full NLTE treatment for the following species: H and He with ionisation state I, and C, N, O, Mg, and Ca with ionisation states I and II; the total number of NLTE levels is 1632, corresponding to 18580 transitions, with a wavelength grid of  $\sim 180000$  points; no atomic or molecular background LTE opacity;
- NL - same as NN, with LTE atomic and molecular background lines;
- NS - a spatially non-binned model,  $120 \times 120 \times 257$ , with fewer NLTE species (H I, Mg I-II, Ca I-II) small model atoms; 133 NLTE levels (238 transitions) and a wavelength grid of  $\sim 4000$  points.

The angular resolution for all models is  $(n_\theta \times n_\phi) = 48^2$ . Chemical abundances were set to solar values, following Asplund et al. (2009). The uppermost layers in the CO<sup>5</sup>BOLD models may be affected by the top boundary condition. For instance, some of the provided snapshots present single isolated cells with extremely high temperature values within the uppermost layers, e.g.  $T \sim 10^5$  K or higher. Therefore, the last four layers of the input model box were removed.



(a) A slice showing the vertical profile of the temperature.

(b) Temperature at  $z = 0$  km.



(c) Temperature at  $z \sim +600$  km.

(d) Temperature at the outermost layer.

Figure 4.3: The temperature structure in the input model used for the PHOENIX/3D runs with binned resolution. The original CO<sup>5</sup>BOLD model has a grid resolution four times higher.

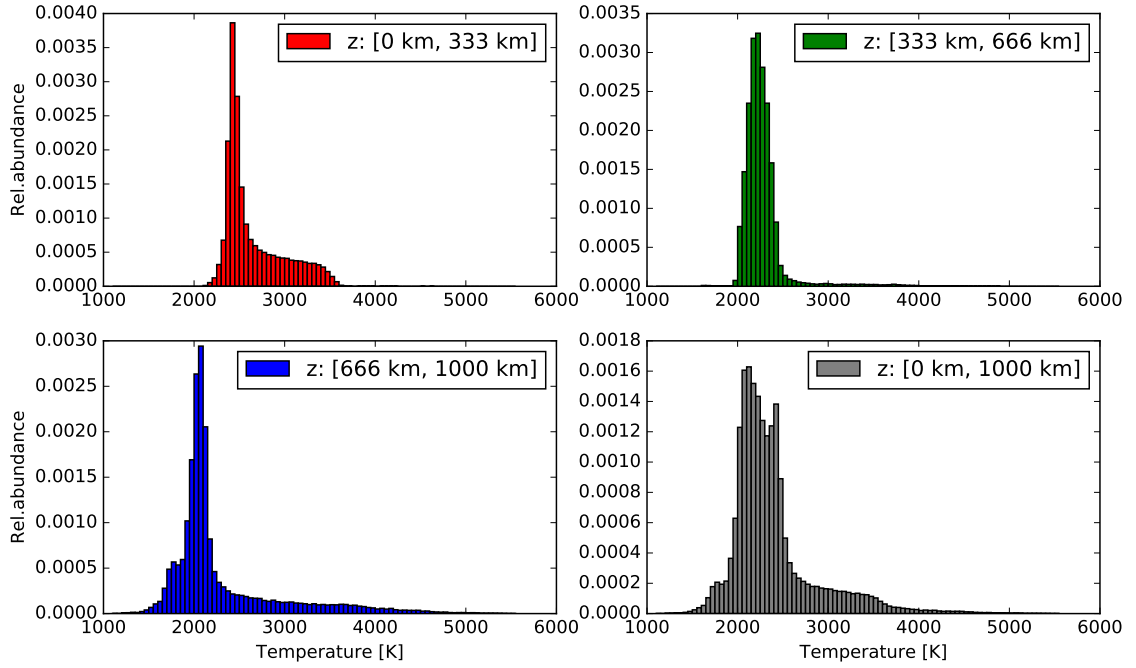
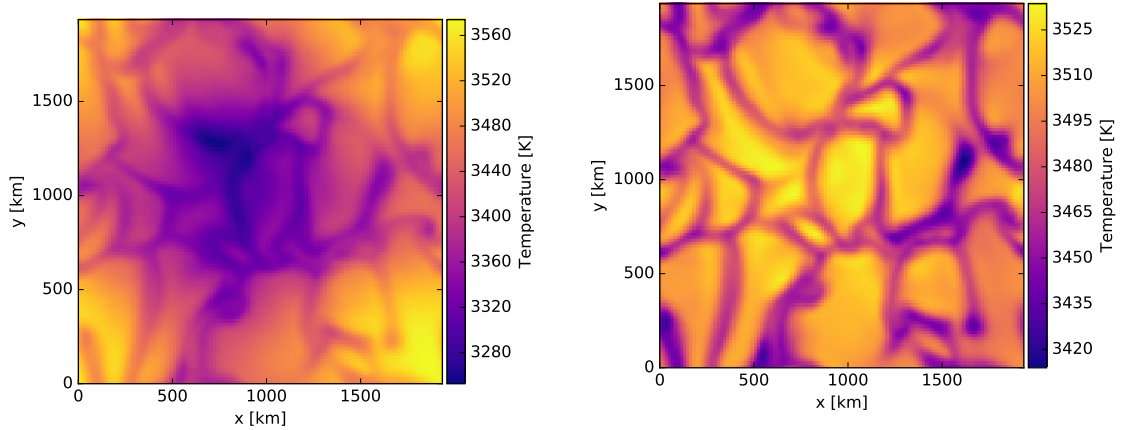


Figure 4.4: Temperature histograms for the input model. Only cells located above  $z = 0$  km, i.e. upper photosphere and chromosphere, were considered. The temperature bins are 50 K wide. The red, green, and blue histograms show three different height ranges, while the gray histogram shows the full temperature distribution for  $z > 0$  km.



(a) Temperature map at  $z = 0$  km, i.e. the layer with  $\langle \tau_R \rangle = 1$ .

(b) Temperature map at the  $\tau_R = 1$  surface, obtained after interpolating the temperature structure to the optical depth scale column by column.

Figure 4.5: Temperature maps at height with Rosseland mean opacity  $\tau_R$  equal to 1 (from the original CO<sup>5</sup>BOLD snapshot used as input model for PHOENIX/3D).



# Chapter 5

## Results

In this chapter, I show the results from the different models computed. Models NN (only NLTE opacity) and NS (small model atoms) are described only briefly, given their role as test cases, and I focus the description on the “more realistic” NL model (NLTE and LTE opacity). The data presented here is discussed in Chapter 6.

### 5.1 NLTE only opacities (NN model)

The atmosphere given to PHOENIX/3D for this case is a binned version of the original CO<sup>5</sup>BOLD model grid, with  $33 \times 33 \times 257$  voxels.

This model was a (successful) test for the 3D NLTE multi-level rate operator (Hauschildt and Baron, 2014) with a complex input atmosphere, periodic boundary conditions and non-regularly spaced z-axis. It also served as a starting point for a more realistic run including LTE opacities.

The wavelength grid goes from 10 Å to 0.1 mm, with variable resolution throughout the grid:  $\Delta\lambda = 1$  Å up to  $\lambda = 2000$  Å,  $\Delta\lambda = 2$  Å up to  $\lambda = 20\,000$  Å etc. Each NLTE line transition is treated with higher wavelength resolution, namely 11 wavelength points, i.e. the rest wavelength and 5 points on both wings.

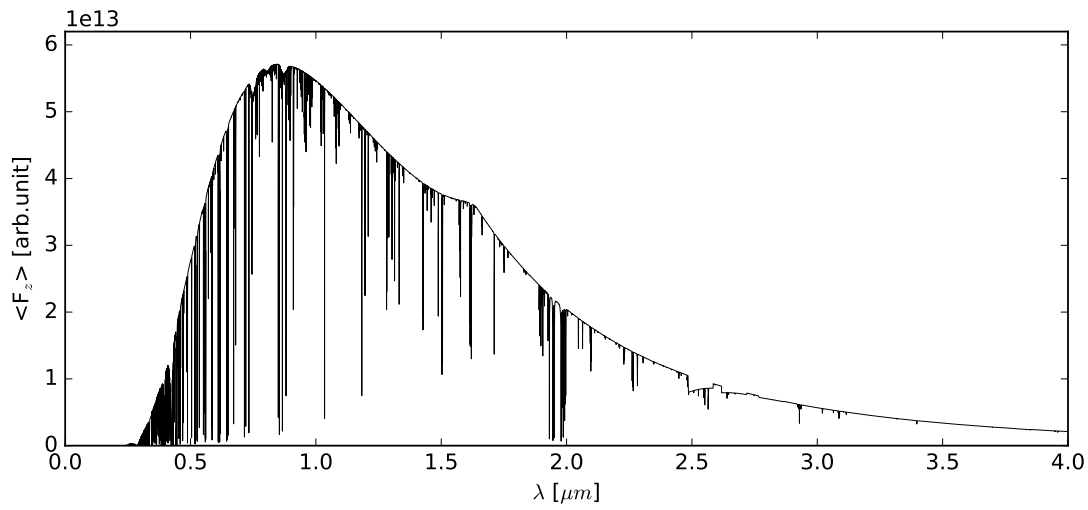
#### Spectrum

The vertical (outgoing) component of the radiative flux  $F_{z,\lambda}$ , although not being a physical observable quantity, can be used to create a synthetic spectrum of the model. Specifically, the flux spectrum is computed as the average of  $F_{z,\lambda}$  across the outermost layer.

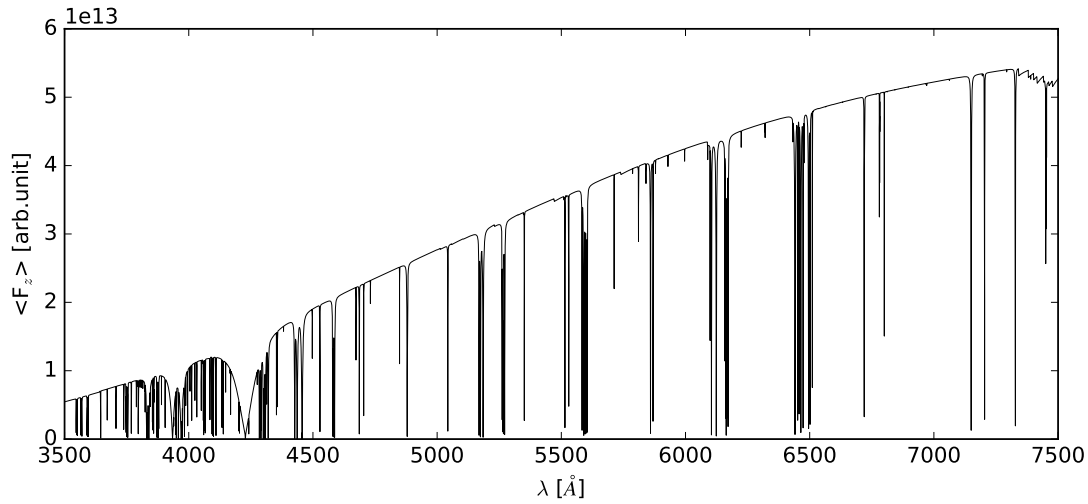
The spectrum (Fig. 5.1a) for model NN is clearly dominated by the continuum. The flux peak is located in the near infrared, at approximately 0.9  $\mu\text{m}$ , with a secondary bump at 1.6  $\mu\text{m}$  corresponding to the H<sup>-</sup> opacity minimum. Absorption lines from atomic species are present throughout the optical (Fig. 5.1b) and infrared. At shorter wavelengths (Fig. 5.1c), the flux is strongly reduced (at Lyman- $\alpha$ , the continuum is 10 orders of magnitude weaker than in the optical), and the spectrum is characterised by many absorption and few emission features. The lines are only originating from the atomic species included for the NLTE multi-level treatment. Lacking LTE atomic and, especially, molecular opacities, the flux spectrum does not resemble a typical M-dwarf spectrum. This is unsurprising, because molecules represent the largest opacity contributions in M-dwarf atmospheres.

### 5.2 NLTE and LTE opacities (NL model)

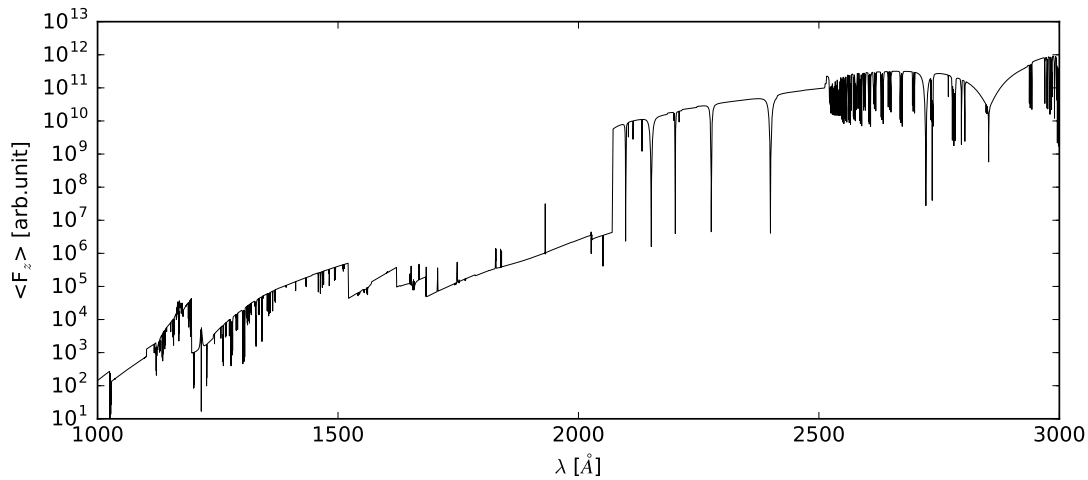
Model NL was computed using the same input atmosphere and continuum wavelength grid adopted for model NN. LTE atomic and molecular opacities were added. This model is the main subject of



(a) Optical and infrared range. The second peak at  $\approx 1.6 \mu\text{m}$  corresponds to the  $\text{H}^-$  opacity minimum bump. The lines in the spectrum originate only from the NLTE atomic species included.



(b) Optical range.



(c) UV range (flux scale is logarithmic).

Figure 5.1: Model NN (NLTE opacity): spectrum computed from the horizontally averaged vertical (outgoing) component of the radiative flux at the outermost layer of the model.

the discussion in the next chapter.

## Spectrum

The effect of “activating” LTE opacity is clearly visible in the overall spectrum (Fig. 5.2a), with the continuum being strongly affected by millions of atomic and molecular lines. Focusing on the optical wavelengths (Fig. 5.2b), the strong molecular bands, typical of M-dwarfs spectra, are visible. The optical and infrared intervals are characterised by a pure absorption spectrum, with “apparent” emission lines being only optically thin windows between absorptions. This effect is clear when looking close to the Ca II H&K doublet (Fig. 5.2c). The UV spectrum (Fig. 5.2d) displays a weak continuum and a forest of emission and absorption lines. Few lines, like Lyman- $\alpha$  (Fig. 5.2e), the Mg II h&k doublet, etc., display an absorption core within an emission profile.

The physical origin and interpretation of these features are discussed in Section 6.1.

## Flux maps

The vertical flux  $F_{z,\lambda}$  (Eq. 3.7), although not being a physical observable, can be used to create simplified synthetic images of the surface at different wavelengths (Figs. 5.3). For each wavelength point, the patterns visible in the flux map are connected to the formation height of spectral continua and lines (more details in Section 6.2).

At short wavelengths, the surface appears very differently when looking in the continuum, e.g. 1200 Å in Fig. 5.3a, or in line cores, e.g. the Mg II h in Fig. 5.3b. The UV continuum flux traces the hot regions, connected to shock waves, distributed through the whole chromosphere, with the contrast<sup>1</sup> between dark and bright regions being very high. For the Mg II h line core, an optically thick line, the flux map features resemble the temperature structure of the upper layers (see Fig. 4.3d), with the flux peaking in a region with low temperature.

The appearance of optical maps for wavelength points corresponding to molecular bands, e.g. the TiO band at 6320 Å in Fig. 5.3c, resembles the granulation pattern at photospheric layers, as seen in Fig. 4.3b. Absorption lines flux maps at longer wavelengths, e.g. the Ca II 8544 Å in Fig. 5.3d, also display features that resemble the gas temperature at chromospheric heights, but deeper than, for example, the Mg II h line core, due to the lower opacity of the line. For optical wavelengths, the root mean square (rms) values for the vertical flux contrast range from 1 to 3% and decrease with increasing wavelength, as observed for the Sun (Wedemeyer-Böhm and Rouppe van der Voort, 2009a). Compared to solar observations, these values are much smaller, i.e. factor  $\sim 10$ : this is due to the lower temperature contrasts in the M-dwarf photosphere compared to the Sun (Ludwig et al., 2002; Wedemeyer and Ludwig, 2015).

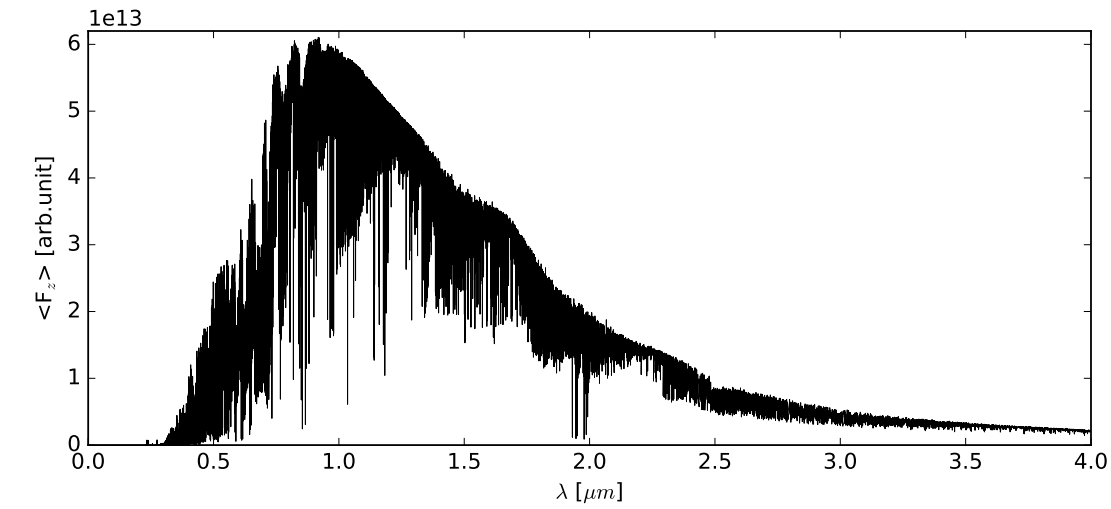
The infrared and far infrared continua, e.g. 10  $\mu\text{m}$  and 0.1 mm in Figs. 5.3e and 5.3f, also show the granulation pattern. At these wavelengths, the flux contrast between lanes and granular regions is very shallow, with rms values ranging from 0.5 to 0.1%.

## Intensity images

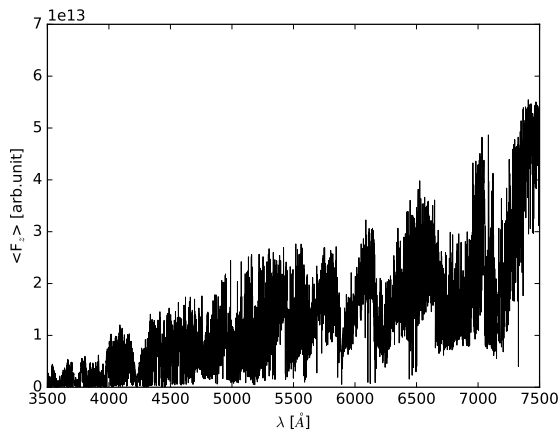
For specific wavelengths, we can compute intensity images of the model’s outermost layer for different viewing angles  $\theta$  (or, conversely,  $\mu = \cos \theta$ ).

In the UV continuum ( $\lambda = 1800$  Å, Fig. 5.4), the images present bright spots with generally large contrast. For  $\mu \sim 1$ , the rms values of the intensity contrast take values between 90 and 100%. When viewing close to the limb, i.e.  $\mu \sim 0$ , the intensity images present limb brightening, with rms contrast ranging from 100 to 700% for different azimuthal angle  $\phi$ . This suggests that the features are located somewhere close to the top boundary of the model (more details in Section 6.2).

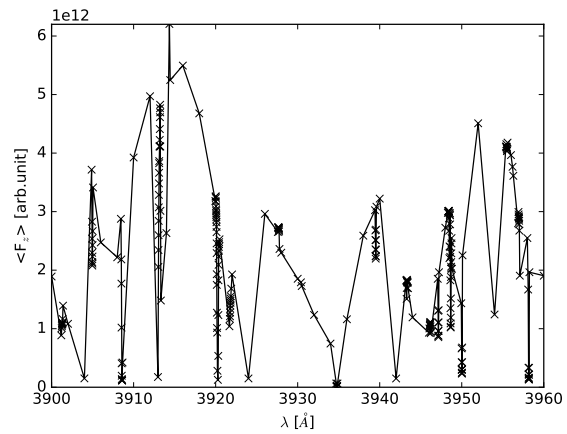
<sup>1</sup>For the wavelength  $\lambda$ , the contrast  $C$  for the quantity  $f_\lambda$ , e.g. intensity or vertical flux for these models, is computed as  $C = f_\lambda / \langle f_\lambda \rangle - 1$ , with  $\langle f_\lambda \rangle$  being the mean across the xy-plane.



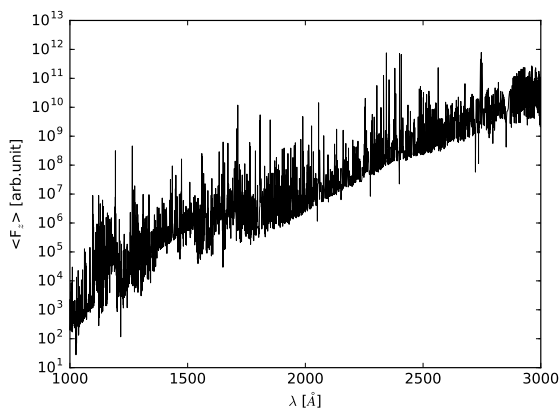
(a) Optical and infrared range.



(b) Optical range.



(c) Ca II H&amp;K doublet.



(d) UV range (flux scale is logarithmic).

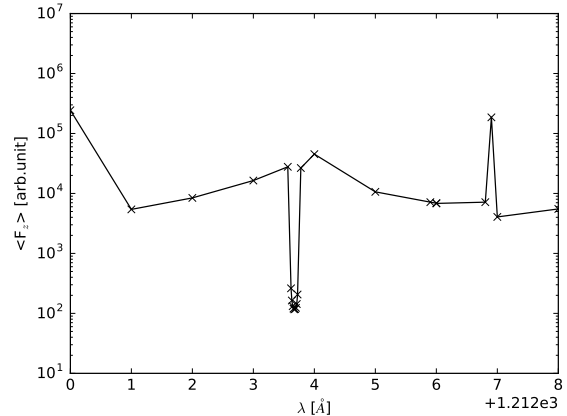
(e) Lyman- $\alpha$  (flux scale is logarithmic).

Figure 5.2: Model NL (NLTE+LTE opacity): flux spectrum, computed like in Figs. 5.1. Compared to model NN, i.e. only NLTE opacity, this spectrum shows the molecular absorption bands typical in M-dwarf optical and infrared spectra.

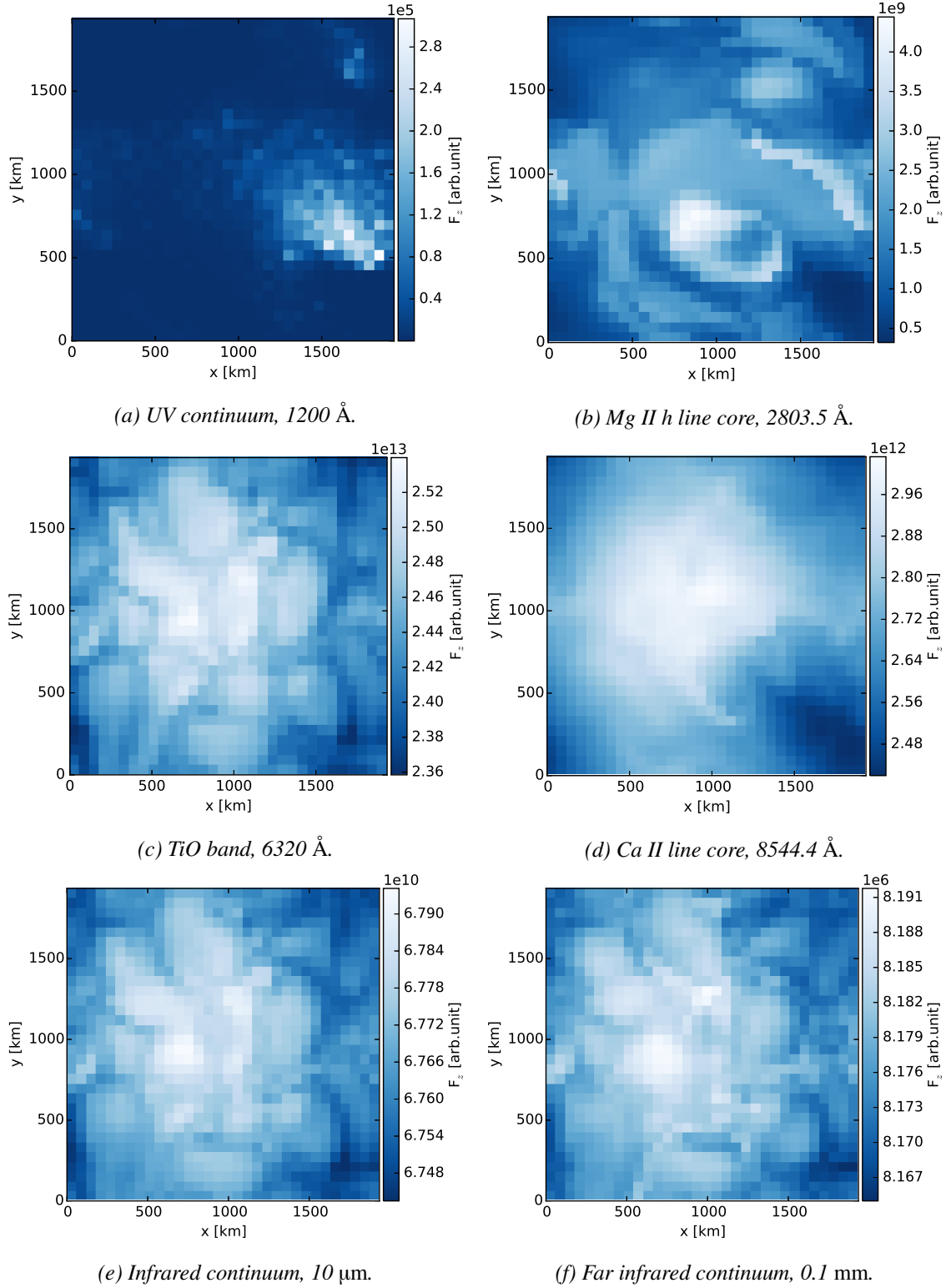


Figure 5.3: Model NL: vertical flux colour maps. The colour-coded flux corresponds to the vertical component of the radiative flux at the outermost layer of the model.

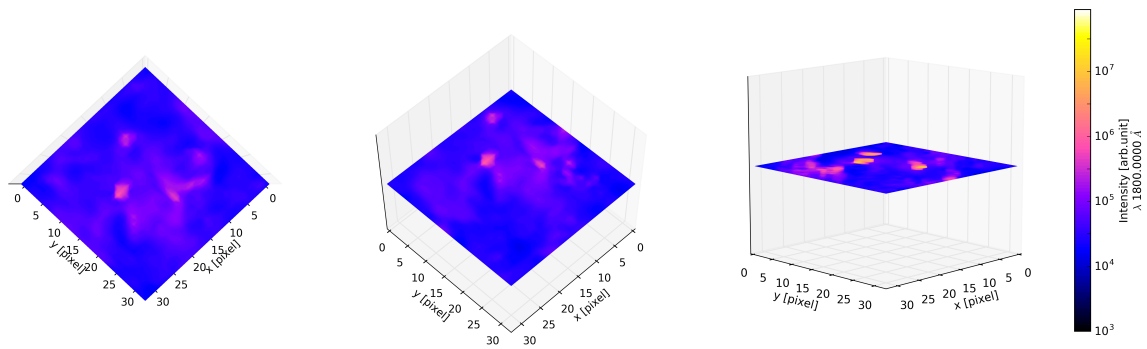


Figure 5.4: Model NL: intensity images for the outermost layer at  $\lambda = 1800 \text{ \AA}$ , i.e. UV continuum. The colour intensity minimum and maximum values (displayed on the right bar) are set to the lowest and highest intensities at all angles.

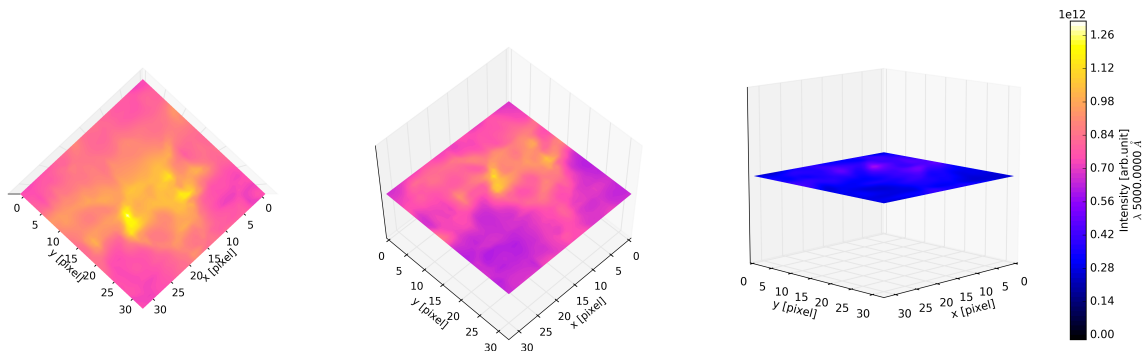


Figure 5.5: Model NL: intensity images, like in Fig. 5.4, for  $\lambda = 5000 \text{ \AA}$ , i.e. optical continuum.

In the optical continuum ( $\lambda = 5000 \text{ \AA}$ , Fig. 5.5), for  $\mu \sim 1$ , the model shows a less pronounced contrast, i.e. few percent, when compared to the UV pictures. At smaller  $\mu$ 's, the effect of the limb-darkening is visible.

At infrared wavelengths ( $\lambda = 10 \text{ \mu m}$ , Fig. 5.6), the images for low inclinations show an almost uniform surface with a very low contrast ( $\sim 0.5\%$ ), featuring the granulation pattern visible in the vertical flux maps; the off-limb images present a weaker limb-darkening when compared to shorter wavelengths images.

### Species concentrations

The EOS provides concentrations for the atomic and molecular species included in the simulation. 894 species are considered in total, including neutral and ionised atoms and molecules.

Figs. 5.7 show the concentrations for a selection of species through a vertical slice in the model (the temperature map in Fig. 4.3a shows the same slice). It is clear how the concentration maps follow the temperature profile within the atmosphere. For neutral hydrogen, protons, and negative hydrogen (Figs. 5.7a, 5.7b, and 5.7c, respectively), concentrations are high in the photosphere and decrease through the cool chromosphere, where most of the hydrogen is trapped into  $\text{H}_2$  (Fig. 5.7a). However, in the presence of warm chromospheric gas, molecules, e.g.  $\text{H}_2$ , CO (Fig. 5.7e), and TiO (Fig. 5.7f), dissociate and their concentrations are lower. Moreover, it is important to note that the NLTE treatment influences the concentrations of the atomic species included in the multi-level NLTE calculations (H, He I; C, N, O, Mg, Ca I-II) and, consequently, the concentrations of ions and molecules containing them (more details in Section 6.5).

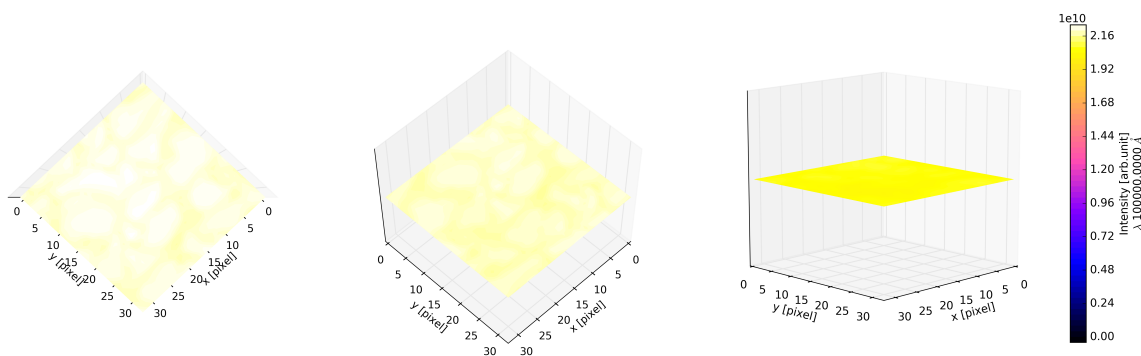


Figure 5.6: Model NL: intensity images, like in Fig. 5.4, for  $\lambda = 10 \mu\text{m}$ , i.e. infrared continuum.

### Departure coefficients

The departure coefficients  $b_i$  for the ground states of a selection of species (H I, He I, and Ca II) are plotted in Figs. 5.8.

The frames on the left side represent the  $b_i$ 's through the same vertical slice mentioned above, Fig. 4.3a. For all the species, LTE conditions are valid through the photosphere, i.e.  $z \lesssim 200 \text{ km}$ . In the chromosphere, the  $b_i$ 's take high values, i.e. above unity, in correspondence of warm gas, and very low values, i.e. less than 1, where the gas reaches the lowest temperatures. The frames on the right side in Figs. 5.8 display the departure coefficients at the outermost layer. The correspondence between the  $b_i$ 's values and the local temperature is clear once we compare these frames with the temperature map for the outermost layer (Fig. 4.3d). A comparison between the LTE population densities  $n_i^*$  and the actual population densities  $n_i$  (Figs. 5.9) shows even more explicitly this agreement.

As mentioned above, the LTE and actual population densities take very similar values in the photosphere. In the chromosphere, the LTE population densities follow the local temperature profile. Hydrogen is trapped into molecules in the presence of cool gas, or ionised where the temperature is high: in both cases, the LTE population density is decreased. For He I and Ca II, the ground states are more populated for lower temperatures, in agreement with the Saha-Boltzmann distribution. The actual NLTE population densities follow a different behaviour, with over-population, compared to LTE, where the gas is warm, and under-population where the temperature is low. These plots clearly highlight the importance of NLTE treatment for the chromosphere, where the real population densities differ by orders of magnitude from the LTE case. Ignoring this fact would lead to inaccurate calculation of the radiative properties and, ultimately, wrong estimate of the spectral diagnostics.

The influence of the complex inhomogeneous thermal structure on the radiative properties and the relation between departure coefficients and local temperatures are discussed in Chapter 6.

### 5.3 Small model atoms (NS model)

The input atmosphere for this model is the original CO<sup>5</sup>BOLD model snapshot, i.e.  $121 \times 121 \times 257$  voxels, with approximately  $4 \times 4$  higher horizontal resolution than models NN and NL. This run served as a test to evaluate the performance of PHOENIX/3D with higher spatial resolution, therefore, more memory-demanding, and with a reduced list of NLTE species and transitions.

The finer spatial grid for this model makes it almost impossible to adopt a large, highly resolved wavelength grid or to include a large number of NLTE transitions, due to technical restrictions (more details in Chapter 6). For this purpose, the continuum wavelength grid resolution was decreased. The species treated in NLTE consist only of H I, Ca I-II, and Mg I-II. The number of levels per NLTE species was reduced, i.e. 133 levels with 238 transitions in total, compared to the 1632 levels and

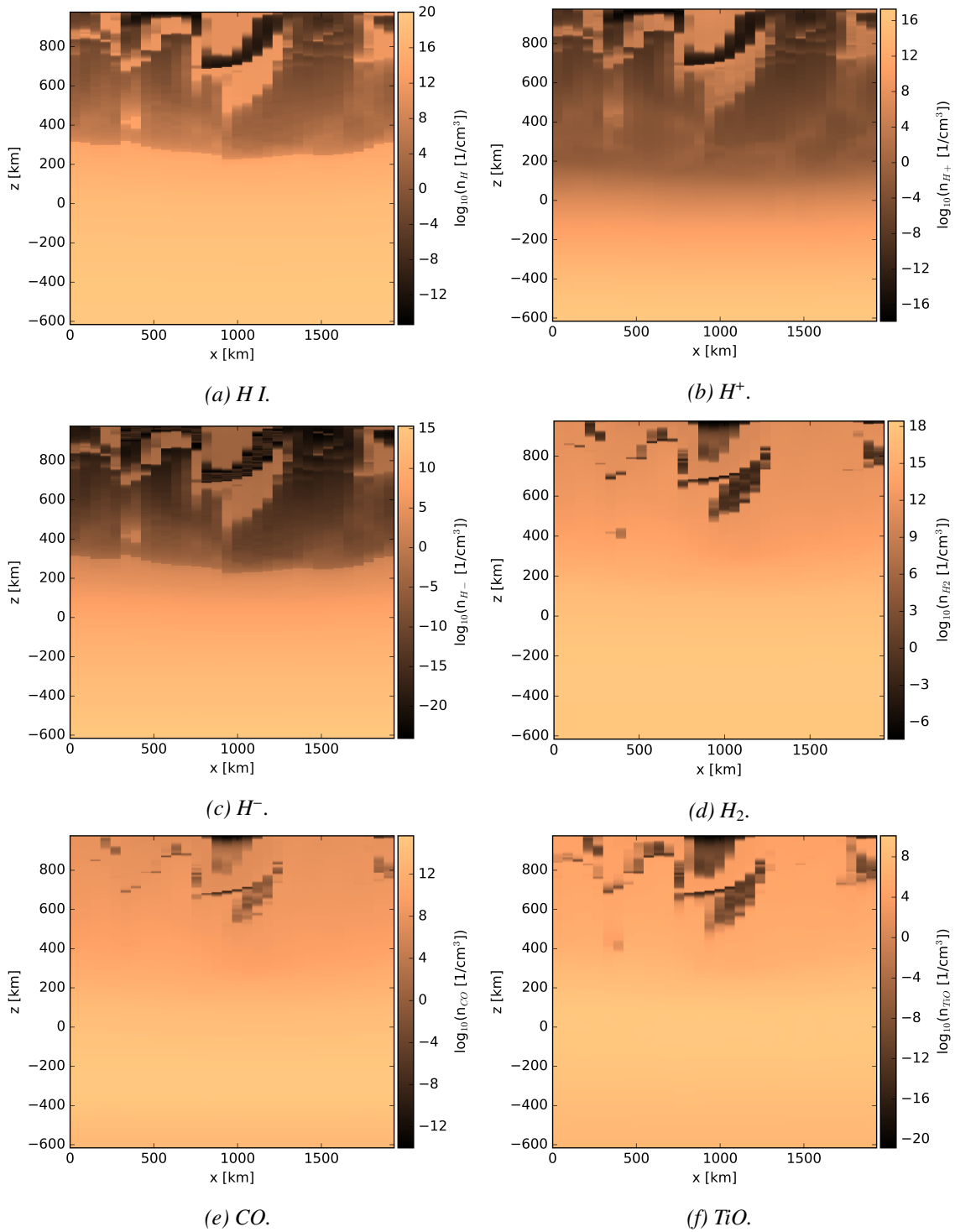


Figure 5.7: Model NL: concentrations colour maps for a selection of species. The vertical slice is the same used in Fig. 4.3a.

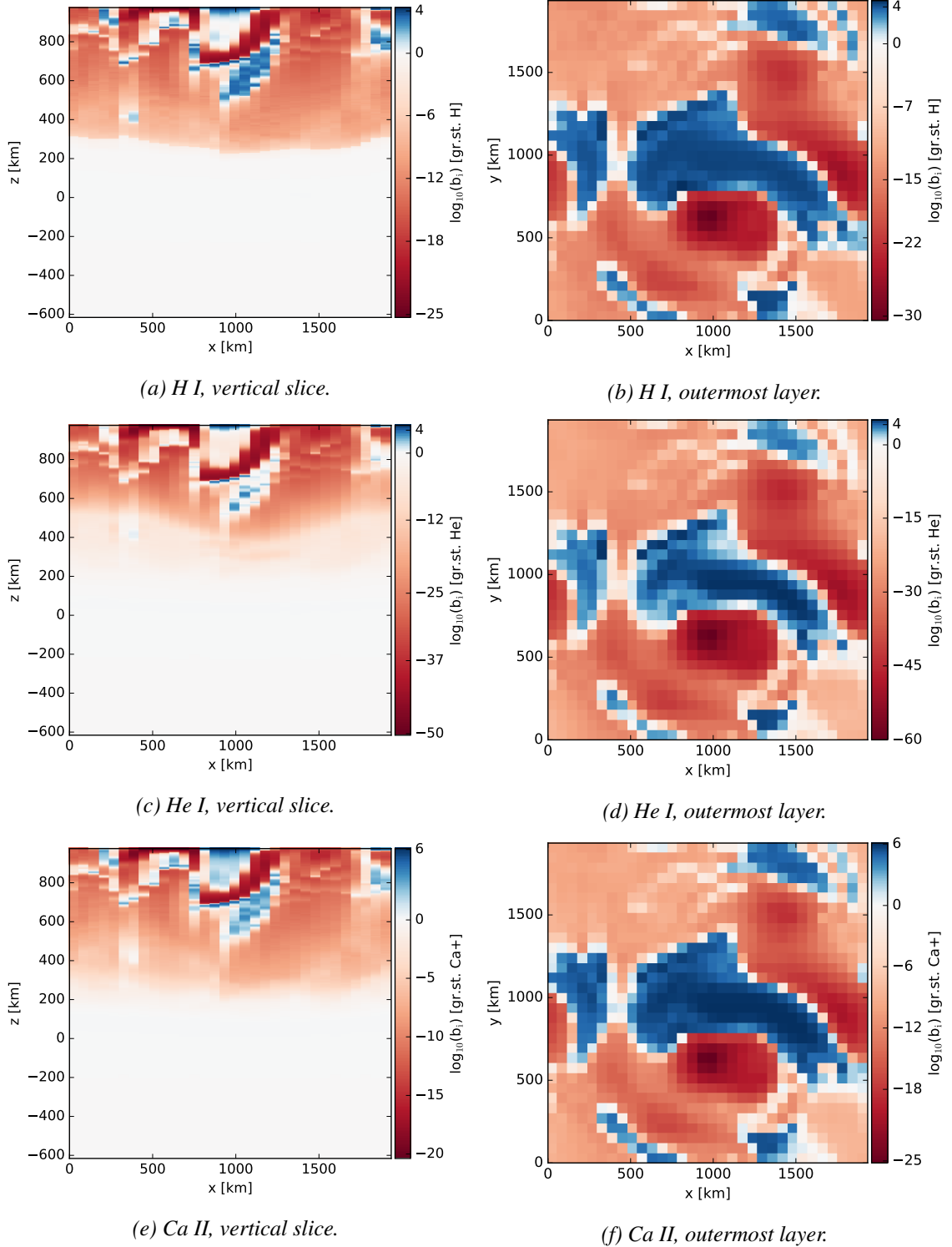


Figure 5.8: Model NL: departure coefficients for the ground state of different ions (the colour bar is logarithmic). The area in white takes values  $b_i \sim 1$ , while red and blue indicates respectively under- and over-population with respect to the LTE values. The left panels show the same vertical slice adopted for Fig. 4.3a and Figs. 5.7, while the right panels show the outermost layer, like in Fig. 4.3d.

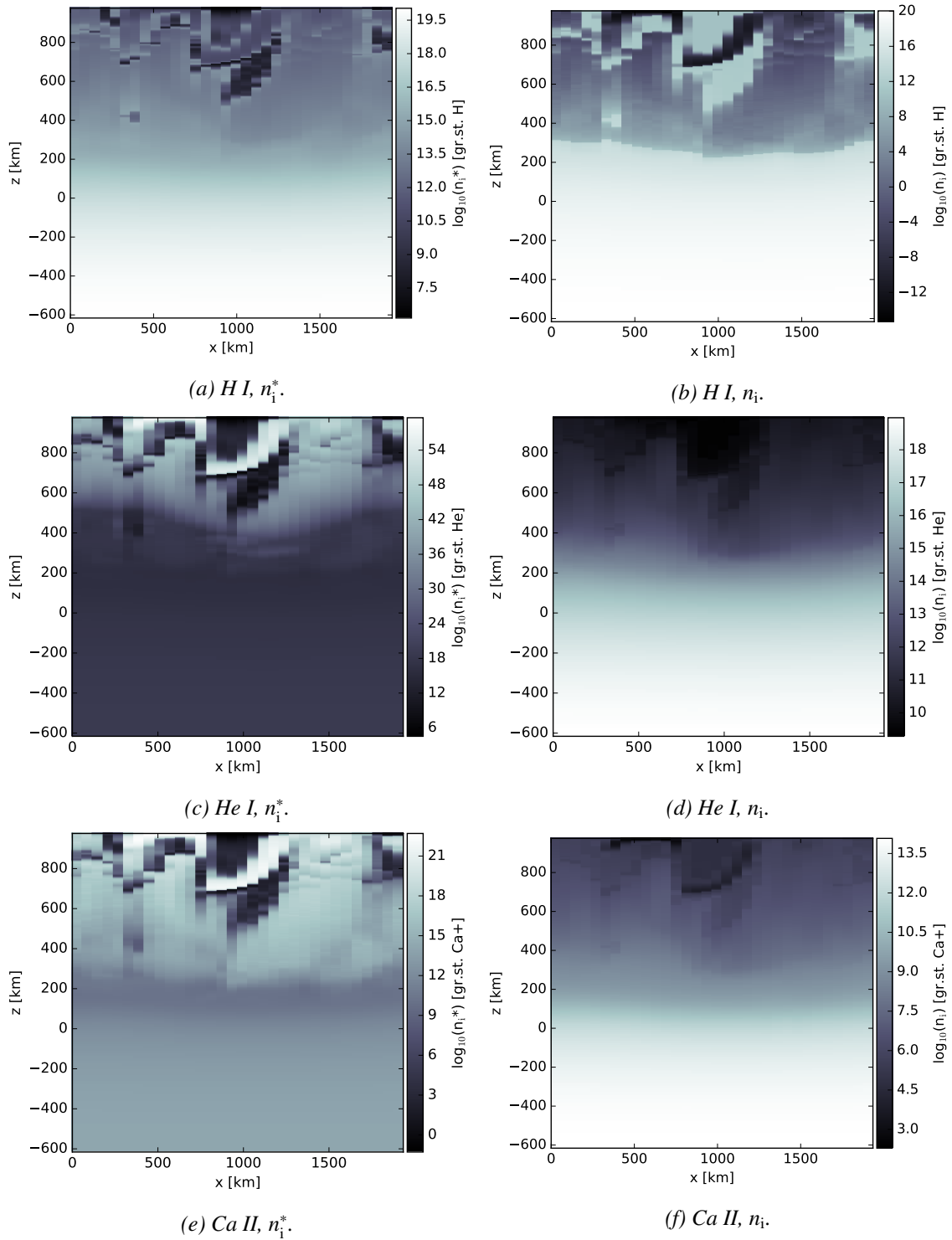


Figure 5.9: Model NL: population densities for the ground states of different ions (the colour bar is logarithmic). The left panels show the LTE population densities  $n_i^*$ , while the right panels show the actual population densities  $n_i$ . The vertical slice adopted here is the same used in Fig. 4.3a.

18 580 transitions for model NN and NL.

### Spectrum

The spectrum (Fig. 5.10a), although characterised by a lower wavelength resolution than models NN and NL, presents the typical features of early M-dwarfs spectra: the flux peak at approximately  $1 \mu\text{m}$ ; the  $\text{H}^-$  bump at  $1.6 \mu\text{m}$ ; the strong molecular absorption bands in the optical range (Fig. 5.10b); shallow (compared to the infrared) continuum with absorption/emission lines in the UV (Fig. 5.10c). Despite the strong simplification for the NLTE opacities in comparison with model NL, the two spectra are qualitatively similar.

### Flux maps

The higher spatial resolution for model NS evidently influences the appearance of the flux maps (Figs. 5.11). The horizontal resolution is roughly 16 times higher than the previous models, and the flux images reveal finer structures, when compared to model NL flux images in Figs. 5.3.

The UV continuum close to Lyman- $\alpha$  (Fig. 5.11a) shows a similar map compared to the binned resolution model (Fig. 5.3a). The Mg II k line core image (Fig. 5.11b), presents features that resemble the temperature structure at the outermost layers, like the Mg II h line for the binned model (Fig. 5.3b).

The Ca II K line core image (Fig. 5.11c) displays, as expected, a pattern similar to the Mg II h line, being both optically thick lines. The wing of the line (Fig. 5.11d) shows instead features originating from gas located deeper in the chromosphere.

The infrared map at  $1.6 \mu\text{m}$  (Fig. 5.11e), corresponding approximately to the peak of the  $\text{H}^-$  opacity minimum, shows the photospheric granulation pattern. At longer wavelengths, e.g. the  $10 \mu\text{m}$  flux map in Fig. 5.11f, the granulation pattern is still visible, but features from higher layers are also contributing to the images, with some of the intergranular lanes being actually brighter than the granules patches: this phenomenon is called *reversed granulation* and more details are given in Chapter 6.

### Departure coefficients

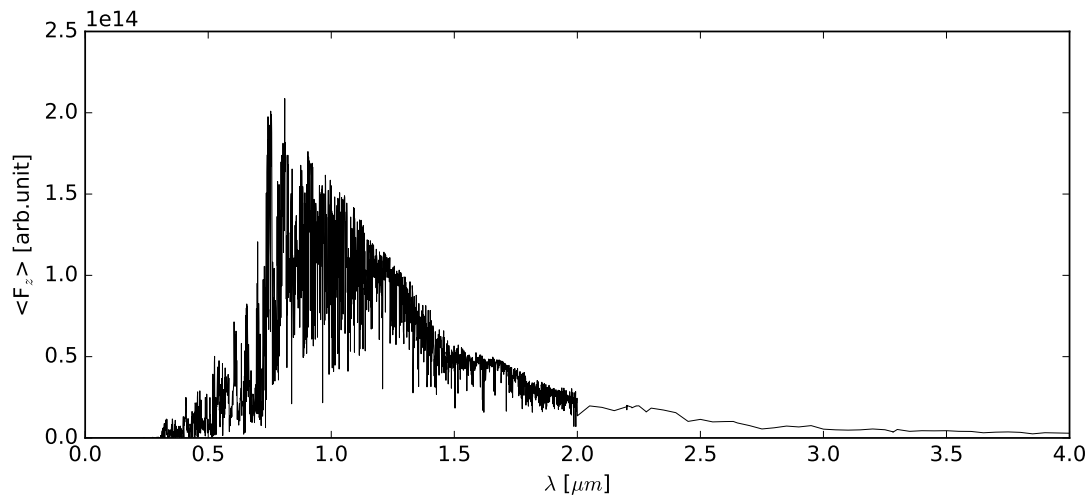
The departure coefficients for the ground state of a selection of species (H I, Mg I, Ca II) are displayed in Figs. 5.12.

In comparison with model NL (see Figs. 5.8), the departure coefficients for model NS show the same behaviour with respect to the local gas temperature:  $b_i \sim 1$  in the photosphere, low (high) values in correspondence of cold (hot) gas. Qualitatively, both models present similar development of the  $b_i$ 's through the atmosphere, but the values strongly differ. This is not surprising given the large setup difference between the two PHOENIX/3D runs.

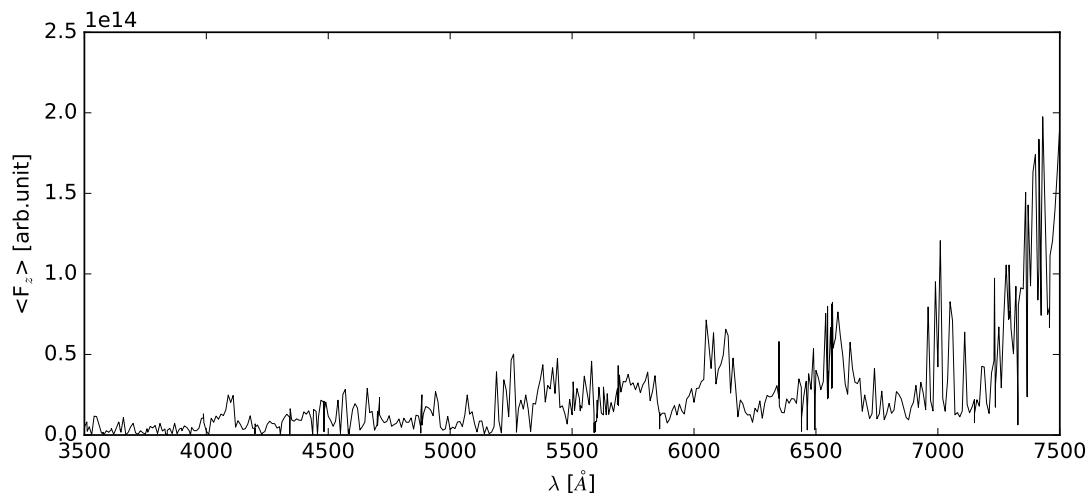
## 5.4 Aliasing artefacts

When displaying the vertical flux at the outermost layer, at short wavelengths ( $\lambda < 3000 \text{ \AA}$ ), all three models present aliasing artefacts. The artefacts are a series of concentric rings, similar to a *moiré* pattern, with the centre being a voxel with a rather high value of the corresponding physical quantity. The artefacts are very clear for images displaying the mean intensity or the vertical flux (Fig. 5.13a). The rings follow the periodic boundary condition, being connected on the opposite sides of the model box.

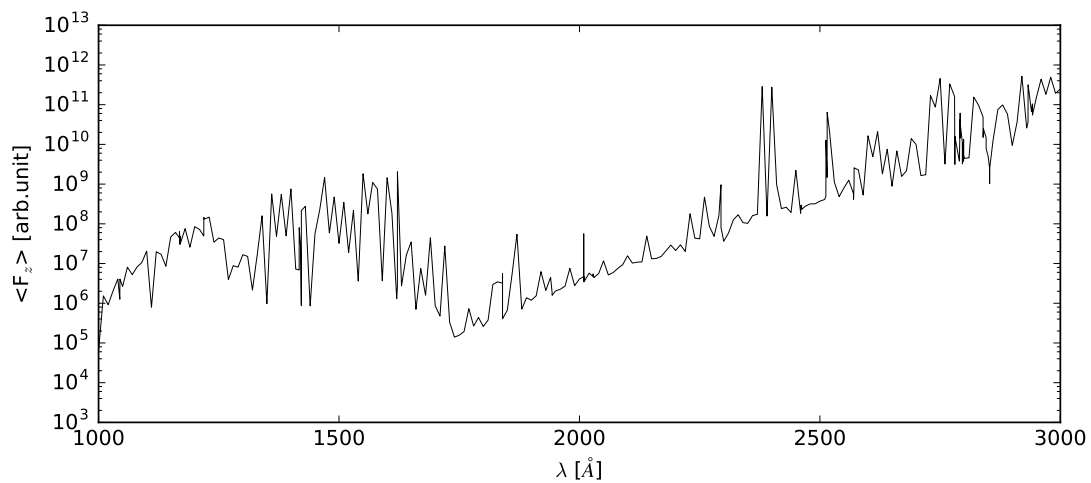
The ring-like patterns visible at the outermost layer are present also in depth. The departure coefficients may show the vertical development of the rings (Fig. 5.13b), or the horizontal pattern (upper left corner in Fig. 5.12d). Mean intensity and flux images show the same problem.



(a) Optical and infrared range.



(b) Optical range.



(c) UV range (flux scale is logarithmic).

Figure 5.10: Model NS (NLTE+LTE opacity, with reduced model atoms): flux spectrum, computed like in Figs. 5.1. The wavelength resolution is greatly reduced, in comparison to model NL (Figs. 5.2, but the spectrum is qualitatively similar).

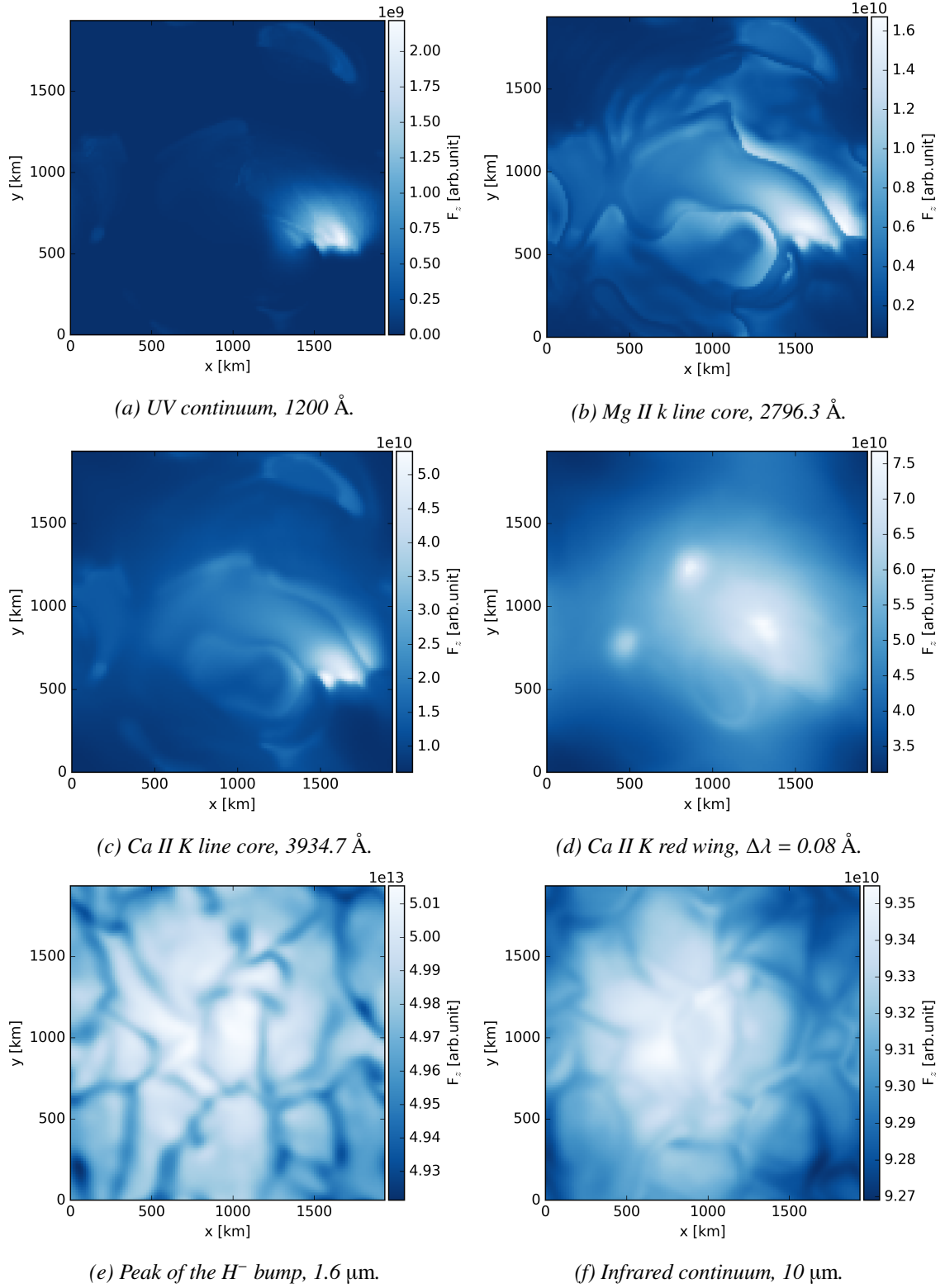


Figure 5.11: Model NS: vertical flux colour maps. The spatial resolution is approximately  $4 \times 4$  times higher than model NL (Fig. 5.3).

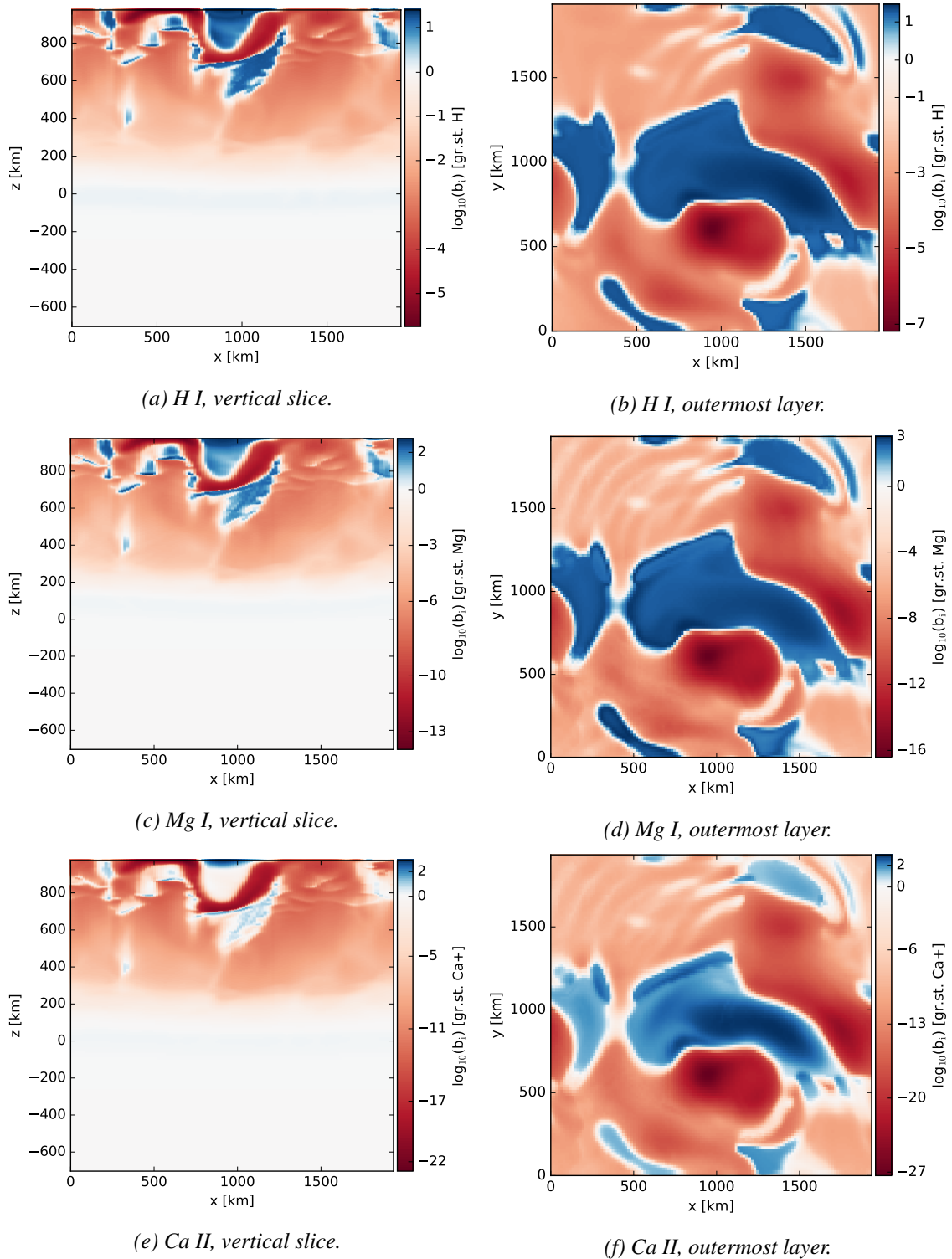


Figure 5.12: Model NS: departure coefficients for the ground state of H I, Mg I, Ca II. The plots colour-code is the same of Figs. 5.8

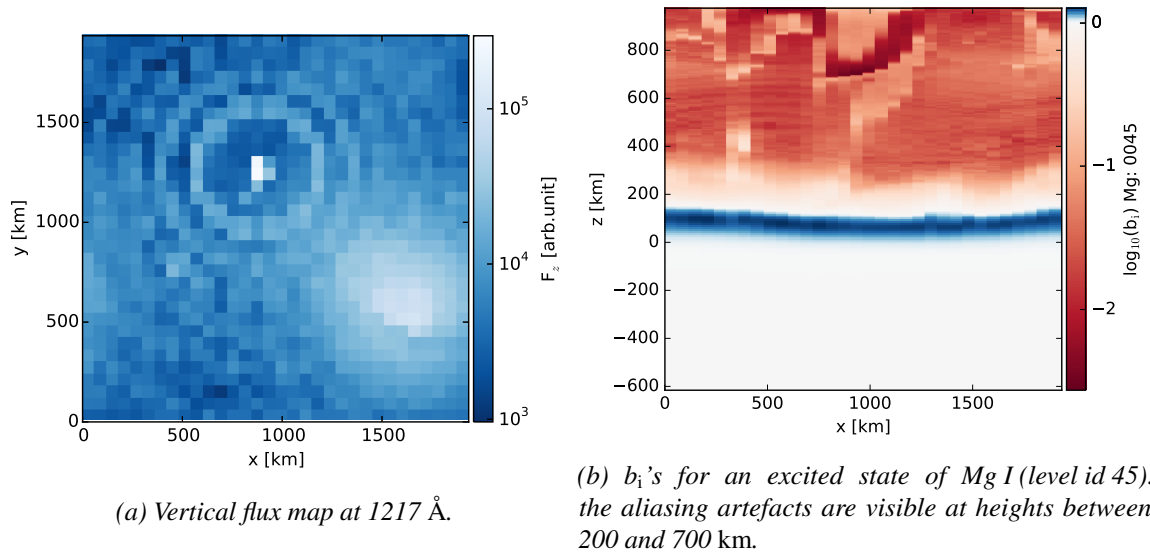


Figure 5.13: Model NL: aliasing artefacts. Models NN and NS show similar behaviours.

While not critically affecting the overall radiative field, these artefacts reveal problems in the numerical approach used for these simulations. Causes and a possible solution to this problem are discussed in Section 6.7.



# Chapter 6

## Discussion

I concentrate the discussion mostly on model NL (NLTE+LTE opacity), which is the most complex and “realistic” of the three cases presented. Model NN (only NLTE) served mainly as starting point for model NL and, beside its testing purposes, does not represent a physically realistic M-dwarf atmosphere. Model NS (small model atoms) features a lower wavelength resolution and less NLTE levels compared to models NN and NL, but used the original, high spatial resolution grid from the CO<sup>5</sup>BOLD models: this leads to interesting features not clearly observable in the low spatial resolution models.

### 6.1 Flux spectrum

The overall flux spectrum for model NL (Fig. 6.1, with reduced wavelength resolution to better visualise the broad features) resembles a typical M3V spectrum. The peak of the spectral energy distribution is around 1  $\mu\text{m}$ , while a second broad peak is clearly visible at 1.6  $\mu\text{m}$ , in correspondence to the H<sup>-</sup> opacity minimum at this wavelength. A third broad bump is visible at 2.3  $\mu\text{m}$  in correspondence of a water opacity minimum. A forest of absorption lines, mostly molecular, characterises the spectrum at optical and infrared wavelengths. We can distinguish the typical M-dwarf spectra molecular absorption bands: TiO and VO bands from 5500 to 7500  $\text{\AA}$ , water bands at 1.4 and 1.8  $\mu\text{m}$  (see Kirkpatrick et al., 1991, for an extensive list of spectral features in early M-dwarfs spectra). In the UV (Fig. 5.2d), we can see many features standing out from the shallow continuum. The UV spectrum is so crowded, i.e. rich in features, that many “apparent” emission lines are actually only spikes between absorptions. Some emission lines, like Lyman- $\alpha$  (Fig. 6.2a), Mg II h&k, etc., present emission wings and absorption cores. When comparing the UV range between model NL (NLTE+LTE opacity) and model NN (NLTE opacity) (Fig. 5.1c), we see that the latter is characterised by very few emission lines, originating exclusively from the atomic species included in NLTE treatment, compared to the former. This is due to the LTE populations for the atomic species being largely over-estimated in the chromosphere compared to NLTE (more details in Section 6.4), causing too strong emission lines in the UV. Fuhrmeister et al. (2006) reported the same behaviour for PHOENIX/1D chromospheric models, ultimately suggesting to expand as much as possible the NLTE species list.

The horizontally averaged flux spectrum may differ from the local spectrum (the vertical flux spectrum extracted from each specific voxel in the outermost layer). The Lyman- $\alpha$  local flux spectrum (Fig. 6.2a) varies over several orders of magnitude, with a large dispersion around the mean profile. On the other hand, for Ca II 8544  $\text{\AA}$  (Fig. 6.2b), minimum to maximum flux variation is only marginal, and the local spectrum does not differ from the averaged one. This is due to the vertical flux for UV continuum and lines originating mostly from narrow confined regions, e.g. Figs. 5.3a and 5.3b, while optical and infrared continua and lines emerge from most of the surface, e.g. Figs. 5.3c and 5.3d.

We can compare the flux spectrum of model NL with observed data from AD Leo (as mentioned

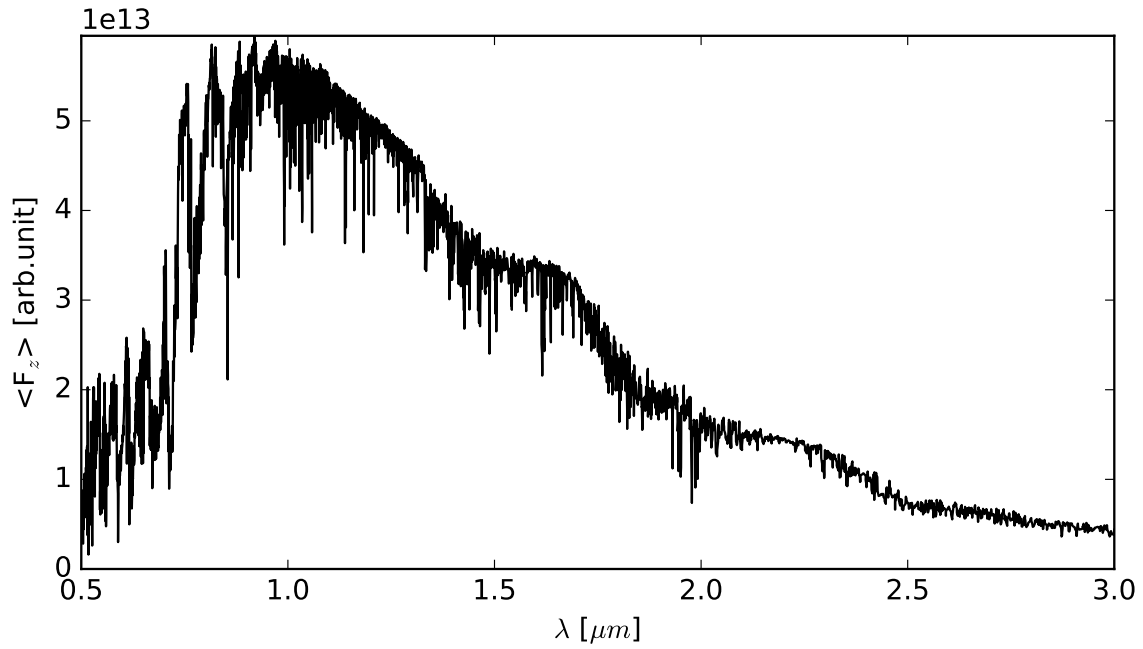
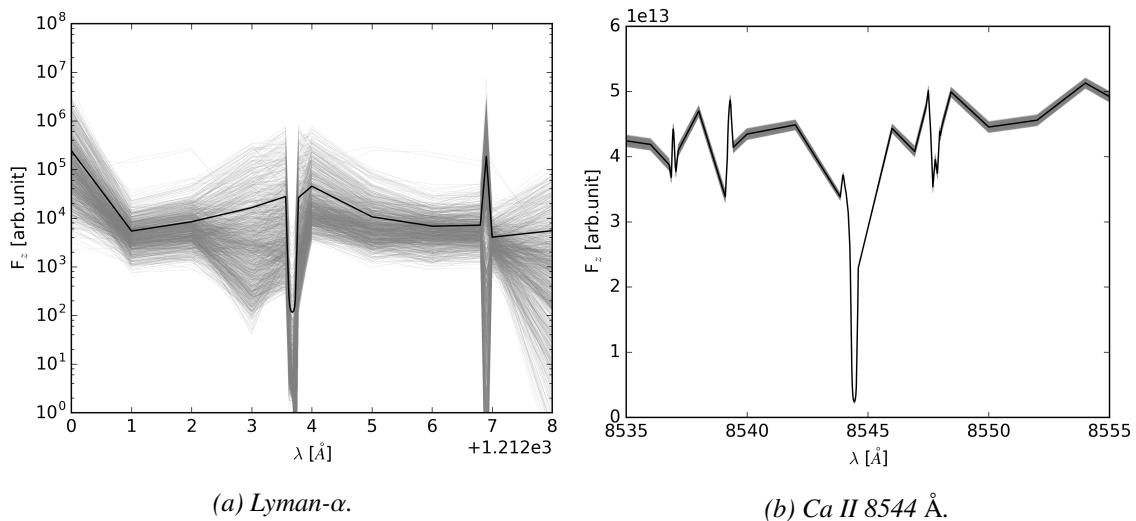


Figure 6.1: Model NL: infrared spectrum with reduced wavelength resolution (original resolution in Fig. 5.2a).



(a) Lyman- $\alpha$ .

(b) Ca II 8544 Å.

Figure 6.2: Model NL: line profiles showing the difference between the horizontally averaged spectrum (black) and the local, i.e. extracted voxel by voxel, flux spectrum (grey).

above, the CO<sup>5</sup>BOLD models grid, from which the input atmosphere was extracted, had its effective temperature and surface gravity based upon this M-dwarf). The comparison is merely qualitative: while the observed spectrum is a time-integrated disk-averaged measurement, the theoretical spectrum is computed from the vertical flux (not a physical observable) of a small portion of the whole stellar surface. Further work is necessary to improve this comparison, e.g. using a star-in-a-box model or simulate a stellar disk from several surface patches, and correctly averaging the intensity towards the observed point of view. Moreover, the input CO<sup>5</sup>BOLD model used for this work represents a low activity state of the atmosphere (low initial magnetic field,  $|B_z|_0 = 10$  G), while AD Leo is a very active M-dwarf, with the surface-averaged magnetic field estimated on the order of 3 kG (Saar and Linsky, 1985; Reiners, 2012).

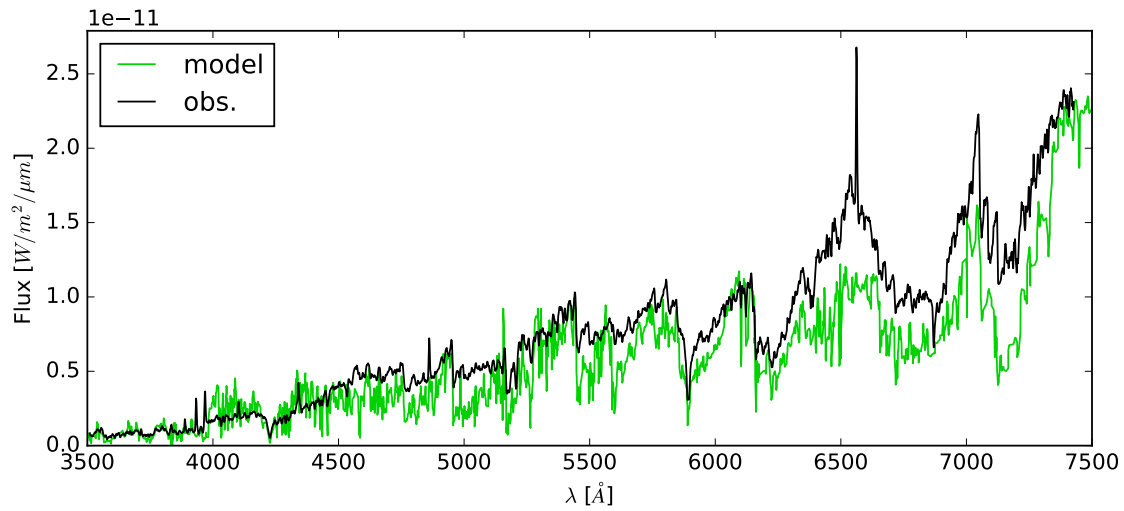
Some of AD Leo stellar properties are the following: spectral type M3.5V;  $T_{\text{eff}} = 3330$  K;  $\log g = 4.5$ ; dMe-type, i.e. H $\alpha$  in emission; flare star, i.e. active with very bright flares. The spectra were retrieved from the VizieR database (Ochsenbein et al., 2000): the optical spectrum (Fig. 6.3a), from 3500 to 7500 Å with resolution  $\Delta\lambda = 1.4$  Å, was published by Jacoby et al. (1984), while the IR spectrum (Fig. 6.3b), from 0.8 to 5 μm with resolution  $\Delta\lambda/\lambda = 0.0002$ , was published by Rayner et al. (2009). The observed spectra are flux calibrated. The PHOENIX/3D flux spectrum was interpolated to the observed spectral resolution and scaled to match the observed spectrum at the flux peak, around 1 μm.

The model spectrum does not dramatically differ from the observed AD Leo spectrum. The continuum is qualitatively similar, and the major features in the optical spectrum, i.e. the molecular absorption bands, are matching. The observed optical spectrum clearly presents emission lines: H $\alpha$ , H $\beta$ , and the Ca II H&K doublet. These features are absent in the PHOENIX/3D spectrum, but since the photospheric spectrum of the model is similar to the observed one, the reason for this difference has to be located in the upper layers, i.e. the chromosphere. As mentioned in Chapter 2, Balmer lines' presence in M-dwarf spectra is connected to the level of activity, and for very low activity the H $\alpha$  line is not observed. With higher and more localised temperatures, the excitation will be stronger and increase the strength of the emission lines; at the same time, more shock fronts and hot filaments will also increase the gas excitation and ionisation. Both scenarios require a higher degree of activity, but the models described in this work are too inactive. The CO<sup>5</sup>BOLD snapshot used for these PHOENIX/3D calculations features mild shocks and temperature gradients, in comparison to the higher initial magnetic field M-dwarf models from the Wedemeyer et al. (2013) models grid. It represented, therefore, an easier case for PHOENIX/3D, and more active models will be computed in the future.

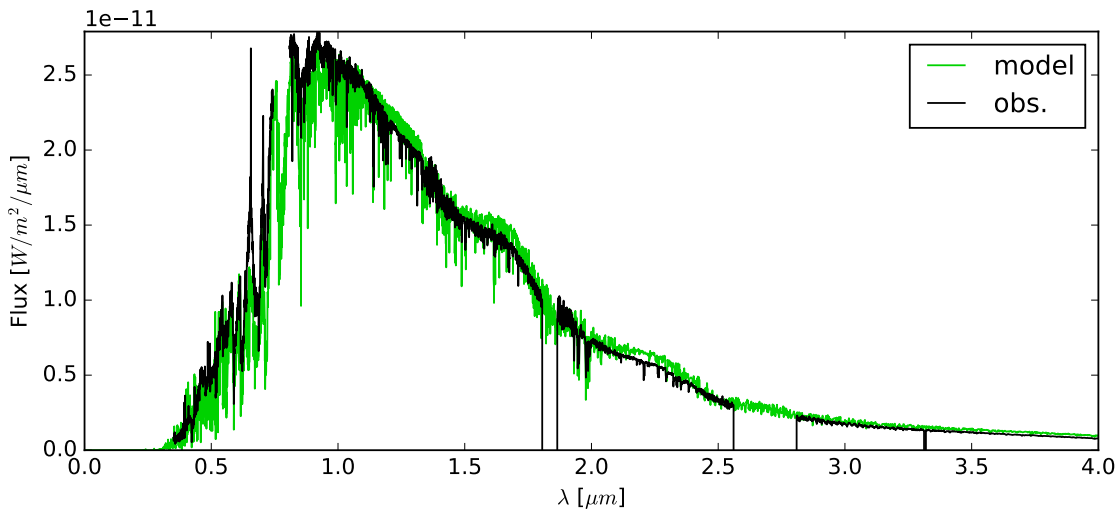
## 6.2 Synthetic images

As shown in Chapter 5, we can create synthetic images of PHOENIX/3D models from the the intensity surface maps that we can use to investigate the formation height of spectral lines and continua, and the appearance of the model at different viewing angles. Even though the vertical flux is not a physical observable, it can also be used to study the formation heights of spectral features.

Vernazza et al. (1981) thoroughly studied the depth dependence of the main spectral diagnostics for the solar chromosphere (Fig. 2.2). The line core for all the main diagnostics, i.e. Lyman- $\alpha$ , Ca II K, H $\alpha$ , etc., is formed at chromospheric heights, right below the transition region. This is due to the intrinsic high opacity of the line core: photons in deep layers do not travel large distances before being absorbed and, therefore, we only see the ones formed in the upper layers. Line wings are formed deeper in the atmosphere, at the temperature minimum or even deeper, in the photosphere. Line opacity in the wings is low and the photons can travel large distances, enough to escape the box. While VAL *solar* models assumed a 1D plane-parallel atmosphere, the 3D M-dwarf models discussed here present a more complex scenario, with the atmosphere, and especially the chromosphere, being highly inhomogeneous. Therefore, any comparison with the VAL models is mainly qualitative.



(a) Optical range.



(b) Infrared range.

Figure 6.3: Model NL: comparison between the model mean flux spectrum (green) and AD Leo archive data (black). The comparison is qualitatively successful, especially considering the strong molecular features.

### 6.2.1 Solar narrowband observations

Rutten (2007) presented images from the DOT solar telescope showing the appearance of the fibrils when observing at  $H\alpha$  line core and moving towards the line wing (Fig. 6.4). At the line core (rightmost frame in Fig. 6.4), the observations show the fibrils uniformly covering the solar surface, extending shortly above the surface when looking at the limb, i.e. within the chromosphere. At the line wing, the ensemble of fibrils disappears, and the photons originate mostly from the photosphere, with localised dark features due to blue-shifted fibrils.

Although the models described in this work simulate a M-dwarf atmosphere, we can investigate the height of formation of lines and continua in a way similar to the observations described above using the flux vector and intensity data, and qualitatively compare the results to solar chromosphere models.



Figure 6.4: From Wedemeyer-Böhm *et al.* (2009), original figures in Rutten (2007). DOT solar narrow-band observations at wavelength close to  $H\alpha$ . From left to right, the wavelength shift from line core, i.e.  $\Delta\lambda = \lambda - \lambda(H\alpha)$ , is -800, -600, -400, and -200 mÅ.

### 6.2.2 Model NL: flux images

With vertical flux images we can produce line-scans of spectral features, similarly to the observations described above (although the radiative flux is not a physical observable). Unlike the solar observations from Rutten (2007), for these models we cannot use  $H\alpha$  because it is absent as photospheric and chromospheric line (as mentioned in Section 6.1). Figure 6.5 displays a vertical flux line scan of Ca II K. The flux at line core (bottom-left in Fig. 6.5) shows features that resemble the gas temperature in the upper regions. It is, however, not exactly matching the outermost layer (Fig. 4.3d), because the photons escape from a broad range in depth, not only from the box top boundary. Like for the Mg II h line core (Fig. 5.3b), the flux peaks in regions with very low temperature. Moving away from the line core, the appearance changes from well defined structure to a diffuse emission: in this case photons are tracing a large range in height. At the line wing, the flux image shows the granulation pattern. This behaviour for the M-dwarf 3D models agrees with the above mentioned plane-parallel scenario of the solar VAL models and the narrowband  $H\alpha$  solar observations.

We use the vertical component of the flux vector to generate the flux spectrum and flux maps. Moreover, we can use the horizontal components of the flux vector to visualise the propagation of the radiation across the xy-plane, using an arrow field. If the flux vector is defined as  $\vec{F}_\lambda = \vec{F}_{x,\lambda} + \vec{F}_{y,\lambda} + \vec{F}_{z,\lambda}$ , the vertical flux is  $\vec{F}_{z,\lambda}$ , while the horizontal flux is  $\vec{F}_{x,\lambda} + \vec{F}_{y,\lambda}$ . In Figs. 6.6, the cell colour represents the vertical flux, while the arrow represents the horizontal component, with the length of the arrows normalised to the maximum horizontal flux value for that wavelength.

The horizontal flux field also follows the temperature structure at the layers where the line or continuum is formed. Horizontal and vertical magnitudes are clearly correlated. The best example is in Fig. 6.6a. In this picture, the cells with the strongest horizontal flux field are close, but not coincident, with the cells with the highest vertical flux. Photons flow from hot regions to cold regions, and given the three-dimensional structure of the model, the escape can happen towards any direction.

In the optical continuum (Fig. 6.6b), we see a similar case, with the horizontal flux being directed towards the intergranular lanes, where the temperature is lower.

For longer wavelengths, the differences between the vertical flux maps at 10  $\mu\text{m}$  and 0.1 mm (Figs. 5.3e and 5.3f) are more distinct than the horizontal flux maps at the same wavelengths (Figs. 6.6c and 6.6d). The first clearly show the granulation pattern and only marginal differences in flux, while the latter feature a slightly different horizontal flux field. This is likely due to the interplay of the main opacity sources at long wavelengths. As shown in Vernazza *et al.* (1981), for the solar chromosphere, the continuum at 10  $\mu\text{m}$  is dominated by  $H^-$  free-free opacity. This is true also at 0.1 mm, but at this wavelength free-free transitions on neutral hydrogen become also important, and dominant at wavelengths longer than 1 mm. Moreover, for the solar chromosphere, at sub-millimetre and millimetre wavelengths, the continuum formation height increases with increasing height. There-

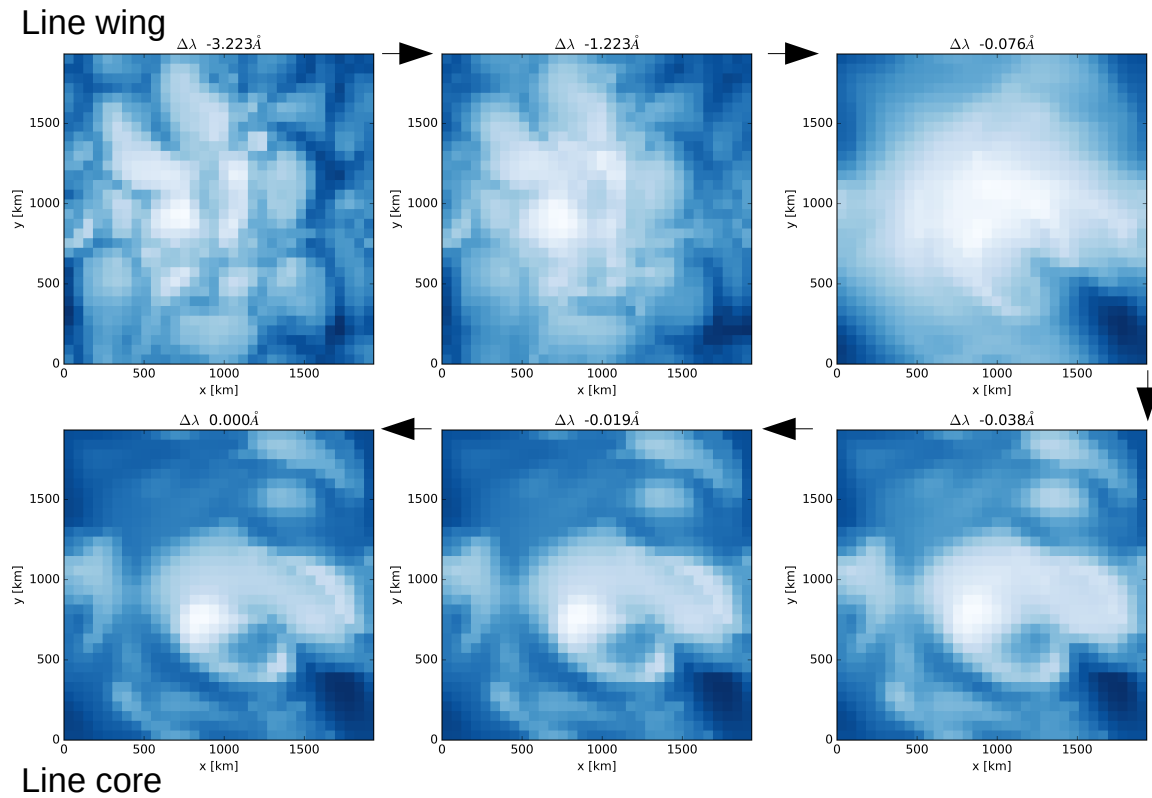


Figure 6.5: Model NL: vertical flux line scan of Ca II K. Clockwise from the top-left frame, the images go from  $-3.2 \text{ \AA}$ , i.e. blue wing, to the line core.

fore, radio observations can be used to probe the temperature structure of the chromosphere (e.g. ALMA observations of  $\alpha$  Cen described by Liseau et al., 2015).

### 6.2.3 Model NL: intensity images

Intensity images generated with the imager allow us to corroborate the relation between the flux images and the height of formation of lines and continua.

Also in this case, I focus on the Ca II K line. Intensity maps at the wing (Fig. 6.7) show, for  $\mu$  close to 1, the granulation pattern, with low contrast between the intergranular lanes and the granules. Looking closer to the limb, the granulation pattern is still visible but the total intensity decreases. At the limb the intensity reaches eventually zero. At the line core (Fig. 6.8), we see, like for the flux images (Figs. 6.5), the temperature structure of the upper layers. For lower  $\mu$ 's, the total intensity does not steadily decrease and the bright patches seen “face-on” are still bright. We have to look very close to the limb to observe a fully dark surface: the photons traverse a longer path and are more likely absorbed, and at the same time the projected area decreases.

Varying both solid angles also manifests the difference in depth of formation between wing and core of absorption lines. When displaying the intensity field at different angles, the features observable in the line wing (intergranular lanes, granules, bright patches, etc.) repeat themselves (Fig. 6.9). This behaviour is not observable for the line core features (Fig. 6.10). This is due to the periodic boundary conditions and parallax effects. Increasing the inclination, i.e. the angle between the observer and the line perpendicular to the surface, the features that originate deep in the model will re-appear on the other side. This effect is only marginal for the line core, because the photons are created close to the upper boundary. A sketch of the effect is shown in Fig. 6.11.

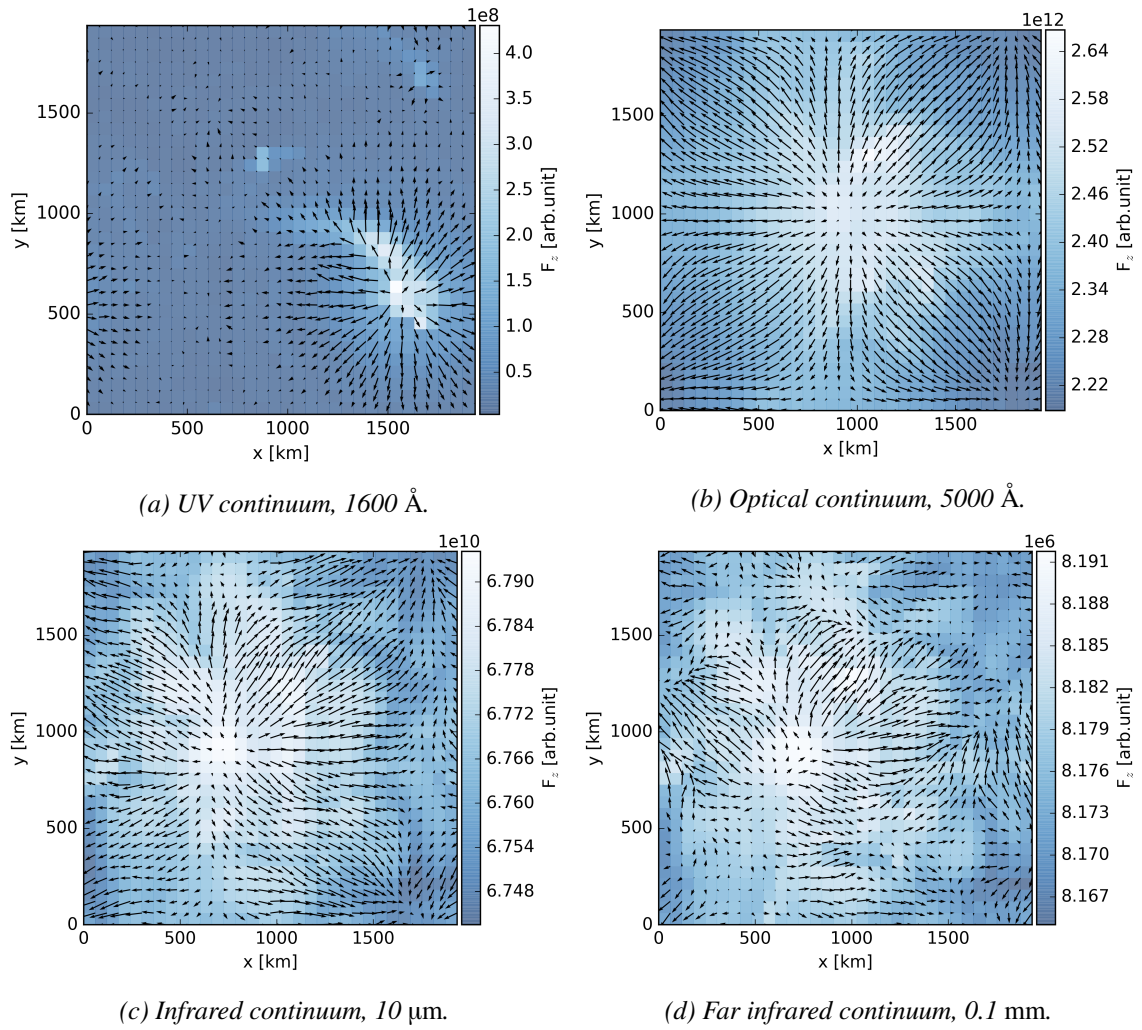


Figure 6.6: Model NL: vertical flux colour maps with super-imposed arrow field for the horizontal flux. The length of the arrow is normalised to the maximum value of the horizontal flux at each wavelength.

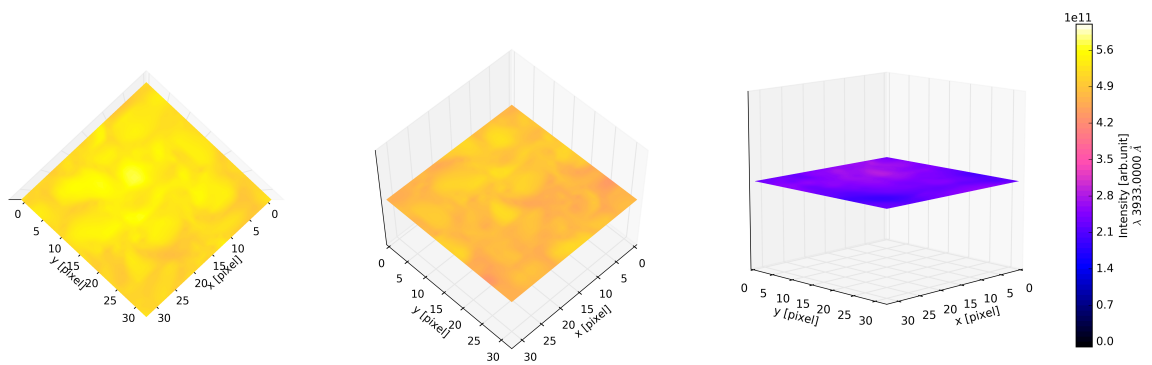


Figure 6.7: Model NL: intensity images for Ca II K, blue wing.

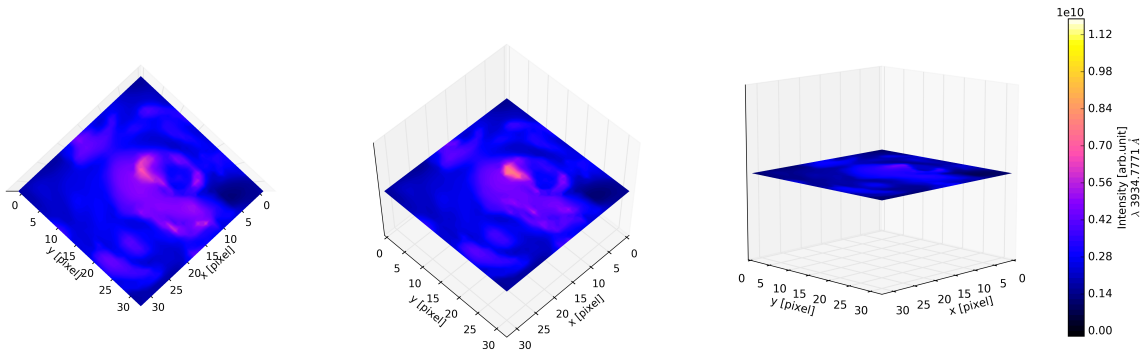


Figure 6.8: Model NL: intensity images for Ca II K, line core.

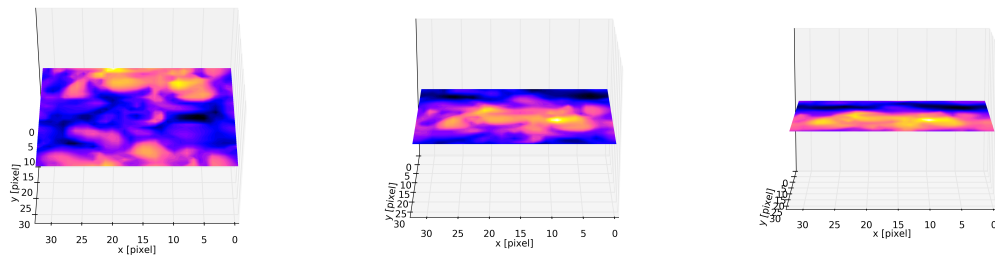


Figure 6.9: Model NL: intensity images for Ca II K wing. The intensity colour range is normalised for each frame.

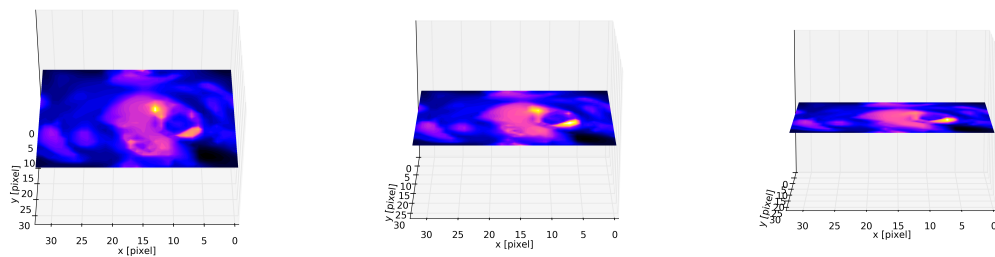


Figure 6.10: Model NL: intensity images for Ca II K core. The intensity colour range is normalised for each frame.

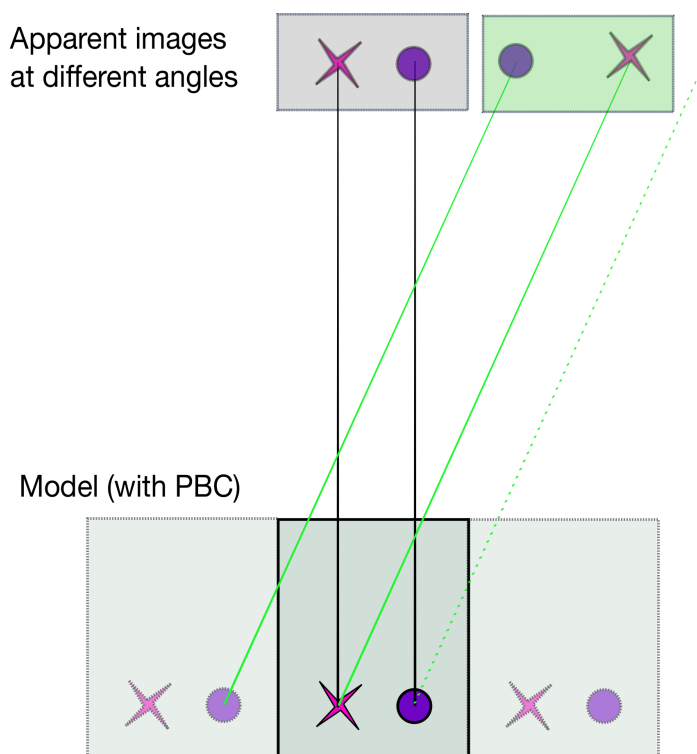


Figure 6.11: Sketch of the parallax effect due to the periodic boundary conditions (PBC). When looking at lower inclination, features may re-appear on the other side of the apparent image, if they are located in deeper layers inside the box.

### 6.3 Mean vs. median 1D profiles

With 3D models we can investigate the connection between spatially averaged spectral diagnostics and the local, unresolved structure of a stellar atmosphere. When comparing multi-dimensional simulations to disk-averaged, column-density-weighted observations, or to 1D models, it is necessary to reduce the dimensionality of the problem. For this purpose, a standard procedure is to “collapse” the 3D information into 1D profiles.

For a structure with  $n_x \times n_y$  cells per horizontal layer, the mean, or average, of a certain quantity  $Q$  within a layer is simply  $Q = \sum_{i,j} Q(i,j)/n_x n_y$ . Repeating this step for each layer, we build a 1D vertical profile for  $Q$ . The median is another useful statistical indicator with a different purpose: it is the value that halves the sample into two “equally populated” sub-samples. In specific cases, for instance with uniform or Gaussian probability distributions, mean and median are identical, but, generally, the two values are different. Specifically, the median is less affected by outliers and skewed data, providing an estimate of the value that is “most common” in the sample. When constructing 1D profiles from 3D data, a comparison between the mean and the median profiles can provide interesting insights on the physical properties of the model.

The first example is the flux spectrum. The flux spectra shown in this and the previous chapters are computed from the average across the outermost layer of the vertical component of the flux. If we compute the median flux spectrum, and then compute the ratio between mean and median spectrum, we obtain the curve in Fig. 6.12. The ratio differs from 1 for wavelengths below 4000 Å and varies over several orders of magnitude. The ratio curve presents spikes, which coincide with the lines observed in the UV range (Fig. 5.2d). This is due to the outgoing flux being concentrated in small patches, which are usually much brighter than the surrounding, as also visible in Fig. 5.3a. Thanks to this plot, we can infer, without visualising the surface flux for each wavelength point, that the UV and far-UV vertical flux, for lines and continuum, is concentrated in small areas, while optical and

infrared photons emerge throughout most of the surface (as mentioned in Section 6.1).

Another example comes from the departure coefficients. Figure 6.13 displays the departure coefficients, for the ground state of hydrogen, extracted from each column of the box. Each point represents the  $b_i$ 's value in a voxel, and different colour means different column. The average and median profiles are plotted as a black and blue line, respectively. The mean  $b_i$ 's profile shows the departure coefficients increasing, on average, with height. The median profile displays an opposite behaviour, with the departure coefficients decreasing with height. The high values for the  $b_i$ 's are due to hot gas, while the low values are due to cool gas (see Section 6.4). The median profile is heavily weighted on the large number of voxels with low departure coefficients, while the mean is strongly affected by very high, but few, values within a layer. In this case, we can consider the median profile as an indicator of the most probable (similarly to the statistical mode) conditions in the model, while the mean profile simply shows the average conditions.

A final example comes from investigating the concentrations of carbon ions and molecules. In M-dwarf atmospheres, a large fraction of carbon is trapped in CO (Allard et al., 1997): we can easily confirm this by comparing the vertical profiles for neutral carbon, singly ionised carbon, and carbon monoxide (Figs. 6.14a, 6.14b, and 6.14c). CO mean and median profiles are essentially identical, which confirms that CO is an abundant molecule in the photosphere and also in the chromosphere. Some voxels present very low CO concentrations in correspondence with high temperature. C I and C II concentrations feature different profiles: the steady decline in concentrations from the bottom up to +200 km chromosphere, simply due to the decreasing density, is followed by large variations in the outer layers. The mean profile shows C I and C II concentrations being almost constant with height for the upper layers, while the median profile presents a steady decline. This difference is again due to the “logarithmic” contrast within specific horizontal layers. The high temperatures in hot filaments and shock fronts (few, very narrow and confined regions, as shown in Section 4.3.1) are responsible for the dips in CO concentrations. As a result, where CO dissociates, more C I and C II is present. Therefore, for the upper layers, while most of the voxels are characterised by low neutral and ionised carbon concentrations, the model presents, on average, high concentrations, but only due to few small regions of enhanced CO dissociation. This scenario may differ if we do not assume time-independence and instantaneous chemical equilibrium. For instance, shocks may heat up the gas on time scales shorter than the dissociation time scale of CO. Consequently, free carbon and oxygen concentrations may largely differ from the instantaneous chemical equilibrium values (Wedemeyer-Böhm et al., 2005).

## 6.4 NLTE effects

The NLTE departure coefficients measure how much the real population densities differ from the LTE case, for which the values are dependent only on the local temperature and density.

As shown in the Section 5.2, the  $b_i$ 's for any level, of any species, present values close to 1 for layers below  $z \sim 0$  km. Hence, LTE conditions are met in the lower regions of the model, corresponding to the photosphere. Above the  $z \sim 0$  km layer, the  $b_i$ 's vary strongly from level to level, for each species.

Extracting the vertical profile for  $b_i$ 's, temperature, density, and pressure, from one column of the model, we can evaluate the relation between the thermodynamic quantities and the departure coefficients. In three different panels, Figs. 6.15a, 6.15b, and 6.15c, the  $b_i$ 's for all levels of C I are displayed with the  $T$ ,  $\rho$ , and  $P$  profiles (blue line), respectively. The different C I levels are colour-coded: black for levels close to the ground, light orange for levels close to the continuum. The departure coefficients in the photosphere take value 1 (with deviations being on the order of  $10^{-4}$ ) for each level. This is true also for the other species. The gas is in LTE conditions and the population densities are set accordingly to the Saha-Boltzmann distribution. The radiation that emerges from the lower region of the box is, therefore, very similar to a black body of approximately 3300 K.

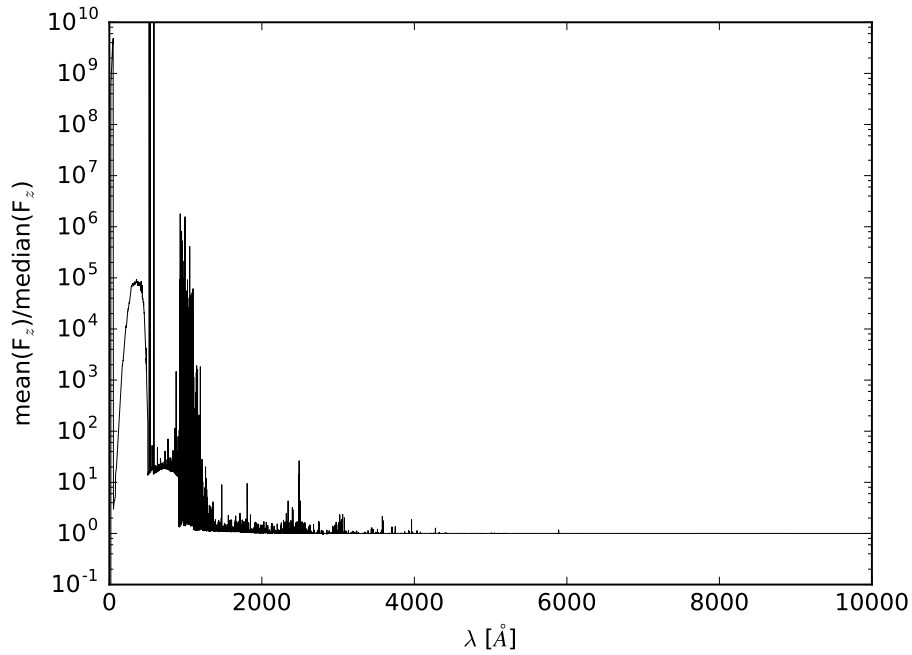


Figure 6.12: Model NL: ratio between mean and median flux spectrum. The spikes correspond to absorption and emission lines in the short wavelength interval.

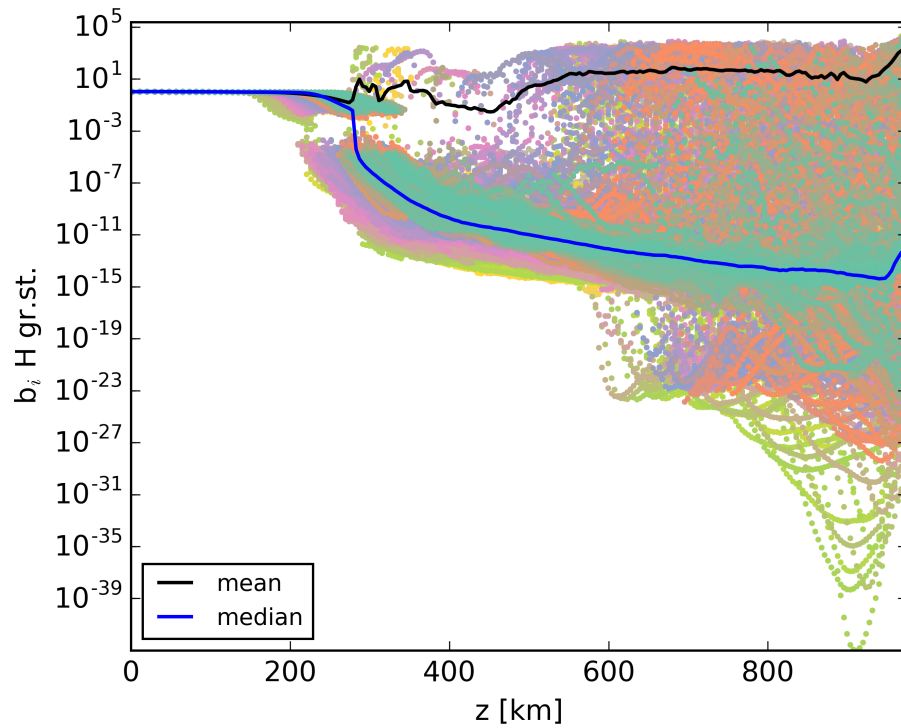


Figure 6.13: Model NL: H I ground state departure coefficients in the chromosphere. Each voxel  $b_i$  is represented by a point, colour-coded to its respective grid column. The black and blue curves represent the vertical profiles for the horizontal mean and median curves, respectively.

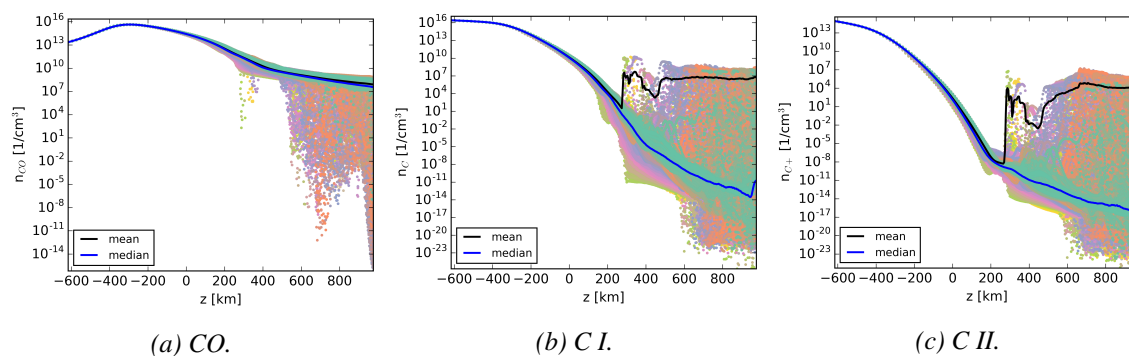


Figure 6.14: Model NL: concentrations for CO, C I, and C II, plotted against height. Colours set like in Fig. 6.13. The vertical profiles for the mean and median across the horizontal planes are the black and blue curve, respectively.

Due to the density being low in the chromospheric layers, collisional rates do not play an important role and the population densities do not follow LTE values in the upper layers. Comparing the profiles, we can see that the development of the  $b_i$ 's with altitude is mostly controlled by the temperature. This suggests that the radiative rates are dominating the populating processes against the collisional processes. The  $b_i$ 's profiles also show small features that are not visible in the temperature profile: this is due to the influence of the surrounding environment.

In Figs. 6.16, the left frames display the  $b_i$ 's mean vertical profile for each level of H I, He I, and Ca II, while the right frames show the median profile. The layers for heights less than 0 km are omitted because the  $b_i$ 's take value 1 for each level, for each species.

At higher layers, the  $b_i$ 's median profiles, for the low levels, show a quasi-monotonous decline. This behaviour is valid for each species, not only the ones showed here. The density decreases with height, and the collisional rates do not dominate over the radiative rates. The gas temperature decreases, on average, with height. The atoms “see” photons that are “hotter” than the local conditions. This influences the bound-bound transition rates: there are more energetic photons, responsible for upwards transitions, than expected from the LTE rates. Therefore, the population densities in the lower levels are under-populated with respect to LTE, i.e.  $b_i \ll 1$ .

If the lower levels are under-populated, the upper levels may in turn show weaker departure from LTE or be over-populated, with  $b_i$ 's larger than 1. The uppermost levels have  $b_i$ 's close to 1: this is due to the large collisional rates between these states and the continuum.

In regions with high gas temperatures, the departure coefficients increase. We observe this behaviour clearly in Fig. 6.15a. The explanation is similar to the previous case, with reversed arguments. The radiation field is “cold” compared to the local gas conditions. There are less upwards-transitions than under LTE conditions, hence the states are over-populated, and  $b_i \gg 1$ . Also in this case, the lower states show stronger departures than the higher states.

At the shock fronts, going from hot to cold gas, the  $b_i$ 's take extremely small values, as shown in Figs. 5.8. The very low density and the multi-dimensionality of the problem play a big role for this effect. The hot gas at the shock fronts, concentrated in few voxels, emits energetic photons, especially UV continuum and strong lines. This enormously enhances the excitation, i.e. upwards transitions, in the low density gas around the shock fronts. Ultimately, the states are strongly under-populated compared to the LTE case.

The shocks' fronts are localised regions in the models, but the photons originating from these areas influence a large fraction of the model box around them. This is visible in the right frames of Figs. 5.8, where the voxels with the lowest  $b_i$ 's are very close to high  $b_i$ 's voxels. This also agrees with the Mg II h and Ca II K line core flux images, in Fig. 5.3b and bottom-left panel in Fig. 6.5 respectively. Both spectral lines appear as absorption lines in the flux spectrum. However, in the flux

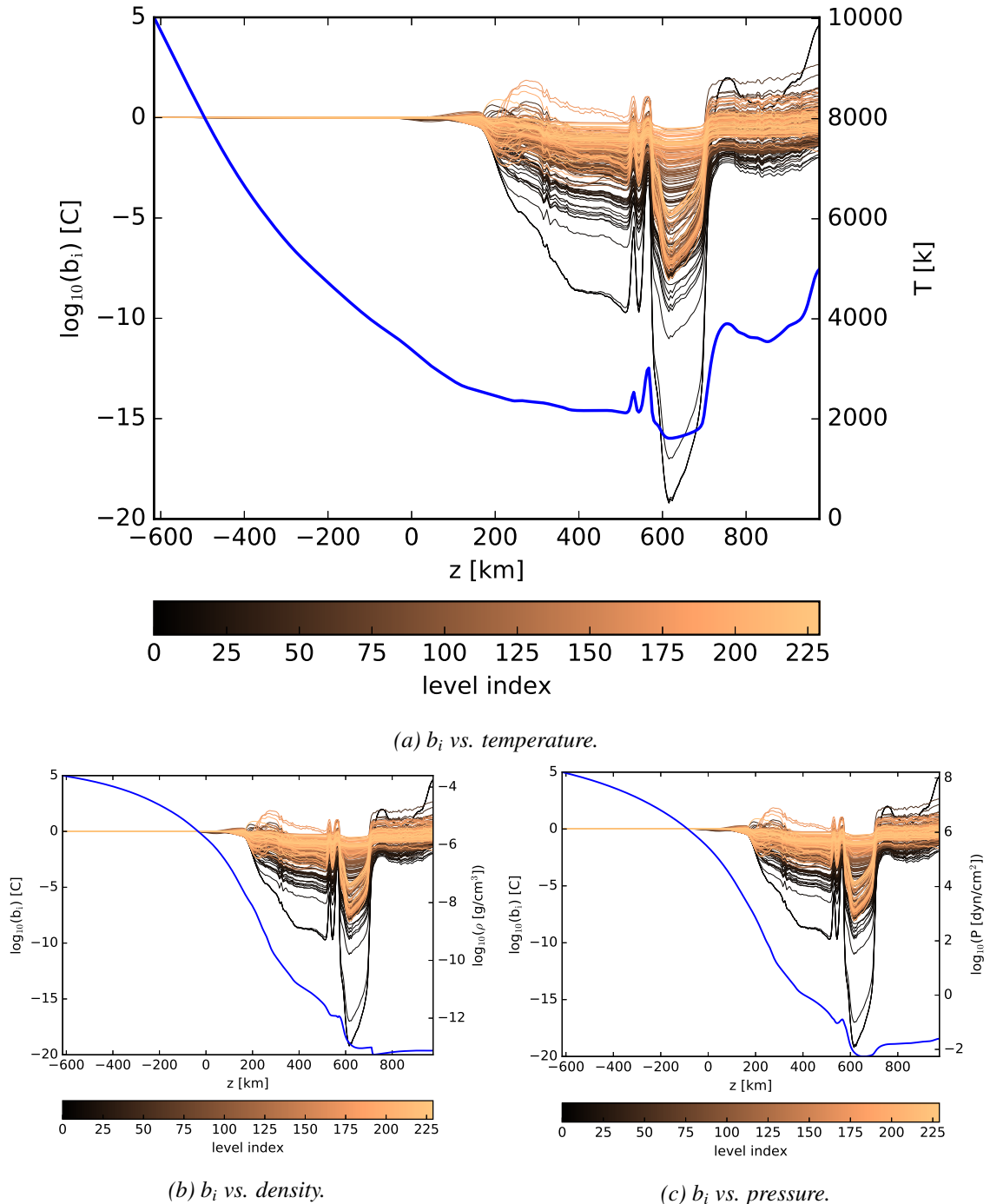


Figure 6.15: Model NL: departure coefficients for C I, extracted from a single column, plotted against height, along with temperature, density, and pressure (the blue line in each respective graph); each level treated is colour-coded (black, ground state; orange, uppermost state).

maps, the highest flux values spatially correspond to regions with low temperatures. The photons escaping from this cold gas pockets likely originate deeper in the atmosphere, in layers with higher temperatures, or they are scattered from the sides. Due to the low temperatures, Mg and Ca are mostly neutral, and the photons simply escape without being absorbed.

For layers close to the top boundary, both mean and median profiles of  $b_i$ 's increase, for each species, for each level. This is due to the average temperature slightly increasing in the uppermost layers, as seen in Fig. 4.2a.

As mentioned above, the departure coefficients depend simultaneously on density and temperature. In Figs. 6.17, the departure coefficients, extracted voxel by voxel, are colour-coded and plotted against temperature and density. We clearly see that the most extreme values of the  $b_i$ 's correspond to regions with very low density, and high or low temperature.

## 6.5 Species concentrations

In Section 6.3 I showed how atomic and molecular species concentrations are tightly connected, when they include the same species, and how they depend on the temperature structure of the atmosphere. We can explore the dependency between chemical concentrations, gas density and temperature in one single graph. Figures 6.18a and 6.18a display CO and water concentrations, respectively. Both molecules dissociate where the gas is rarefied and the temperature increases, with water being more sensitive to the temperature in the density range available in the model (respectively, CO and water dissociation energies are 11.09 eV and 5.11 eV, Allen and Cox, 2000).

Treating atomic or molecular species in NLTE has strong influence on the species concentrations. For example, we can compare the concentrations of LTE and NLTE species that share similar chemical properties. Figures 6.19 show the concentrations, for the same vertical slice, of neutral and singly ionised helium and neon, which belong to the same group of the periodic table, feature similar first ionisation potentials, and do not form molecules in stellar atmospheres. Neon I-II and He II are treated in LTE, while He I is treated in NLTE. However, the degree of ionisation of neutral helium and, therefore, He II concentrations, depend on the actual NLTE level populations of He I. Neutral helium and neon present similar profiles (Figs. 6.19a and 6.19c), but He II and Ne II clearly differ (Figs. 6.19b and 6.19d). In particular, the Ne II profile follows very clearly the temperature structure in the same vertical slice (Fig. 4.3a). While the neon ionisation degree is solely dependent on the local conditions (LTE), He II concentrations are strongly related to He I concentrations, which depend on He I population densities that are calculated in NLTE, thus being sensitive to the surrounding radiative field. The departure coefficients for neutral helium (Fig. 6.16d) show large under-populations in the outer layers, and this agrees with the high concentrations of ionised helium at the same heights. The high chromospheric concentrations of Ne II (the highest values are close to the top boundary) hint at high degrees of excitation and ionisation for this species. Other LTE species show similar behaviour. This effect is tightly connected to the forest of strong LTE emission lines observed in the UV spectrum of model NL.

A similar comparison between calcium and strontium (both alkaline earth metals with similar first and second ionisation potentials) for the concentrations of the outermost layer exhibits the difference between a NLTE and a LTE species (Figs. 6.20). The corresponding temperature map is shown in Fig. 4.3d. The neutral strontium (Fig. 6.20a) concentration is almost strictly temperature-regulated: low (high) values at higher (lower) temperatures. Singly ionised strontium (Fig. 6.20b) also clearly follows the temperature profile. For neutral and ionised calcium (Figs. 6.20c and 6.20d), the concentrations do not follow the temperature map. The low concentration areas visible in both pictures, corresponding to the lowest temperature in the layer, suggest that there calcium is trapped in molecules, mainly CaH and CaOH (Figs. 6.20e and 6.20f). These molecules are important opacity sources, responsible for absorption bands in the optical and infrared, with CaOH being mostly observed in late M and L-dwarfs (Reid et al., 2000; Reid and Hawley, 2005). The models

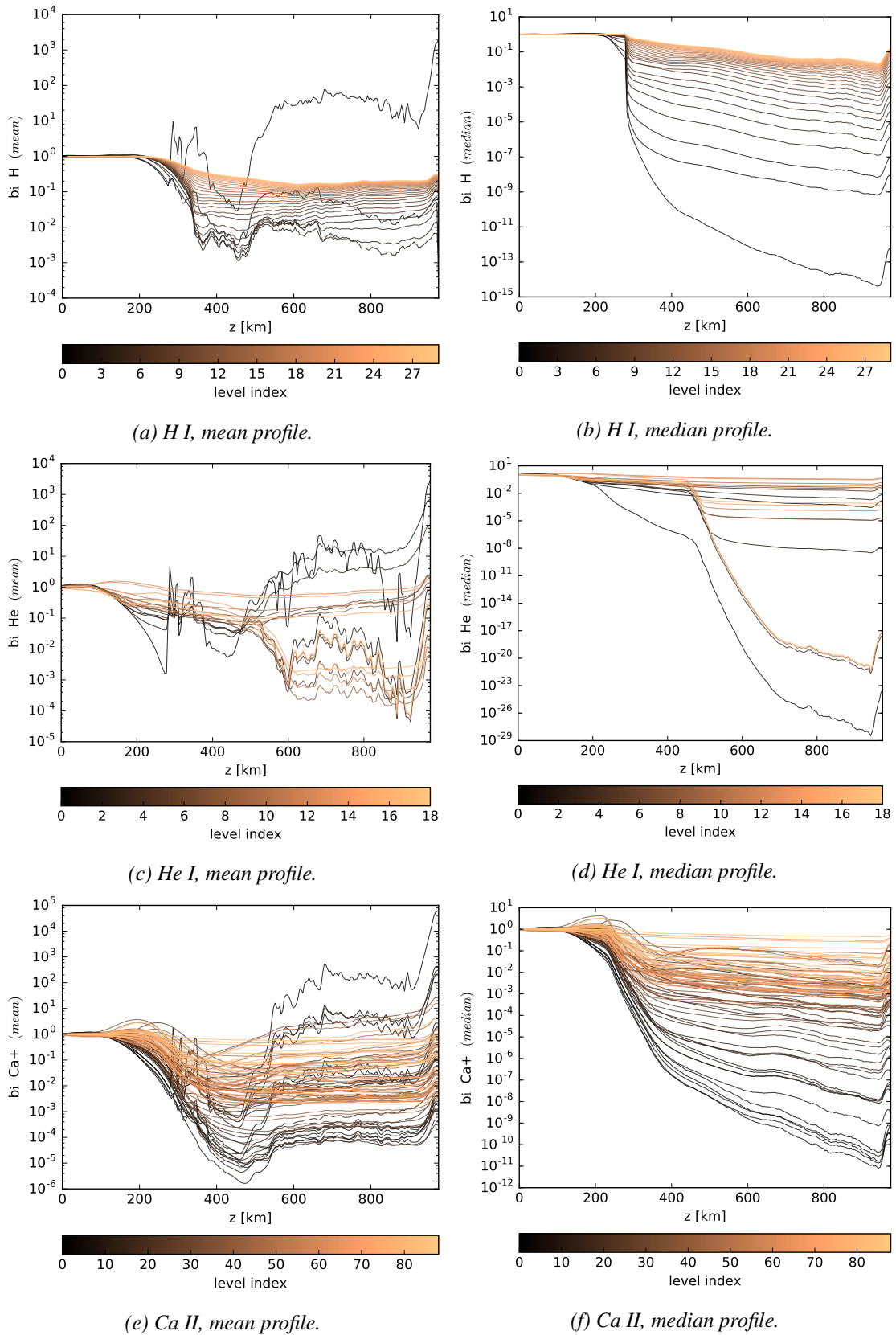


Figure 6.16: Model NL: mean and median vertical profiles for departure coefficients in the chromosphere. Each level treated is colour-coded (black, ground state; orange, uppermost state).

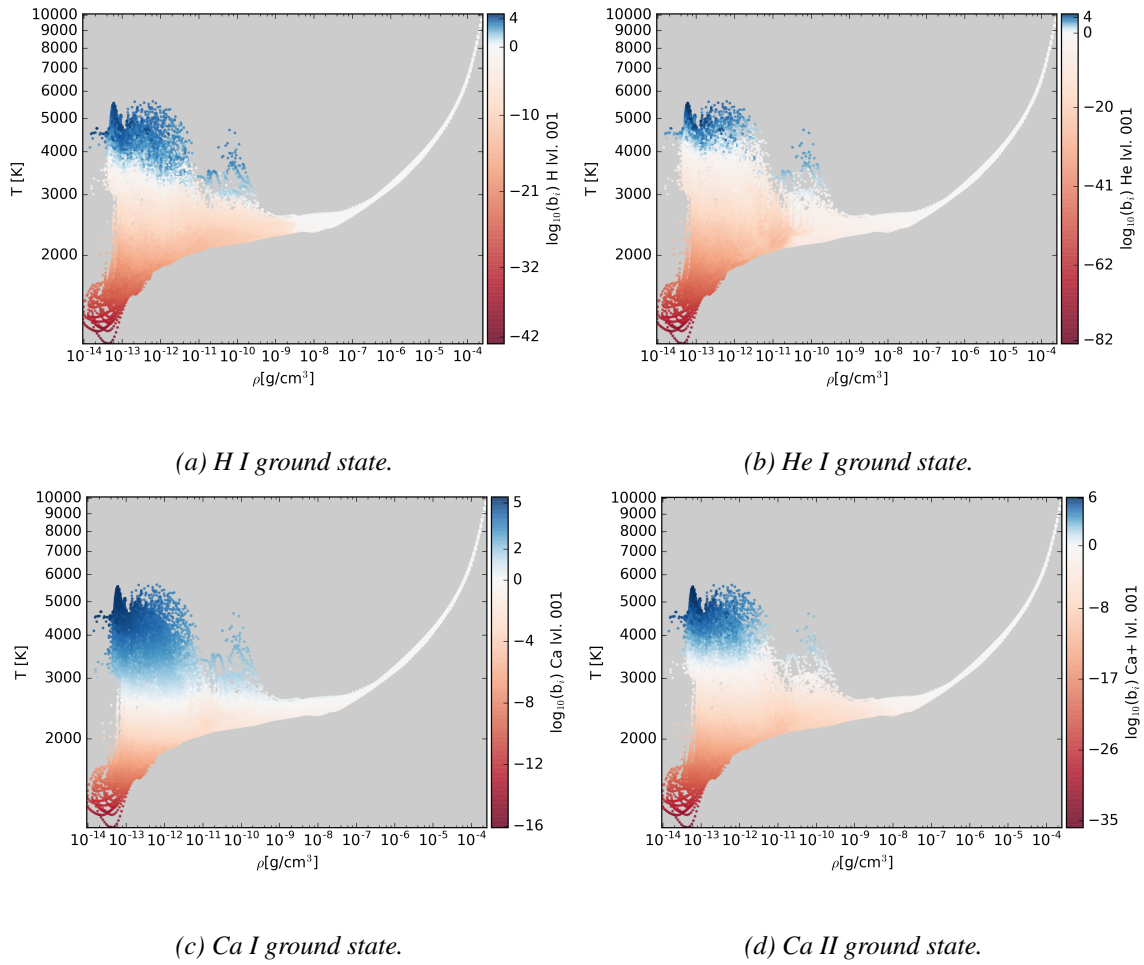


Figure 6.17: Model NL: departure coefficients for the ground states of H I, He I, Ca I and II, extracted voxel by voxel and colour-coded, plotted against the local temperature and density. The  $b_i$ 's take the highest values in regions with low temperature - low density, while the lowest values correspond to low density - low temperature regions.

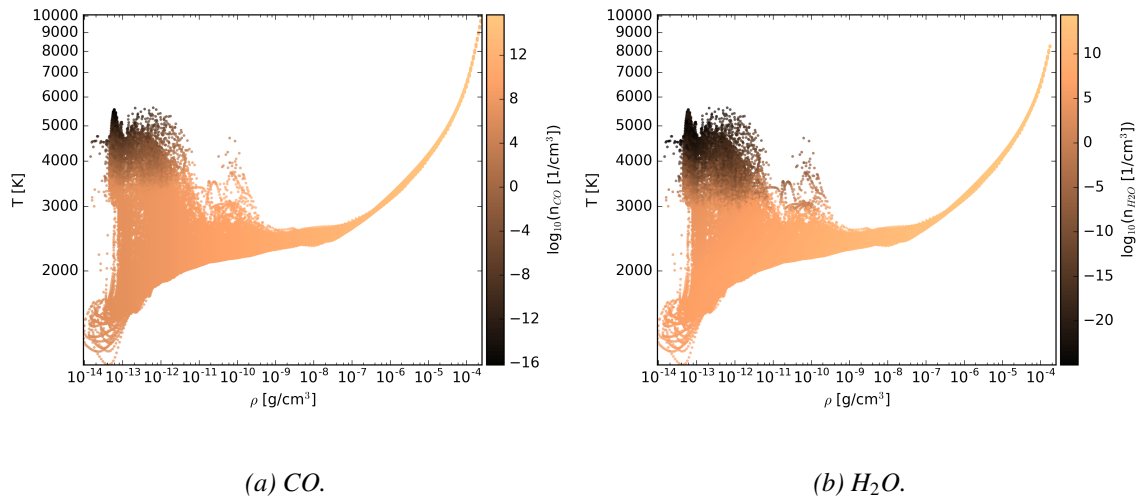


Figure 6.18: Model NL: molecular concentrations, extracted voxel by voxel and colour-coded, plotted against the local temperature and density.

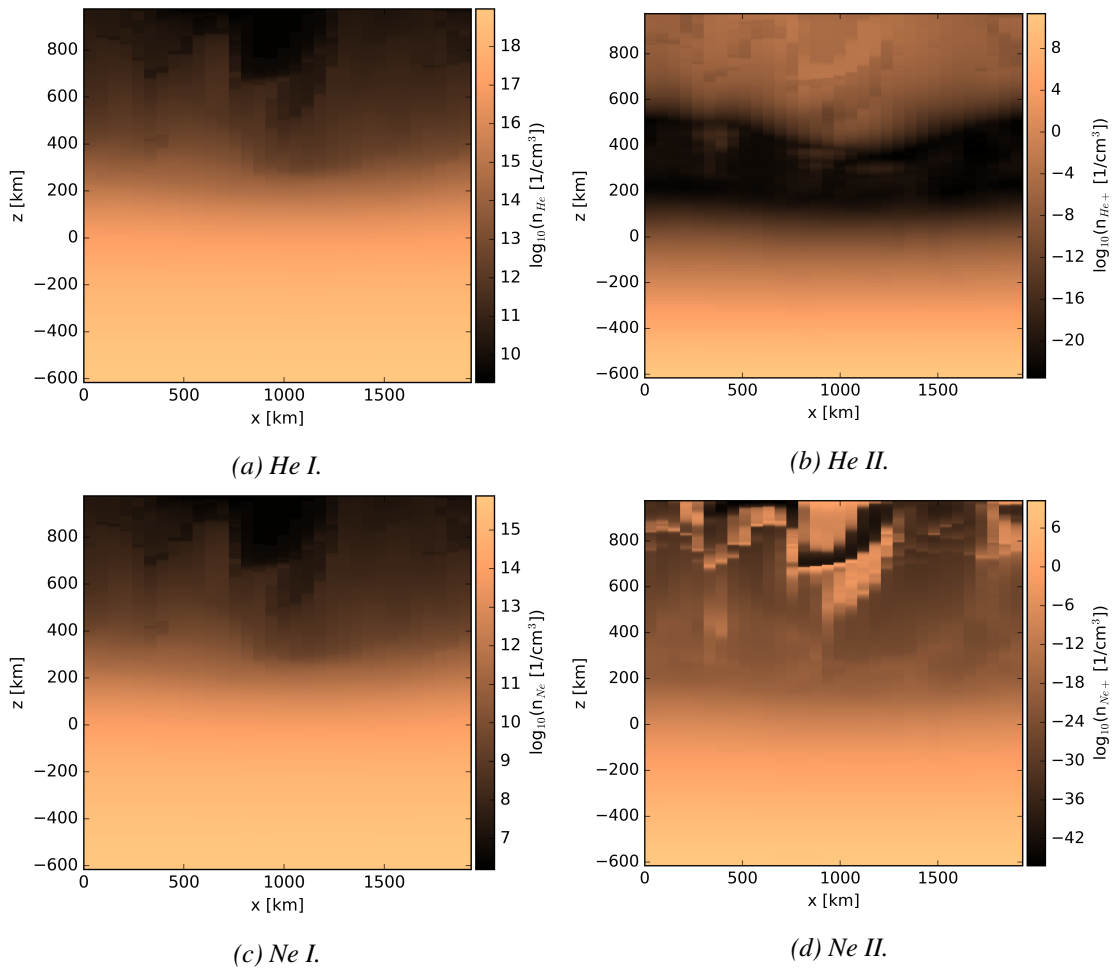


Figure 6.19: Model NL: concentrations for species treated in NLTE or LTE. The vertical slice used here is the same shown in Figs. 4.3a and 5.7.

presented here clearly highlight the importance of including an accurate chemical equilibrium solver for radiative transfer (and MHD) simulations: low temperatures favour the formation of calcium compounds, therefore decreasing the amount of calcium ions in the atmosphere, directly influencing, for example, Ca II spectral features.

## 6.6 Binned vs. non-binned model

Model NS was performed using a reduced set of NLTE species and transitions, lower wavelength resolution, and the original CO<sup>5</sup>BOLD model box, with higher spatial resolution compared to models NN and NL. Considering the outgoing flux spectrum (Fig. 5.10), model NS does not differ substantially from model NL. This is not surprising, because the strongest opacity sources are molecules, which both models include as LTE background opacity sources. The chromosphere appears to be not very active, and reducing the spatial resolution of the grid did not cause any difference: interpolating the grid on a smaller horizontal resolution may reduce the contrast between hot and cold temperatures, but it does not seem to affect the models presented here. The departure coefficients profile (Fig. 5.12) is also similar to that of model NL (Fig. 5.8).

In contrast to model NL, the higher spatial resolution in model NS offers well resolved synthetic flux images (Figs. 5.11). This allows also to observe, for some wavelength points, the *reversed granulation* pattern. We can compare the flux images of two wavelength points from the flux spectrum in the optical range (Fig. 6.21), with the first point characterised by lower flux than the second (in Fig 6.21, the red and cyan markers, respectively). Given the strong molecular opacities at optical wavelengths, the second point represents an “optically thin” window between molecular lines, characterised, therefore, by a lower formation height. We can then visualise the synthetic flux maps for these two wavelength points. The first image, Fig. 6.21a, corresponding to the absorption line, shows the reversed granulation pattern with bright lanes and dark granules, in contrast to the second image, Fig. 6.21b, that shows the standard granulation, i.e. bright granules and dark lanes. This phenomenon has been extensively observed (Evans and Catalano, 1972; Rutten et al., 2004b) and simulated (Wedemeyer et al., 2004; Cheung et al., 2007) for the Sun. Its origin is connected to the thermal structure in the layers right above the photosphere and the convective motions. In the lower photosphere, the bright granules correspond to up-flowing warm gas, while the dark lanes to relatively cooler down-flowing material, thus causing the regular granulation pattern. In the upper photosphere, the over-shooting gas cools down, while the down-flowing gas in the intergranular lanes is mildly shocked and heated up, thus forming the reversed granulation pattern. The absorption line flux image traces gas located higher in the atmosphere, therefore carrying the signature of the reversed granulation.

The results of model NS are indeed promising. If we reduce the number of NLTE transitions by a factor of 100, while keeping the original spatial resolution, the radiative field can be calculated much faster. Ideally, future 3D MHD codes could use a radiative transfer module similar to PHOENIX/3D to compute a more realistic, detailed, multi-level NLTE radiative transport, and replace look-up table algorithms like the *Opacity Binning method*. However, this is nowadays computationally very demanding, and several technical requirements must be considered.

The choice between performing calculations using the binned or the non-binned grid is primarily technical. Model NL (binned grid) required approximately  $10^7$  CPU hours to be computed and the memory occupied is on the order of 6 terabytes. While reserving several terabytes of memory on a large computational facility is nowadays unproblematic, 10 or more million CPU hours require large amounts of allocated time, obtainable only through large projects and collaborations. In comparison, model NS (non-binned grid) required approximately  $10^6$  CPU hours (10 times faster than model NL), while the memory occupied is on the order of 4 terabytes. As mentioned in Section 5.3, for this case, it would be technically very challenging to adopt a finer wavelength grid and/or include more NLTE species.

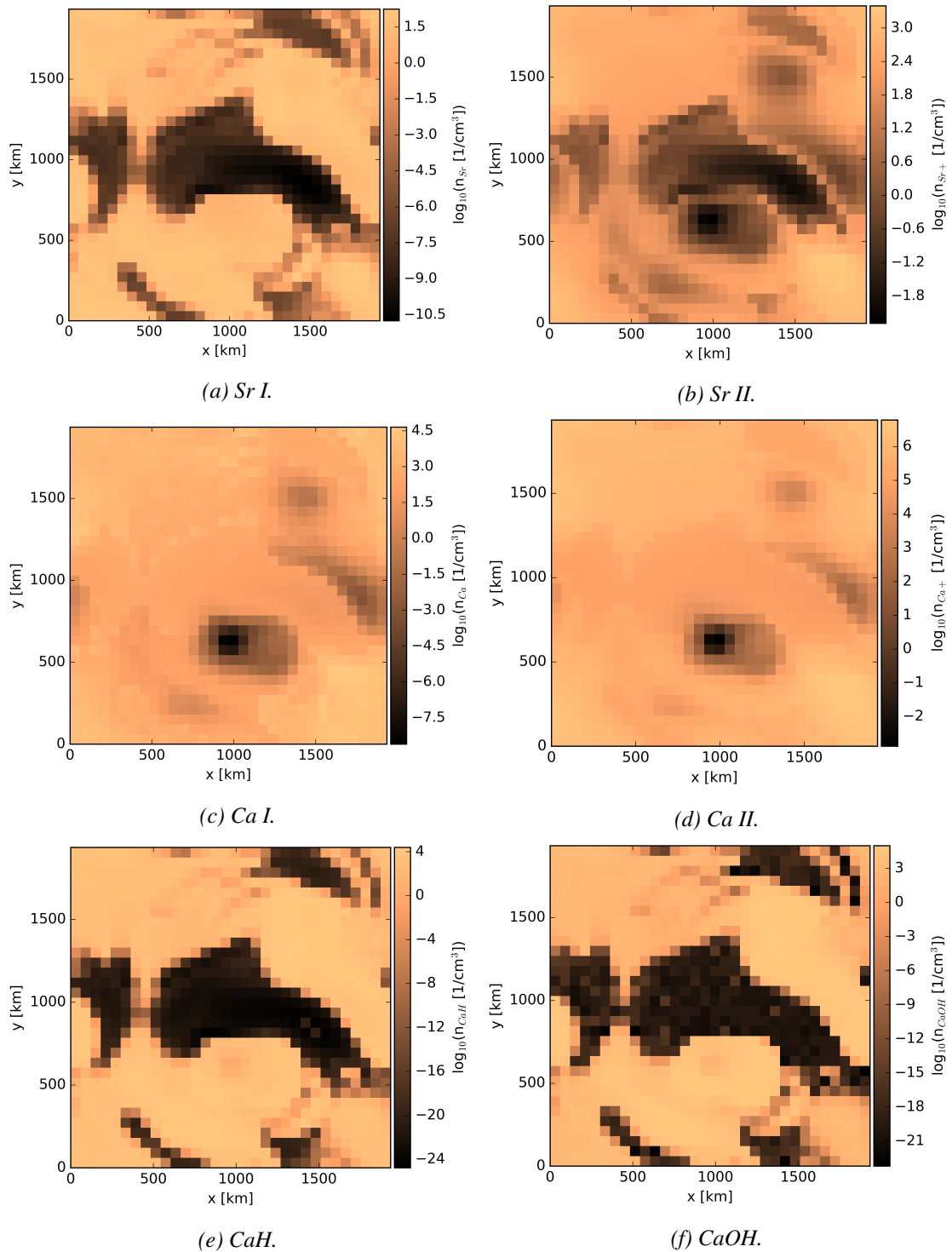
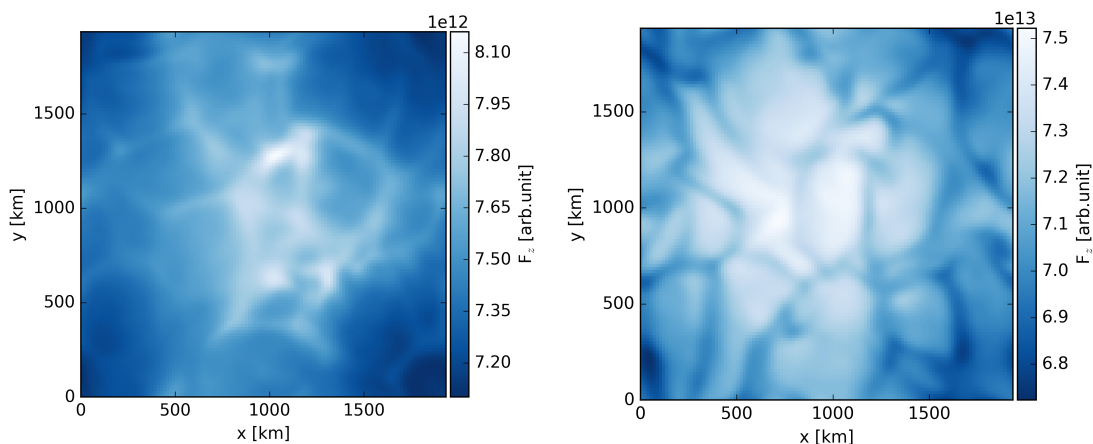
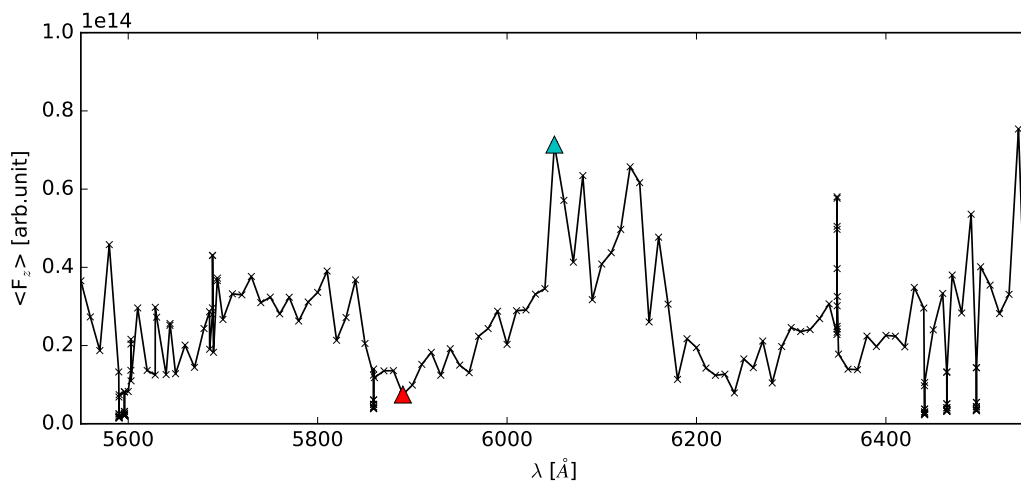


Figure 6.20: Model NL: concentrations for species treated in NLTE or LTE. The images show the outermost layer, like Figs. 4.3d and 6.5.



(a) Flux image at  $5890 \text{ \AA}$ , the wavelength point indicated by the red triangle in the flux spectrum. (b) Flux image at  $6050 \text{ \AA}$ , the wavelength point indicated by the cyan triangle in the flux spectrum.



(c) Flux spectrum in the optical range.

Figure 6.21: Model NS: flux images showing the reversed (a) and regular (b) granulation pattern for the marked wavelength points in the flux spectrum (c). The red triangle marks a wavelength point (at  $5890 \text{ \AA}$ ) with relatively high opacity compared to the one marked by the cyan triangle (at  $6050 \text{ \AA}$ ).

The memory requirements mentioned above are not critical, especially for large computational facilities. On the other hand, successful allocation of a large amount of CPU time is necessary to perform these simulations. These technical obstacles will become trivial with the next generation of supercomputers, if the astrophysical codes are constantly maintained, optimised and extended.

## 6.7 Aliasing artefacts

All the models presented in this work display the aliasing artefacts shown in Section 5.4. The artefacts show up as rings in flux images, but they are actually concentric cones, spreading upwards from a defined location. The “bright” vertical flux spot that appears as the centre of the rings spatially correlates with a hot spot in the input model at  $z = 290 \text{ km}$  (Fig. 6.22a), where the temperature changes by approximately  $2000 \text{ K}$  between two adjacent cells. This causes the local Planck function and consequently the source function to change abruptly, and the integration may fail if the solid angle phase space is not sufficiently covered.

The wavelength dependence of the process is likely due to the opacity. For the flux images, the

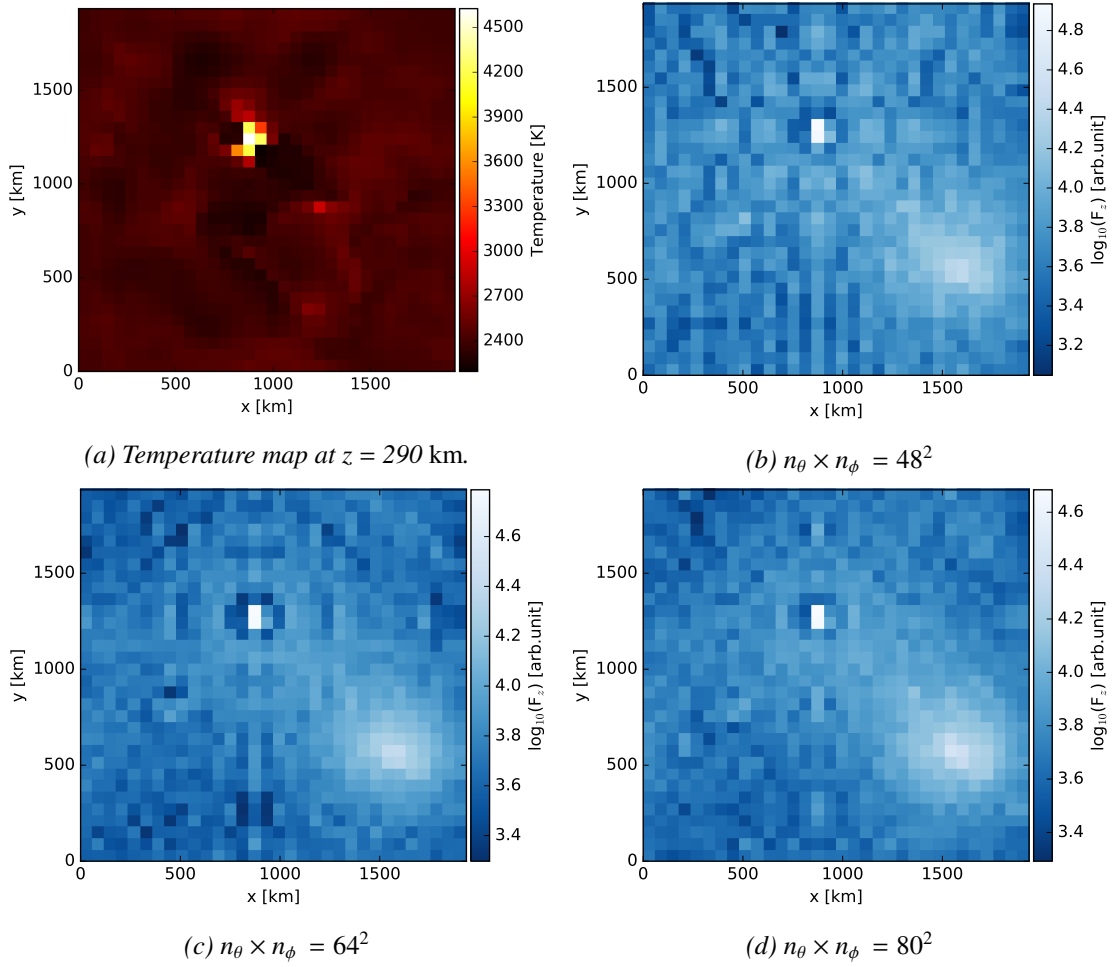


Figure 6.22: Model NL: aliasing artefacts. Panel (a) shows the temperature layer from which the artefacts spread; panels (b), (c), and (d) show the vertical flux image at  $1210 \text{ \AA}$  computed with different angular resolutions.

rings appear preferentially in the continuum and not in lines. The photons originating in the artefact travel up to the outermost layer undisturbed, while UV lines are optically thick. In the first case, the flux image shows the hot spot at  $z = 290$  km, while in the second case we see features resembling the gas temperature from the upper layers. At longer wavelengths, the continuum is formed deeper in the atmosphere, and the temperature discontinuity of the chromosphere does not strongly affect the continuum.

I conducted small tests, including only few UV wavelength points, to investigate the origin of the artefacts and find a possible solution. The angular resolution is likely the most important parameter to set to avoid the artefacts. When increasing the number of solid angles ( $n_\theta$ ,  $n_\phi$ ) from  $48^2$  to  $64^2$  and  $80^2$ , the artefacts are strongly reduced if not eliminated (see Figs. 6.22b, 6.22c, and 6.22d). Changing the wrap-around limiter (Section 4.1.1) does not have any influence. Increasing the angular resolution by a factor of approximately 10 or higher, leads “naturally” to higher accuracy: the formal solution integration is performed on more characteristics, with a finer coverage of the solid angles. This directly affects the computational time needed per iteration due to the larger number of formal solutions to be solved. However, thanks to the domain decomposition, and the large number of processes employable on current super-computers, future PHOENIX/3D models can easily be conducted with a much higher angular resolution and thus avoid the type of artefacts discussed here.



## Chapter 7

# Conclusions and outlook

In this work, I described the results of 3D NLTE PHOENIX/3D simulations of a M-dwarf atmosphere, including photosphere and chromosphere.

The models clearly highlight the necessity of including NLTE treatment for the chromosphere of M-dwarfs. Because of the very low chromospheric plasma densities, the collisional rates do not dominate over the radiative rates, ultimately pushing the radiative field out of LTE conditions. While density and temperature decrease with height, shocks and inhomogeneities create regions with largely different temperatures, higher or lower, compared to the cool surrounding. This heavily influences the flow of photons through the chromosphere and, consequently, the population densities (pushing the departures from LTE to extreme values) and the chemical concentrations.

Flux and intensity images clearly show the interplay between thermal structure and radiative field, and can be used to evaluate the formation heights of spectral lines and continua. I have shown that the processes characterising the M-dwarf atmosphere radiative properties are qualitatively similar to the solar case. For instance, model NS' synthetic images reveal, thanks to the higher spatial resolution, reversed granulation, a phenomenon typically observed on the Sun.

The computed flux spectrum does not dramatically differ from an observed spectrum of AD Leo (the reference star for the CO<sup>5</sup>BOLD M-dwarf models grid from Wedemeyer et al.). The absence of chromospheric emission lines, such as Ca II H&K or H $\alpha$ , suggests that the atmosphere is characterised by a low level of activity. This is not surprising: the input model is a snapshot from the CO<sup>5</sup>BOLD simulation with the lowest initial magnetic field strength. More PHOENIX/3D models are necessary to investigate the influence of magnetic activity, i.e. the initial magnetic field strength and configuration for the CO<sup>5</sup>BOLD models, on the spectral properties of the atmosphere.

The comparison between median and mean vertical profiles for different quantities gives interesting insights about the structure of the atmosphere, such as degree of ionisation and molecular concentrations. For instance, I demonstrated that the high values for the mean concentrations of neutral and ionised carbon are due to few cells featuring high temperatures, where CO dissociation is greatly enhanced. On the other hand, the mean and median profiles for CO reveal rather large concentrations, suggesting that most of the carbon in the photosphere and chromosphere is indeed trapped in molecules, in agreement with observations. These considerations may be very significant when comparing 3D models to 1D column-weighted observations, such as stellar spectra.

I have shown that nowadays, with modern super-computers, it is possible to compute 3D atmosphere models that include a large number of NLTE species, LTE background opacities, a high wavelength resolution, and highly resolved spatial grid. We can use this kind of radiative transfer simulations to compute synthetic data, e.g. spectrum, line profiles, intensity images, etc., to compare to observations, or estimate the stellar radiative output in wavelength areas not easily accessible with instruments. The limitations for this kind of work for PHOENIX/3D are mostly technical.

Memory requirements are currently critical, affecting the choice for spatial and wavelength resolutions. It is impossible to save the intermediate data for each iteration, and, for the “last”

iteration, unfortunately not all the relevant output data can be stored and moved to local drives. It is, therefore, of primary importance to regularly check the progress of the convergence of a model iteration after iteration. This task may be easier in the future with larger memory drives and an automated working-pipeline.

As briefly mentioned in Section 2.3, 3D radiative transfer simulations require a large amount of computational time. Specifically, for model NL, approximately 10 millions CPU hours were necessary. These simulations are possible only thanks to PHOENIX/3D high degree of parallelisation, and the generous time allocated at various computational facilities. Optimisation of the code is fundamental to reduce the computational costs, primarily in terms of CPU time requirements.

Angular resolution in 3D models has to be properly chosen to avoid artefacts. A low angular resolution works for uniform atmospheres, but may produce physically incorrect results (inaccurate integration over the solid angles) when giving complex atmospheres, like CO<sup>5</sup>BOLD models, as input to PHOENIX/3D. Small and abrupt changes in the model thermal structure must be resolved properly, i.e. the sampling has to be sufficient to provide an accurate solution. Increasing the angular resolution by a factor of 10 will affect the computational time needed per iteration, specifically the formal solution step, but improve the accuracy. Also in this case, code optimisation and increased computing power can effectively overcome this problem.

The models discussed here have treated only the most abundant species in NLTE. Including higher ionisation stages and more species is mainly a technical complication, which has to be addressed in the future to properly evaluate the relevance of, for example, abundant low ionisation metals like Fe I-II.

The assumption of complete frequency redistribution is greatly simplifying the radiative transfer. However, 1D models have shown the need to include partial frequency redistribution to consistently model line profiles, directly influencing levels' excitation, ionisation, free electron density, and other properties. The implementation of partial frequency redistribution in PHOENIX/3D is currently under development.

CO<sup>5</sup>BOLD MHD models provide as output also the velocity and magnetic field, which were not employed in the PHOENIX/3D simulations presented in this work. Seelmann et al. (2010) describe the treatment of non-relativistic arbitrary velocity fields in the Eulerian frame, for a two-level-atom, in PHOENIX/3D. The further extension to NLTE multi-level opacity calculation is under development. PHOENIX does not currently include any magnetic field treatment. The influence of the magnetic field on the thermal properties of the chromosphere is properly addressed by CO<sup>5</sup>BOLD, thus indirectly included in the PHOENIX/3D models. Moreover, the magnetic field influences locally the radiative properties of the gas, e.g by the *Zeeman effect* responsible for line splitting. The inclusion of arbitrary magnetic fields and the Zeeman effect in PHOENIX/3D may help to investigate the interplay between magnetic structures and radiative transfer in NLTE conditions.

Ideal MHD simulations of the chromosphere conducted with CO<sup>5</sup>BOLD represent the latest and best achievement in a consistent modelling of the upper atmosphere of M-dwarfs. These simulations deserve undoubtedly further development to model more different stellar environments with higher accuracy, and to relax some of the strong physical assumptions, e.g. high gas collisionality, LTE radiation transport, etc. The adoption of a NLTE radiative transfer module for 3D MHD would be a major advancement but, nowadays, computationally rather expensive. Plasma codes adopting a multi-fluid approach, solving separately the equations for different components (ions, electrons and neutrals), are nowadays becoming more popular (Khomenko et al., 2014). This kind of simulations treats partial ionisation more accurately than classical MHD works, thus being very promising for the modelling of cool stars atmospheres.

1D stellar atmosphere models usually adopt strong simplifying assumptions. 3D simulations are necessary to thoroughly test the theory and to better reproduce the observations. An accurate modelling of the chromosphere also requires multi-dimensional simulations, including a detailed treatment of the radiative transfer and allowing for departures from LTE conditions. 3D NLTE

radiative transfer frameworks, such as PHOENIX/3D, are necessary to address these problems. The simulations presented in this thesis show how similar M-dwarf chromospheric radiative processes are in comparison to the solar case, with an accurate multi-level multi-species opacity treatment being crucial to correctly evaluate the atmosphere properties. 3D synthetic observables provide an important tool to evaluate how much information we can extract from spatially averaged stellar observations. The analysis conducted in this work represents a starting point to investigate M-dwarf properties with 3D NLTE PHOENIX/3D models.



# Bibliography

- F. Allard, P. H. Hauschildt, D. R. Alexander, and S. Starrfield. Model Atmospheres of Very Low Mass Stars and Brown Dwarfs. *Annual Review of Astronomy & Astrophysics*, 35:137–177, 1997. doi: 10.1146/annurev.astro.35.1.137.
- C.W. Allen and A.N. Cox. *Allen's Astrophysical Quantities*. Springer, 2000. ISBN 9780387987460. URL <https://books.google.de/books?id=w8PK2XFLLH8C>.
- F. J. Alonso-Floriano, J. C. Morales, J. A. Caballero, et al. CARMENES input catalogue of M dwarfs. I. Low-resolution spectroscopy with CAFOS. *Astronomy and Astrophysics*, 577:A128, May 2015. doi: 10.1051/0004-6361/201525803.
- L. S. Anderson and R. G. Athay. Chromospheric and coronal heating. *Astrophysical Journal*, 336: 1089–1091, January 1989. doi: 10.1086/167078.
- M. Asplund. New Light on Stellar Abundance Analyses: Departures from LTE and Homogeneity. *Annual Review of Astronomy & Astrophysics*, 43:481–530, September 2005. doi: 10.1146/annurev.astro.42.053102.134001.
- M. Asplund, N. Grevesse, A. J. Sauval, and P. Scott. The Chemical Composition of the Sun. *Annual Review of Astronomy & Astrophysics*, 47:481–522, September 2009. doi: 10.1146/annurev.astro.46.060407.145222.
- T. R. Ayres. Chromospheric scaling laws, width-luminosity correlations, and the Wilson-Bappu effect. *Astrophysical Journal*, 228:509–520, March 1979. doi: 10.1086/156873.
- T. R. Ayres and L. Testerman. Fourier Transform Spectrometer observations of solar carbon monoxide. I - The fundamental and first overtone bands in the quiet sun. *Astrophysical Journal*, 245:1124–1140, May 1981. doi: 10.1086/158888.
- T. R. Ayres, R. A. Shine, and J. L. Linsky. A possible width-luminosity correlation of the CA II K1 and MG II k1 features. *Astrophysical Journal Letters*, 195:L121–L124, February 1975. doi: 10.1086/181724.
- S. L. Baliunas, R. A. Donahue, W. Soon, and G. W. Henry. Activity Cycles in Lower Main Sequence and POST Main Sequence Stars: The HK Project. In R. A. Donahue and J. A. Bookbinder, editors, *Cool Stars, Stellar Systems, and the Sun*, volume 154 of *Astronomical Society of the Pacific Conference Series*, page 153, 1998.
- B. Beeck, R. H. Cameron, A. Reiners, and M. Schüssler. Three-dimensional simulations of near-surface convection in main-sequence stars. II. Properties of granulation and spectral lines. *Astronomy and Astrophysics*, 558:A49, October 2013. doi: 10.1051/0004-6361/201321345.
- A. Berkner. *3D Super Level non-LTE Radiative Transfer for Molecules*. PhD thesis, Universität Hamburg, 2015. URL <http://ediss.sub.uni-hamburg.de/volltexte/2015/7186>.

- J. J. Bochanski, S. L. Hawley, K. R. Covey, et al. The Luminosity and Mass Functions of Low-mass Stars in the Galactic Disk. II. The Field. *Astronomical Journal*, 139:2679-2699, June 2010. doi: 10.1088/0004-6256/139/6/2679.
- E. Böhm-Vitense. Über die Wasserstoffkonvektionszone in Sternen verschiedener Effektivtemperaturen und Leuchtkräfte. Mit 5 Textabbildungen. *Zeitschrift für Astrophysik*, 46:108, 1958.
- C. J. Cannon. Angular quadrature perturbations in radiative transfer theory. *Journal of Quantitative Spectroscopy and Radiative Transfer*, 13:627–633, 1973. doi: 10.1016/0022-4073(73)90021-6.
- M. Carlsson and R. F. Stein. Non-LTE radiating acoustic shocks and CA II K2V bright points. *Astrophysical Journal Letters*, 397:L59–L62, September 1992. doi: 10.1086/186544.
- M. Carlsson and R. F. Stein. Does a nonmagnetic solar chromosphere exist? *Astrophysical Journal Letters*, 440:L29–L32, February 1995. doi: 10.1086/187753.
- P. Charbonneau. Solar Dynamo Theory. *Annual Review of Astronomy & Astrophysics*, 52:251–290, August 2014. doi: 10.1146/annurev-astro-081913-040012.
- M. C. M. Cheung, M. Schüssler, and F. Moreno-Insertis. The origin of the reversed granulation in the solar photosphere. *Astronomy and Astrophysics*, 461:1163–1171, January 2007. doi: 10.1051/0004-6361:20066390.
- L. E. Cram and M. S. Giampapa. Formation of chromospheric lines in cool dwarf stars. *Astrophysical Journal*, 323:316–324, December 1987. doi: 10.1086/165829.
- B. De Pontieu, R. Erdélyi, and A. G. de Wijn. Intensity Oscillations in the Upper Transition Region above Active Region Plage. *Astrophysical Journal Letters*, 595:L63–L66, September 2003. doi: 10.1086/378843.
- B. De Pontieu, A. M. Title, J. R. Lemen, et al. The interface region imaging spectrograph (iris). *Solar Physics*, 289(7):2733–2779, 2014. ISSN 1573-093X. doi: 10.1007/s11207-014-0485-y. URL <http://dx.doi.org/10.1007/s11207-014-0485-y>.
- V. Domingo, B. Fleck, and A. I. Poland. The SOHO Mission: an Overview. *Solar Physics*, 162:1–37, December 1995. doi: 10.1007/BF00733425.
- A. Driesman, S. Hynes, and G. Cancro. The stereo observatory. *Space Science Reviews*, 136(1): 17–44, 2008. ISSN 1572-9672. doi: 10.1007/s11214-007-9286-z. URL <http://dx.doi.org/10.1007/s11214-007-9286-z>.
- G. Eberhard and K. Schwarzschild. On the reversal of the calcium lines H and K in stellar spectra. *Astrophysical Journal*, 38, October 1913. doi: 10.1086/142037.
- J. W. Evans and C. P. Catalano. Observed Oddities in the Lines H, K, b and Hbeta. *Solar Physics*, 27: 299–302, December 1972. doi: 10.1007/BF00153101.
- A. Falchi and P. J. D. Mauas. Building reliable models of M dwarf chromospheres: the impact of the usual assumptions. *Astronomy and Astrophysics*, 336:281–289, August 1998.
- J. M. Fontenla, E. H. Avrett, and R. Loeser. Energy balance in the solar transition region. I - Hydrostatic thermal models with ambipolar diffusion. *Astrophysical Journal*, 355:700–718, June 1990. doi: 10.1086/168803.
- J. M. Fontenla, E. H. Avrett, and R. Loeser. Energy balance in the solar transition region. II - Effects of pressure and energy input on hydrostatic models. *Astrophysical Journal*, 377:712–725, August 1991. doi: 10.1086/170399.

- J. M. Fontenla, E. H. Avrett, and R. Loeser. Energy balance in the solar transition region. III - Helium emission in hydrostatic, constant-abundance models with diffusion. *Astrophysical Journal*, 406: 319–345, March 1993. doi: 10.1086/172443.
- J. M. Fontenla, J. L. Linsky, J. Witbrod, et al. Semi-empirical Modeling of the Photosphere, Chromosphere, Transition Region, and Corona of the M-dwarf Host Star GJ 832. *ArXiv e-prints*, August 2016.
- B. Freytag, F. Allard, H.-G. Ludwig, D. Homeier, and M. Steffen. The role of convection, overshoot, and gravity waves for the transport of dust in M dwarf and brown dwarf atmospheres. *Astronomy and Astrophysics*, 513:A19, April 2010. doi: 10.1051/0004-6361/200913354.
- B. Freytag, M. Steffen, H.-G. Ludwig, et al. Simulations of stellar convection with CO5BOLD. *Journal of Computational Physics*, 231:919–959, February 2012. doi: 10.1016/j.jcp.2011.09.026.
- B. Fuhrmeister, J. H. M. M. Schmitt, and P. H. Hauschildt. PHOENIX model chromospheres of mid- to late-type M dwarfs. *Astronomy and Astrophysics*, 439:1137–1148, September 2005. doi: 10.1051/0004-6361:20042338.
- B. Fuhrmeister, C. I. Short, and P. H. Hauschildt. Influence of NLTE calculations on the hydrogen lines in chromospheric models. *Astronomy and Astrophysics*, 452:1083–1088, June 2006. doi: 10.1051/0004-6361:20053787.
- B. Fuhrmeister, J. H. M. M. Schmitt, and P. H. Hauschildt. Multi-wavelength observations of a giant flare on CN Leonis. II. Chromospheric modelling with PHOENIX. *Astronomy and Astrophysics*, 511:A83, February 2010. doi: 10.1051/0004-6361/200810224.
- M. S. Giampapa and J. Liebert. High-resolution H-alpha observations of M dwarf stars Implications for stellar dynamo models and stellar kinematic properties at faint magnitudes. *Astrophysical Journal*, 305:784–794, June 1986. doi: 10.1086/164291.
- M. S. Giampapa, S. P. Worden, and J. L. Linsky. Stellar model chromospheres. XIII - M dwarf stars. *Astrophysical Journal*, 258:740–760, July 1982. doi: 10.1086/160122.
- O. Gingerich and C. de Jager. The Bilderberg Model of the Photosphere and Low Chromosphere. *Solar Physics*, 3:5–25, January 1968. doi: 10.1007/BF00154238.
- O. Gingerich, R. W. Noyes, W. Kalkofen, and Y. Cuny. The Harvard-Smithsonian reference atmosphere. *Solar Physics*, 18:347–365, July 1971. doi: 10.1007/BF00149057.
- D. Goorvitch. Infrared CO line for the X 1 Sigma(+) state. *Astrophysical Journal Supplement Series*, 95:535–552, December 1994. doi: 10.1086/192110.
- J. C. Hall. Stellar chromospheric activity. *Living Reviews in Solar Physics*, 5(2), 2008. doi: 10.1007/lrsp-2008-2. URL <http://www.livingreviews.org/lrsp-2008-2>.
- P. H. Hauschildt. A fast operator perturbation method for the solution of the special relativistic equation of radiative transfer in spherical symmetry. *Journal of Quantitative Spectroscopy & Radiative Transfer*, 47:433–453, June 1992. doi: 10.1016/0022-4073(92)90105-D.
- P. H. Hauschildt. Multi-level non-LTE radiative transfer in expanding shells. *Journal of Quantitative Spectroscopy & Radiative Transfer*, 50:301–318, September 1993. doi: 10.1016/0022-4073(93)90080-2.

- P. H. Hauschildt and E. Baron. A 3D radiative transfer framework. I. Non-local operator splitting and continuum scattering problems. *Astronomy and Astrophysics*, 451:273–284, May 2006. doi: 10.1051/0004-6361:20053846.
- P. H. Hauschildt and E. Baron. A 3D radiative transfer framework. III. Periodic boundary conditions. *Astronomy and Astrophysics*, 490:873–877, November 2008. doi: 10.1051/0004-6361:200810239.
- P. H. Hauschildt and E. Baron. A 3D radiative transfer framework. VI. PHOENIX/3D example applications. *Astronomy and Astrophysics*, 509:A36, January 2010. doi: 10.1051/0004-6361/200913064.
- P. H. Hauschildt and E. Baron. A 3D radiative transfer framework. XI. Multi-level NLTE. *Astronomy and Astrophysics*, 566:A89, June 2014. doi: 10.1051/0004-6361/201423574.
- P. H. Hauschildt, E. Baron, and F. Allard. Parallel Implementation of the PHOENIX Generalized Stellar Atmosphere Program. *Astrophysical Journal*, 483:390–398, July 1997.
- P. H. Hauschildt, F. Allard, and E. Baron. The NextGen Model Atmosphere Grid for 3000 Teff 10,000 K. *Astrophysical Journal*, 512:377–385, February 1999. doi: 10.1086/306745.
- J. R. W. Heintze, H. Hubenet, and C. de Jager. A reference model of the solar photosphere and low chromosphere. *Bulletin of the Astronomical Institutes of the Netherlands*, 17:442, May 1964.
- P. Heinzel, I. Dorotovič, and R. J. Rutten, editors. *The Physics of Chromospheric Plasmas*, volume 368 of *Astronomical Society of the Pacific Conference Series*, May 2007.
- H. Holweger. Ein empirisches Modell der Sonnenatmosphäre mit lokalem thermodynamischem Gleichgewicht. *Zeitschrift für Astrophysik*, 65:365, 1967.
- H. Holweger and E. A. Mueller. The photospheric barium spectrum - Solar abundance and collision broadening of BA II lines by hydrogen. *Solar Physics*, 39:19–30, November 1974. doi: 10.1007/BF00154968.
- I. Hubeny and D. Mihalas. *Theory of stellar atmospheres: an introduction to astrophysical non-equilibrium quantitative spectroscopic analysis*. Princeton series in astrophysics. Princeton University Press, Princeton, NJ, 2015.
- Y. Itikawa, editor. *Interactions of Photons and Electrons with Molecules*, volume 17C of *Landolt-Börnstein - Group I Elementary Particles, Nuclei and Atoms*. Springer Berlin Heidelberg, 2003. doi: 10.1007/b83711.
- G. H. Jacoby, D. A. Hunter, and C. A. Christian. A library of stellar spectra. *Astrophysical Journal Supplement Series*, 56:257–281, October 1984. doi: 10.1086/190983.
- A. H. Joy and H. A. Abt. Spectral Types of M Dwarf Stars. *Astrophysical Journal Supplement Series*, 28:1, November 1974. doi: 10.1086/190307.
- R. Kandel. Contribution à l'étude des atmosphères des étoiles naines froides. II. Les chromosphères des étoiles naines froides. *Annales d'Astrophysique*, 30:999, February 1967.
- E. Khomenko, M. Collados, A. Díaz, and N. Vitas. Fluid description of multi-component solar partially ionized plasma. *Physics of Plasmas*, 21(9):092901, September 2014. doi: 10.1063/1.4894106.
- J. D. Kirkpatrick, T. J. Henry, and D. W. McCarthy, Jr. A standard stellar spectral sequence in the red/near-infrared - Classes K5 to M9. *Astrophysical Journal Supplement Series*, 77:417–440, November 1991. doi: 10.1086/191611.

- J. A. Klimchuk. Key aspects of coronal heating. *Philosophical Transactions of the Royal Society of London Series A*, 373:20140256–20140256, April 2015. doi: 10.1098/rsta.2014.0256.
- Y. Kondo, W. Wamsteker, A. Boggess, et al. *Exploring the Universe with the IUE Satellite*. Astrophysics and Space Science Library. Springer Netherlands, 2013. ISBN 9789401081733. URL <https://books.google.de/books?id=66IzngEACAAJ>.
- R. B. Leighton. Observations of Solar Magnetic Fields in Plage Regions. *Astrophysical Journal*, 130: 366, September 1959. doi: 10.1086/146727.
- J. L. Linsky. Stellar chromospheres. *Annual Review of Astronomy & Astrophysics*, 18:439–488, 1980. doi: 10.1146/annurev.aa.18.090180.002255.
- R. Liseau, W. Vlemmings, A. Bayo, et al. ALMA observations of  $\alpha$  Centauri. First detection of main-sequence stars at 3 mm wavelength. *Astronomy and Astrophysics*, 573:L4, January 2015. doi: 10.1051/0004-6361/201425189.
- J. N. Lockyer. Spectroscopic Observation of the Sun, No. II. *Proceedings of the Royal Society of London Series I*, 17:131–132, 1868.
- H.-G. Ludwig, F. Allard, and P. H. Hauschildt. Numerical simulations of surface convection in a late M-dwarf. *Astronomy and Astrophysics*, 395:99–115, November 2002. doi: 10.1051/0004-6361:20021153.
- H.-G. Ludwig, F. Allard, and P. H. Hauschildt. Energy transport, overshoot, and mixing in the atmospheres of M-type main- and pre-main-sequence objects. *Astronomy and Astrophysics*, 459: 599–612, November 2006. doi: 10.1051/0004-6361:20054010.
- P. J. D. Mauas and A. Falchi. Atmospheric models of flare stars: The quiescent state of AD Leonis. *Astronomy and Astrophysics*, 281:129–138, January 1994.
- P. J. D. Mauas and A. Falchi. Atmospheric models of flare stars: the flaring state of AD Leonis. *Astronomy and Astrophysics*, 310:245–258, June 1996.
- F. Middelkoop and C. Zwaan. Magnetic structure in cool stars. I - The CA II H and K emission from giants. *Astronomy and Astrophysics*, 101:26–32, August 1981.
- D. Mihalas. *Stellar atmospheres /2nd edition/*. 1978.
- A. Nordlund. Numerical simulations of the solar granulation. I - Basic equations and methods. *Astronomy and Astrophysics*, 107:1–10, March 1982.
- R. W. Noyes, L. W. Hartmann, S. L. Baliunas, D. K. Duncan, and A. H. Vaughan. Rotation, convection, and magnetic activity in lower main-sequence stars. *Astrophysical Journal*, 279:763–777, April 1984. doi: 10.1086/161945.
- F. Ochsenbein, P. Bauer, and J. Marcout. The VizieR database of astronomical catalogues. *Astronomy and Astrophysics Supplement*, 143:23–32, April 2000. doi: 10.1051/aas:2000169.
- G. L. Olson, L. H. Auer, and J. R. Buchler. A rapidly convergent iterative solution of the non-LTE line radiation transfer problem. *Journal of Quantitative Spectroscopy and Radiative Transfer*, 35: 431–442, June 1986. doi: 10.1016/0022-4073(86)90030-0.
- T. M. D. Pereira, M. Asplund, R. Collet, et al. How realistic are solar model atmospheres? *Astronomy and Astrophysics*, 554:A118, June 2013. doi: 10.1051/0004-6361/201321227.

- W. D. Pesnell, B. J. Thompson, and P. C. Chamberlin. The Solar Dynamics Observatory (SDO). *Solar Physics*, 275:3–15, January 2012. doi: 10.1007/s11207-011-9841-3.
- J. T. Rayner, M. C. Cushing, and W. D. Vacca. The Infrared Telescope Facility (IRTF) Spectral Library: Cool Stars. *Astrophysical Journal Supplement Series*, 185:289–432, December 2009. doi: 10.1088/0067-0049/185/2/289.
- I. N. Reid and S. L. Hawley. *New light on dark stars : red dwarfs, low-mass stars, brown dwarfs*. 2005. doi: 10.1007/3-540-27610-6.
- I. N. Reid, J. D. Kirkpatrick, J. E. Gizis, et al. Four Nearby L Dwarfs. *Astronomical Journal*, 119: 369–377, January 2000. doi: 10.1086/301177.
- D. Reimers. A study of Ca II K<sub>2</sub> and H<sub>alpha</sub> line widths in late type stars. *Astronomy and Astrophysics*, 24:79–87, April 1973.
- A. Reiners. Observations of Cool-Star Magnetic Fields. *Living Reviews in Solar Physics*, 9, February 2012. doi: 10.12942/lrsp-2012-1.
- R. J. Rutten. *Radiative Transfer in Stellar Atmospheres*. May 2003. URL <http://esoads.eso.org/abs/2003rtsa.book.....R>.
- R. J. Rutten. Observing the Solar Chromosphere. In P. Heinzel, I. Dorotovič, and R. J. Rutten, editors, *The Physics of Chromospheric Plasmas*, volume 368 of *Astronomical Society of the Pacific Conference Series*, page Heinzel, May 2007.
- R. J. Rutten, F. C. M. Bettonvil, R. H. Hammerschlag, et al. The Dutch Open Telescope on La Palma. In A. V. Stepanov, E. E. Benevolenskaya, and A. G. Kosovichev, editors, *Multi-Wavelength Investigations of Solar Activity*, volume 223 of *IAU Symposium*, pages 597–604, 2004a. doi: 10.1017/S1743921304006957.
- R. J. Rutten, A. G. de Wijn, and P. Sütterlin. DOT tomography of the solar atmosphere. II. Reversed granulation in Ca II H. *Astronomy and Astrophysics*, 416:333–340, March 2004b. doi: 10.1051/0004-6361:20035636.
- G. B. Rybicki and D. G. Hummer. An accelerated lambda iteration method for multilevel radiative transfer. I - Non-overlapping lines with background continuum. *Astronomy and Astrophysics*, 245: 171–181, May 1991.
- S. H. Saar and J. L. Linsky. The photospheric magnetic field of the dM3.5e flare star AD Leonis. *Astrophysical Journal Letters*, 299:L47–L50, December 1985. doi: 10.1086/184578.
- G. B. Scharmer, K. Bjelksjo, T. K. Korhonen, B. Lindberg, and B. Petterson. The 1-meter Swedish solar telescope. In S. L. Keil and S. V. Avakyan, editors, *Innovative Telescopes and Instrumentation for Solar Astrophysics*, volume 4853 of *Proceedings of the SPIE*, pages 341–350, February 2003.
- E. Schatzman. A theory of the role of magnetic activity during star formation. *Annales d'Astrophysique*, 25:18, February 1962.
- W. Schmidt, O. von der Lühe, R. Volkmer, et al. The GREGOR Solar Telescope on Tenerife. In T. R. Rimmele, A. Tritschler, F. Wöger, et al., editors, *Second ATST-EAST Meeting: Magnetic Fields from the Photosphere to the Corona.*, volume 463 of *Astronomical Society of the Pacific Conference Series*, page 365, December 2012.

- C. J. Schrijver. Magnetic structure in cool stars. XI - Relations between radiative fluxes measuring stellar activity, and evidence for two components in stellar chromospheres. *Astronomy and Astrophysics*, 172:111–123, January 1987.
- A. M. Seelmann. *3D radiative transfer in arbitrary velocity fields: The Eulerian approach*. PhD thesis, Universität Hamburg, Von-Melle-Park 3, 20146 Hamburg, 2011. URL <http://ediss.sub.uni-hamburg.de/volltexte/2011/5148>.
- A. M. Seelmann, P. H. Hauschildt, and E. Baron. A 3D radiative transfer framework . VII. Arbitrary velocity fields in the Eulerian frame. *Astronomy and Astrophysics*, 522:A102, November 2010. doi: 10.1051/0004-6361/201014278.
- T. Simon and W. Landsman. The onset of chromospheric activity among the A and F stars. *Astrophysical Journal*, 380:200–207, October 1991. doi: 10.1086/170574.
- R. Skartlien, R. F. Stein, and Å. Nordlund. Excitation of Chromospheric Wave Transients by Collapsing Granules. *Astrophysical Journal*, 541:468–488, September 2000. doi: 10.1086/309414.
- W. R. Smith and R. W. Missen. *Chemical reaction equilibrium analysis: theory and algorithms*. Wiley series in chemical engineering. Wiley, 1982. ISBN 9780471093473.
- S. K. Solanki, W. Livingston, and T. Ayres. New Light on the Heart of Darkness of the Solar Chromosphere. *Science*, 263:64–66, January 1994. doi: 10.1126/science.263.5143.64.
- R. F. Stein and Å. Nordlund. Simulations of Solar Granulation. I. General Properties. *Astrophysical Journal*, 499:914–933, May 1998.
- S. Tsuneta, K. Ichimoto, Y. Katsukawa, et al. The Solar Optical Telescope for the Hinode Mission: An Overview. *Solar Physics*, 249:167–196, June 2008. doi: 10.1007/s11207-008-9174-z.
- A. Unsöld. *Physik der Sternatmosphären: mit besonderer Berücksichtigung der Sonne*. Verlag von Julius Springer, 1938. URL <https://books.google.de/books?id=j8TPAAAAMAAJ>.
- D. R. van Rossum. *Massive NLTE models for X-ray novae with PHOENIX*. PhD thesis, Universität Hamburg, Von-Melle-Park 3, 20146 Hamburg, 2009. URL <http://ediss.sub.uni-hamburg.de/volltexte/2010/4571>.
- J. E. Vernazza, E. H. Avrett, and R. Loeser. Structure of the Solar Chromosphere. Basic Computations and Summary of the Results. *Astrophysical Journal*, 184:605–632, September 1973. doi: 10.1086/152353.
- J. E. Vernazza, E. H. Avrett, and R. Loeser. Structure of the solar chromosphere. II - The underlying photosphere and temperature-minimum region. *Astrophysical Journal Supplement Series*, 30:1–60, January 1976. doi: 10.1086/190356.
- J. E. Vernazza, E. H. Avrett, and R. Loeser. Structure of the solar chromosphere. III - Models of the EUV brightness components of the quiet-sun. *Astrophysical Journal Supplement Series*, 45: 635–725, April 1981. doi: 10.1086/190731.
- A. Vögler, S. Shelyag, M. Schüssler, et al. Simulations of magneto-convection in the solar photosphere. Equations, methods, and results of the MURaM code. *Astronomy and Astrophysics*, 429: 335–351, January 2005. doi: 10.1051/0004-6361:20041507.
- S. Wedemeyer. New Eyes on the Sun - Solar Science with ALMA. *The Messenger*, 163:15–20, March 2016.

- S. Wedemeyer and H.-G. Ludwig. Synthetic activity indicators for M-type dwarf stars. *ArXiv e-prints*, November 2015.
- S. Wedemeyer, B. Freytag, M. Steffen, H.-G. Ludwig, and H. Holweger. Numerical simulation of the three-dimensional structure and dynamics of the non-magnetic solar chromosphere. *Astronomy and Astrophysics*, 414:1121–1137, February 2004. doi: 10.1051/0004-6361:20031682.
- S. Wedemeyer, H.-G. Ludwig, and O. Steiner. Three-dimensional magnetohydrodynamic simulations of M-dwarf chromospheres. *Astronomische Nachrichten*, 334:137–140, February 2013. doi: 10.1002/asna.201211741.
- S. Wedemeyer, T. Bastian, R. Brajša, et al. Solar Science with the Atacama Large Millimeter/Submillimeter Array - A New View of Our Sun. *Space Science Reviews*, 200:1–73, April 2016. doi: 10.1007/s11214-015-0229-9.
- S. Wedemeyer-Böhm and L. Rouppe van der Voort. On the continuum intensity distribution of the solar photosphere. *Astronomy and Astrophysics*, 503:225–239, August 2009a. doi: 10.1051/0004-6361/200911983.
- S. Wedemeyer-Böhm and L. Rouppe van der Voort. Small-scale swirl events in the quiet Sun chromosphere. *Astronomy and Astrophysics*, 507:L9–L12, November 2009b. doi: 10.1051/0004-6361/200913380.
- S. Wedemeyer-Böhm and M. Steffen. Carbon monoxide in the solar atmosphere. II. Radiative cooling by CO lines. *Astronomy and Astrophysics*, 462:L31–L35, February 2007. doi: 10.1051/0004-6361:20066173.
- S. Wedemeyer-Böhm, I. Kamp, J. Bruls, and B. Freytag. Carbon monoxide in the solar atmosphere. I. Numerical method and two-dimensional models. *Astronomy and Astrophysics*, 438:1043–1057, August 2005. doi: 10.1051/0004-6361:20042550.
- S. Wedemeyer-Böhm, A. Lagg, and Å. Nordlund. Coupling from the Photosphere to the Chromosphere and the Corona. *Space Science Reviews*, 144:317–350, April 2009. doi: 10.1007/s11214-008-9447-8.
- S. Wedemeyer-Böhm, E. Scullion, O. Steiner, et al. Magnetic tornadoes as energy channels into the solar corona. *Nature*, 486:505–508, June 2012. doi: 10.1038/nature11202.
- S. Wende, A. Reiners, and H.-G. Ludwig. 3D simulations of M star atmosphere velocities and their influence on molecular FeH lines. *Astronomy and Astrophysics*, 508:1429–1442, December 2009. doi: 10.1051/0004-6361/200913149.
- O. C. Wilson. Chromospheric variations in main-sequence stars. *Astrophysical Journal*, 226:379–396, December 1978. doi: 10.1086/156618.
- O. C. Wilson and M. K. Vainu Bappu. H and K Emission in Late-Type Stars: Dependence of Line Width on Luminosity and Related Topics. *Astrophysical Journal*, 125:661, May 1957. doi: 10.1086/146339.
- K. T. Wong, T. Kamiński, K. M. Menten, and F. Wyrowski. Resolving the extended atmosphere and the inner wind of Mira (o Ceti) with long ALMA baselines. *Astronomy and Astrophysics*, 590:A127, May 2016. doi: 10.1051/0004-6361/201527867.

# Acknowledgement

First of all, I am very thankful to my supervisor Peter Hauschildt for giving me the opportunity to work in his group and on this project, for introducing me to the world of computational physics, and reviewing my dissertation.

A big “thank you” to Sven Wedemeyer for providing the CO<sup>5</sup>BOLD models used in this work, the long-distance discussions and feedback concerning my work, the supervision during my stay in Oslo, and for reviewing this thesis.

For their many suggestions and comments concerning this work and the great support during these three years, I am very grateful to Birgit Fuhrmeister, Andreas Schweitzer and Sören Witte.

My experience at the Hamburger Sternwarte has been amazing mostly thanks to the fantastic people I have met, too many to list them all here. Special mentions go to the secretary and administration, and to the PHOENIX folks, for all the group lunches, scientific discussions, random conversations, and awesome board game evenings.

The Pisa-connection is still strong: for the never-ending scientific stimulation and the uncountable advices on the path to become a scientist, I am greatly indebted to Steven Shore.

My childhood dreams and curiosity would have never led me into real science without the invaluable, endless support of my parents. Grazie.

I am immensely thankful to Marlies Meyer, for constantly being by my side, always ready to help, discuss, advise, comfort, and for reminding me that every day is special.

The simulations presented in this thesis were conducted thanks to generous amounts of allocated time at several super-computing facilities: NERSC, HLRN, HLRS, and Universität Hamburg RRZ. This work was financed by the DFG.



# Eidesstattliche Versicherung

Hiermit erkläre ich an Eides statt, dass ich die vorliegende Dissertationsschrift selbst verfasst und keine anderen als die angegebenen Quellen und Hilfsmittel benutzt habe.

I hereby declare, on oath, that I have written the present dissertation by my own and have not used other than the acknowledged resources and aids.

Hamburg, den 24.11.2016

Ivan De Gennaro Aquino